

**OBSERVATIONS OF WAVE-MEAN FLOW INTERACTION IN
THE PACIFIC EQUATORIAL UNDERCURRENT**

by

Esther Collison Brady

B. S., University of Massachusetts, Amherst
(1982)

SUBMITTED IN PARTIAL FULFILLMENT OF THE
REQUIREMENTS FOR THE DEGREE OF

DOCTOR OF PHILOSOPHY

at the

MASSACHUSETTS INSTITUTE OF TECHNOLOGY

and the

WOODS HOLE OCEANOGRAPHIC INSTITUTION

September 1990

© Esther C. Brady 1990

The author hereby grants to MIT and WHOI permission to reproduce
and distribute copies of this thesis document in whole or in part.

Signature of Author _____

Joint Program in Physical Oceanography,
Massachusetts Institute of Technology/
Woods Hole Oceanographic Institution

Certified by _____

0 0

Harry L. Bryden
Thesis Supervisor,
Woods Hole Oceanographic Institution

Accepted by _____

Carl Wunsch
Chairman, Joint Committee for Physical Oceanography,
Massachusetts Institute of Technology/
Woods Hole Oceanographic Institution

WITHDRAWN
FROM
MIT LIBRARIES

NOV 16 1990

LIBRARIES

Observations of Wave-Mean Flow Interaction in the Pacific Equatorial Undercurrent

ABSTRACT

The contribution of tropical instability waves to the momentum and energy balances of the Pacific Equatorial Undercurrent is investigated using velocity and temperature time series from the three-dimensional Equatorial Pacific Ocean Climate Study mooring array at 110°W. Tropical instability waves are an energetic band of variability typically with periods between 14 and 36 days which are thought to be generated by instability of the equatorial currents. They are frequently observed as meanders of the equatorial front in satellite sea surface temperature maps. Here, they are observed as large oscillations in the meridional velocity records at 110°W with an energy peak at 21 days. Westward phase propagation is observed in this band with a phase speed of $-0.9 (\pm 0.3) \text{ m s}^{-1}$ and a wavelength of 1660 km. Upward phase propagation is observed which is consistent with downward energy propagation. The observed propagation characteristics are compared with those of the mixed Rossby-gravity wave.

The variability in this band produces large northward fluxes of eastward momentum and southward fluxes of temperature which affect the dynamics of the mean Undercurrent through the Reynolds stress divergence, and the Eliassen-Palm flux divergence. The waves produce a northward flux of eastward momentum, uv , which is largest at the northern mooring in the upper part of the array. The meridional divergence of eastward momentum, $-\partial(uv)/\partial y$, decelerates the Undercurrent core down to 150 m. This implies a coupling between the Undercurrent and the South Equatorial Current with the eastward momentum of the Undercurrent transferred to the westward flowing South Equatorial Current. To estimate the vertical momentum flux divergence, the vertical eddy flux of eastward momentum, uw , is inferred using the eddy temperature equation. The vertical eddy momentum flux is positive and largest at the core of the Undercurrent, implying an acceleration of the eastward flow above the core and a deceleration below. The Eliassen-Palm flux divergence is small above the core of the Undercurrent at 75 m, but below the core, is sufficient to balance the deeply penetrating eastward pressure gradient force.

The instability waves are important to the energetics of the mean Undercurrent. An exchange of kinetic energy from the mean Undercurrent to the waves through shear production is estimated. A local exchange is suggested since the rate at which the mean Undercurrent loses kinetic energy through instability is comparable to the rate at which the waves gain energy through shear production. The conversion from mean to eddy potential energy is an order of magnitude smaller with the waves gaining potential energy through conversion of mean available potential energy. The observations of upward phase propagation and downward Eliassen-Palm flux suggest that the waves propagate energy downward into the deep ocean.

The energetics and momentum balance of the mean Undercurrent is investigated further by analyzing the downstream change in the Bernoulli function on the equator along isentropes or potential density surfaces using mean hydrographic sections at 150°W and 110°W. A downstream decrease in the Bernoulli function is observed which is due to a decrease in the Acceleration Potential since the mean kinetic energy of the Undercurrent changes little from 150°W to 110°W. The lateral divergence of eddy momentum fluxes calculated on isotherms is sufficient to balance the observed decrease in the Acceleration Potential. The downstream decrease in the Acceleration potential has further implications for the mean energetics since this "downhill" flow releases mean available potential energy stored in the east-west sloping thermocline. The rate at which the Undercurrent releases available potential energy, is shown to be comparable to the rate at which the mean flow loses kinetic energy by interaction with the waves, with the waves gaining kinetic energy in the process. Thus, it is hypothesized that in the eastern Pacific this downstream release of available potential energy is ultimately converted into a downstream increase in the kinetic energy of the waves rather than the kinetic energy of the mean flow as occurs in the western Pacific. To maintain an equilibrium, the waves radiate energy into the deep ocean as is suggested by the upward phase propagation and the downward Eliassen-Palm flux.

Thesis Supervisor: Dr. Harry L. Bryden

Title: Senior Scientist, Woods Hole Oceanographic Institution

Table of Contents

Abstract	3
Acknowledgements.....	8
Preface.....	11
CHAPTER 1 A Synopsis	
1.1 INTRODUCTION	13
1.2 SIMPLE LINEAR THEORY	15
1.3 THE YANAI-MARUYAMA WAVE IN THE ATMOSPHERE.....	23
1.4 THE INSTABILITY WAVES OF THE EQUATORIAL OCEANS.....	31
1.5 SUMMARY AND FINAL REMARKS.....	50
CHAPTER 2 Wave Analysis	
2.1 INTRODUCTION	57
2.2 DATA	58
2.3 HORIZONTAL PHASE PROPAGATION.....	63
2.4 VERTICAL PHASE PROPAGATION.....	67
2.5 DISCUSSION	73
CHAPTER 3 Zonal Momentum Balance	
3.1 INTRODUCTION	79
3.2 THE MEAN FLOW.....	79
3.3 MEAN ZONAL MOMENTUM BALANCE.....	93
3.4 THE ELIASSEN – PALM FLUX DIVERGENCE	115
3.5 PARAMETERIZING THE VERTICAL EDDY MOMENTUM FLUX.....	127

CHAPTER 4 Energetics

4.1 INTRODUCTION AND OBJECTIVE.....	131
4.2 METHOD	136
4.3 LOCAL KINETIC ENERGY CONVERSION.....	138
4.4 LOCAL POTENTIAL ENERGY CONVERSION.....	142
4.5 SUMMARY.....	145
4.6 CONCLUSION.....	146

CHAPTER 5 Isentropic Analysis

5.1 INTRODUCTION	147
5.2 ISENTROPIC ANALYSIS.....	157
5.3 DATA AND METHOD.....	163
5.4 RESULTS	168
5.5 DISCUSSION	181
5.6 CONCLUSIONS	186

CHAPTER 6 Final Remarks

6.1 SUMMARY.....	189
6.2 CONCLUSIONS	195

Appendix.....	199
---------------	-----

References.....	207
-----------------	-----

Biographical Sketch and List of Publications	215
--	-----

Acknowledgements

Dr. Harry Bryden has served many long years as my advisor and friend. I would especially like to thank him for developing my burgeoning interest in oceanography and steering me toward interesting equatorial problems. He has made many generous contributions to my scientific education; not the least of which was toward my financial and moral support. His enduring guidance, encouragement, motivating presence, and most of all patience, have enabled me to see this project to the end.

I thank the rest of my thesis Committee, Drs. Joseph Pedlosky, James Price, Paola Rizzoli, and John Toole, for their time, comments and encouragement. Each has contributed to my educational experience, through the courses they taught, advice they dispensed, discussions they stimulated, and perspectives they widened. In addition, I would like to thank Nick Fofonoff for doing a great job as Chairman of my thesis defense.

Thanks to Harry Bryden, I was introduced to the community of equatorial scientists; this interaction, particularly with the Tropic Heat scientists, has greatly enhanced my scientific experience. I wish to thank the Tropic Heaters for being so generous with their ideas and data, particularly David Halpern and Mike McPhaden for the EPOCS 110°W array data, Stan Hayes for the EPOCS 110°W CTD data, and Roger Lukas and Bruce Taft for the NORPAX CTD and 152°W current meter array data. Peter Niiler stirred up enthusiasm for equatorial puzzles. Mike Gregg and John Toole gave me the wonderful opportunity to go to sea on a Tropic Heat microstructure cruise. I gratefully acknowledge the financial support of the National Science Foundation under contracts OCE 82-14955 and OCE 85-19551, for participation in Tropic Heat, and OCE 85-04125.

The technical assistance I received from the following individuals was first-rate: Ann Spencer, Mary Woodgate-Jones, Lorraine Barbour, Delores Chausse, and Susan Tarbell. Ann cheerfully solved many of my time-series processing crises. She was a constant source of “buoyant” wisdom during the last few years of my studies. Mary Woodgate-Jones was invaluable with the processing of the CTD data. She spent many hours with me when I began this work, teaching me the WHOI CTD data processing algorithms. Lorraine

Barbour meticulously assisted with the preparation of figures. Susan Tarbell and Delores Chausse did the initial processing of the current meter data. This thesis could not have been completed without the expertise of these individuals. I have enjoyed working with them and thank them for their time, help, and good humor.

The following individuals made my life a lot easier at WHOI because of the wonderful jobs they performed, and a lot more enjoyable because of the wonderful people they are: Veta Green, Maureen Carragher, Ann-Marie Michael, Karin Bohr, Barbara Gaffron, Audrey Williams, Lisa Wolfe, Jeanne Young, MaryAnn Lucas, and Claire Reid. In addition, I would like to thank Donna Scheer and Vicky Cullen at Graphic Arts for being extremely helpful in allowing me use of their laser printer.

The WHOI Education Office is responsible for making my educational experience at WHOI exceptionally rewarding. I would have slipped into the abyss without the special attention of Jake Peirson and Abbie Jackson. Abbie and Jake were my expert guides through the innumerable rules and regulations of MIT. Jake Peirson's dedication to science education at all levels is commendable.

When I began my scientific career at the University of Massachusetts at Amherst, I was fortunate to have Drs. Judy Young and Laurie Brown as inspirational role models. I admire their commitment to both family and science, and hope to continue their dedication to advancing the tradition of women in science.

My WHOI friends and office-mates were an infinite source of encouragement and, more importantly, zaniness. George Bell has belayed me over the final crux of this seemingly sheer vertical wall; with his enthusiasm, energy, and encouragement, I've spent this last year happily striving for the achievement of higher places.

Lastly, I thank my parents, Dave and Carol Brady, and my siblings Julie, John and Jane for their love and support. They were my first teachers, and my first friends. I've learned more from them and because of them, than will ever fit in any book.

PREFACE

The purpose of this thesis is to investigate the role of the tropical instability waves in the dynamics of the Pacific Equatorial Undercurrent. A number of approaches have been made in order to understand this wave-mean flow interaction problem. They are developed in the following way:

Chapter 1 is a review of relevant wave observations in the atmosphere and all three equatorial oceans. There is a wave in the atmosphere, the Yanai-Maruyama wave, which is explored as a useful analogy to the waves observed in the ocean, which have been described as *tropical instability waves*. Because the atmosphere is more accessible to observational studies, and because the Yanai-Maruyama waves have been observed for far longer than the tropical instability waves, it is useful to compare the oceanic and atmospheric observations in the context of wave-mean flow interaction. Observations of tropical instability waves in all three oceans are reviewed. Special attention is focused on the instability waves as observed in numerical ocean models and how the dynamical interpretation is enhanced by these studies.

Chapter 2 presents an analysis of the propagation characteristics of the wave disturbance associated with the variability in the tropical instability wave band as observed in one portion of the EPOCS velocity and temperature array at 110°W. Spectral analysis reveals westward and downward propagation. A comparison with the linear mixed Rossby-gravity wave is suggested from the dispersion properties.

Chapter 3 explores the EPOCS current meter array observations further by investigating the effect of the tropical instability wave band on the zonal momentum balance of the Undercurrent. Spectral analysis reveals large and coherent eddy fluxes of temperature and momentum. These are used to estimate the effect of the Reynolds stress divergence. Eliassen-Palm (EP) flux divergence is estimated as well and found to be a useful diagnostic for understanding the direct and indirect effects of the waves on the mean Undercurrent.

Chapter 4 discusses another aspect of wave-mean flow interaction— the energy conversion from the mean flow to the eddies. The EPOCS array provides estimates of the exchange terms in the energy conversion process. Connection is made to the previous two chapters which independently estimate the propagation of energy: in Chapter 2, through the observed phase propagation, and in Chapter 3 by way of the EP flux which indicates the direction of energy propagation.

Chapter 5 investigates the zonal momentum balance of the Undercurrent with a traditional approach derived from core layer or isentropic analysis. Time averaged CTD data and spectral analysis of the EPOCS data interpolated to temperature surfaces are used to define a downstream coordinate system. The isentropic reference frame used in this analysis is useful because the diapycnal transports determined, are directly related to mechanisms of forcing and dissipation.

Chapter 6 summarizes the results of Chapters 2, 3, 4, and 5 and presents the conclusions of the thesis.

CHAPTER 1:

The Mixed Rossby-gravity Wave in the Atmosphere and Oceans: A Synopsis

1.1 INTRODUCTION

One of the most prominent and persistent modes of variability observed in all equatorial regions of our planet is the mixed Rossby-gravity wave of linear equatorial wave theory. All tropical oceans, the troposphere and stratosphere, and most eddy-resolving tropical numerical models, reveal narrow, energetic peaks in the mesoscale meridional velocity spectra which are identified as mixed Rossby gravity waves.

Equatorial wave motions have been observed in a number of ways, as large spectral peaks above the background spectrum (Wunsch and Gill, 1976), as distinct travelling pulses or packets of velocity or temperature as in the case of Kelvin waves (Lukas and Firing, 1982), or, when no such anomaly is present, by the evidence that the observed shape of the continuous energy spectrum can be explained by the theoretical spectrum of free linear waves (Eriksen, 1978). Usually these observations are classified by drawing qualitative comparisons to simple linear equatorial wave theory based on the observed zonal and vertical phase speeds, variance distributions and polarization relationships. However, the study of waves is interesting not because they can be observed and classified isolated from the surrounding large scale background flow, but because these waves may play a unique role in the large scale circulation. Their existence may be a clue to some larger phenomena, like the quasi-biennial oscillation in the atmosphere or shear flow instability in the ocean. Determining the important function these waves serve in their respective media should be the focus of study. The purpose of this review is to explore the literature on mixed Rossby-gravity

waves with the universality of the existence of these waves as the crux. The comparisons may illuminate the important physics. If due to an instability, why is this wave observed above all others excited? Are they the fastest growing mode? A resonance? A standing mode? Are they remotely forced from some other region? Does their presence suggest an interesting feedback mechanism, locally with the mean flow or with other waves (such as occurs during the QBO), or remotely with other regions? The following subjects will be explored in this review as they relate to the mixed Rossby-gravity wave: remote forcing, in-situ instability, and effect on the mean flow. First, the linear theory of mixed Rossby-gravity waves is reviewed.

1.2 SIMPLE LINEAR THEORY

Preceding the first observations of mixed Rossby-gravity waves in the stratosphere, there were some early key developments in the theory of trapped motions on the equator, most notably by Ichiye (1960), Stern (1963) and Bretherton (1964) as discussed by Matsuno (1966). However, the works of Matsuno (1966) and Blandford (1966), focused on the special problem of the mixed Rossby-gravity wave solution. The treatment of free equatorial waves presented here follows the presentation of Philander (1978) and Eriksen (1978).

The mixed Rossby-gravity wave mode is a solution to the following linearized, hydrostatic, Boussinesq, equatorial beta-plane equations with no mean flow in standard oceanographic notation:

$$\frac{\partial u}{\partial t} - \beta y v = -\frac{1}{\rho_0} \frac{\partial p}{\partial x}$$

$$\frac{\partial v}{\partial t} + \beta y u = -\frac{1}{\rho_0} \frac{\partial p}{\partial y}$$

$$\rho' g = -\frac{\partial p}{\partial z}$$

$$\frac{\partial u}{\partial x} + \frac{\partial v}{\partial y} + \frac{\partial w}{\partial z} = 0$$

$$\frac{\partial \rho}{\partial t} + w \frac{d\rho^*}{dz} = 0$$

where, $\rho(x, y, z, t) = \rho_0 + \rho'(x, y, z, t) + \rho^*(z)$.

Solving for waves which have separable structures in the meridional, y , and vertical, z , dimensions, and a purely propagating structure in the zonal, x dimension, with a wavenumber k and frequency ω , the horizontal velocity, (u,v) , and pressure p , can be written in the form,

$$\begin{Bmatrix} u \\ v \\ p \end{Bmatrix} = \begin{Bmatrix} U(y) \\ V(y) \\ \rho_0 P(y) \end{Bmatrix} \frac{dG(z)}{dz} e^{i(kx - \omega t)}.$$

Substituting this form into the equations above, and separating with the separation parameter c^2 , yields an equation for the vertical structure of $G(z)$,

$$\frac{d^2 G(z)}{dz^2} + \frac{N^2(z)}{c^2} G(z) = 0,$$

with $N^2(z) = -\frac{g}{\rho_0} \frac{d\rho^*}{dz}$. The separation parameter, $c^2 = g h_e$, where h_e is the equivalent depth, is used to non-dimensionalize all parameters with characteristic scales for length, $(c/\beta)^{1/2}$, and time, $(\beta c)^{-1/2}$.

After further manipulation, the meridional structure equation for $V(y)$ is obtained,

$$\frac{\partial^2 V}{\partial y^2} + (\omega^2/c^2 - k^2 - \beta k/\omega - \beta^2 y^2/c^2) V = 0.$$

In general, with a condition that the solutions remain bounded over the whole domain,

$$V \rightarrow 0 \text{ as } y \rightarrow \pm \infty,$$

free solutions to the meridional structure equation are expressed as an infinite set of Hermite functions:

$$V(y) = V_n \exp\{-\frac{1}{2}\beta y^2/c\} H_n((\beta/c)^{1/2} y),$$

where $H_n(y)$ are the complete set of Hermite polynomials. These solutions with the meridional mode number n , are associated with a dispersion relation for the frequency and wavenumber given by,

$$(2n + 1)\beta/c = \omega^2/c^2 - k^2 - \beta k/\omega,$$

where, n is a positive integer equal to 0, 1, 2, If the vertical structure equation is solved for vertical modes with a given $N(z)$ profile, then the parameter c is the eigenvalue of the vertical structure equation. An infinite set of baroclinic moded results each associated with a different equivalent depth h_e . Then, ω and k are found from the above dispersion relation for a given c . Alternately, the meridional structure equation can be solved for a given ω or k , with c is determined by the above dispersion relation.

When $n = 0$, and ω and k are non-dimensionalized by c , where $\sigma = \omega(\beta c)^{1/2}$ and $s = k(c/\beta)^{1/2}$, the dispersion relation factors into,

$$(\sigma + s)(\sigma^2 - s\sigma - 1) = 0,$$

for two roots. The first root, $\sigma = -s$, the anti-Kelvin root, is not valid on an infinite beta plane because the corresponding solutions to u and p are unbounded as η grows toward $\pm \infty$, (Matsuno, 1966). The second root, which is valid, is the mixed Rossby-gravity wave dispersion relation,

$$s = \sigma - 1/\sigma.$$

For $n > 0$ the waves are grouped into two classes, for $\sigma \gg 1$, the waves are inertio-gravity waves and for $\sigma \ll 1$ the waves are Rossby waves. For large s and westward phase speeds, the mixed Rossby-gravity wave behaves like a Rossby wave; and for large s but eastward phase speed, the behavior is like an inertio-gravity wave. The resulting dispersion curves are shown in figure 1.1.

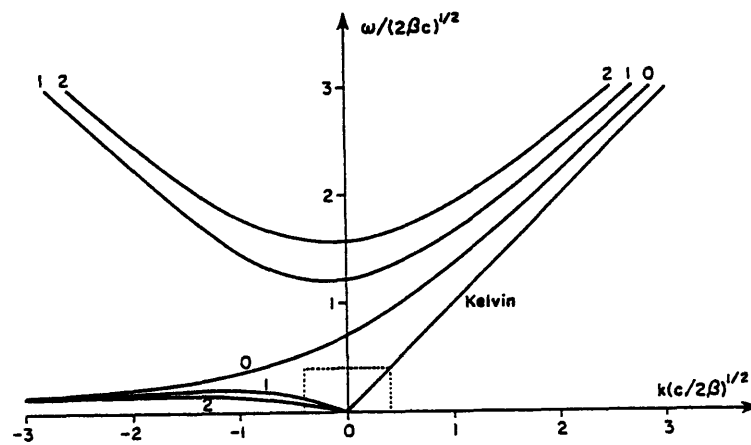


Figure 1.1: Dispersion curves for free waves on the equatorial beta plane. The vertical axis is the nondimensional frequency and the horizontal axis is the nondimensional zonal wavenumber. The curve labeled with 0 is the mixed Rossby-gravity wave. The upper curves labeled 1 and 2 are the inertio-gravity waves and the lower curves labeled 1 and 2 are the Rossby waves. (figure 11.1 from Gill, 1982)

The dispersion relationships for these two branches when $n > 0$, have a point where the zonal group velocity, $\frac{\partial \sigma}{\partial s}$, is zero at $s\sigma = -\frac{1}{2}$. However, the mixed Rossby-gravity wave has eastward group velocity for all k .

The equatorial beta-plane wave-guide solutions are more rigorously an approximation to the solutions of the Laplace Tidal Equations (LTE) on a sphere, for a particular range of eigenvalues where the Lamb parameter, $(2\Omega R)^2/gh_e$, tends toward infinity. This happens for small equivalent depths h_e , and when the squared angular rotation speed of the Earth at radius R and rotation rate Ω , is much larger than the baroclinic mode Kelvin wave speed $(\sqrt{gh_e})$, squared. This condition is met for all baroclinic modes in the ocean, because of the small equivalent depths, but in the atmosphere, for only those modes with small vertical wavelength. Furthermore, because the equatorial beta plane makes the unrealistic assumption that f tends to infinity, only the solutions with rapid decay scales are valid approximations to the LTE solutions. This includes the mixed Rossby-gravity mode, the Kelvin mode, and only the first few of the other meridional modes of Rossby and Inertio-gravity waves. Because the latitude beyond which the wave decays exponentially, the turning latitude, is proportional to the square root of $(2n+1)$, the mixed Rossby-gravity wave, with $n = 0$, is the mode most strongly confined to the equator.

For a finite ocean, with lateral boundaries placed somewhere in the tropics or mid-latitudes, the mixed Rossby-gravity solution breaks into two modes asymptotic to the two roots in the infinite case solution (Cane and Sarachik, 1979). The low frequency mode belongs with the Rossby wave group and the high frequency mode belongs to the inertio-gravity group. These two modes possess zero group velocity locations where $s\sigma = -1/2$, like all the other equatorial modes except the Kelvin wave.

In the finite bounded equatorial beta- plane, with boundaries at $\pm L$, such that the new boundary conditions are,

$$V(\eta) = 0 \text{ at } \eta = \pm L,$$

the dispersion relation,

$$2\mu + 1 = \sigma^2 - s^2 - s / \sigma,$$

is nearly unchanged except that μ can take on a full range of values depending on L , not just an integer. For L much greater than the turning latitude of the mode, the eigenvalues μ are exponentially close to integers,

$$\mu \approx n + 2\pi^{1/2}L \exp(-L^2)$$

In this case, the finite V solutions closely resemble the infinite solutions except within a Rossby radius of the boundaries where the solutions are brought to zero. Cane and Sarachik (1979) demonstrate that for $n = 0$, where the bounded mixed Rossby-gravity curve is near the anti-Kelvin mode curve, for small σ and s where $\sigma \approx -s$ to order μ , the u and p fields are exponentially large at the boundaries, decaying equatorward over a deformation scale, and thus behave like a Kelvin wave. This particular mode propagates energy around the basin in the adjustment of the basin circulation to the applied forcing.

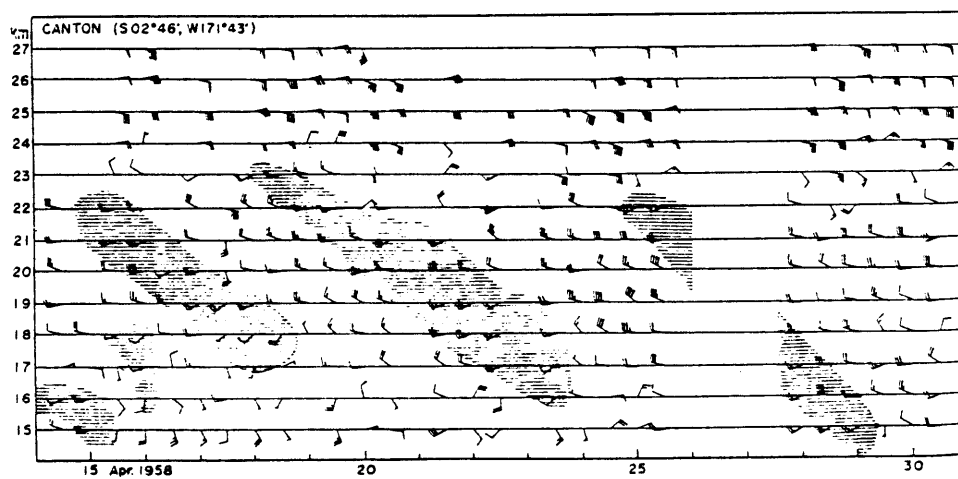


Figure 1.2a: Vertical time section of the lower stratospheric winds at Canton Island for 15-30 April 1958. Winds with southerly components are shaded. (Figure 3 from Yanai and Maruyama, 1966)

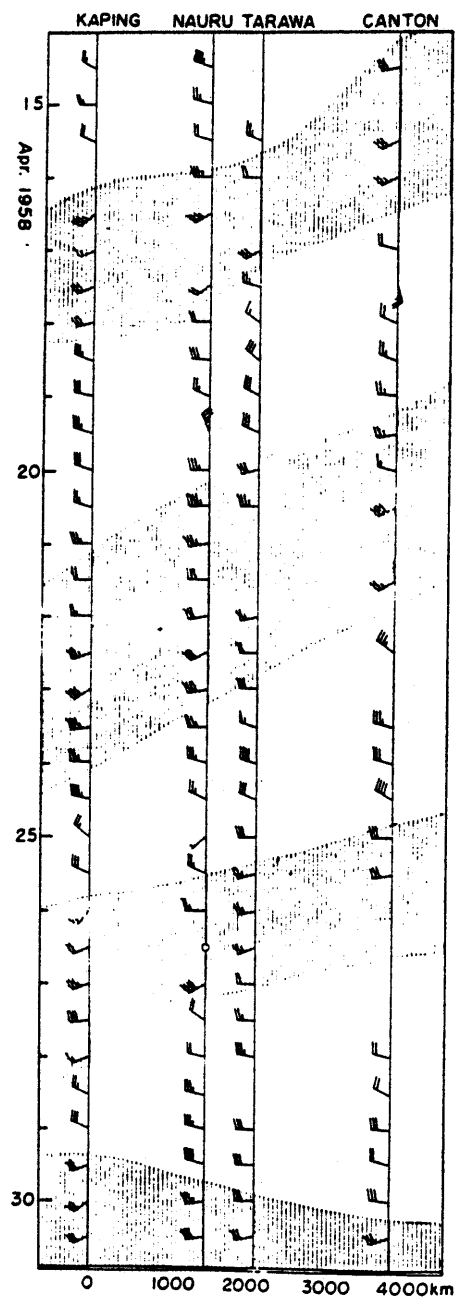


Figure 1.2b: Time series of 70,000 ft (or 21 km) winds at Kapingamarangi, Nauru, Tarawa and Canton Island for 15-30 April 1958. Winds with southerly components are shaded. (Figure 4 from Yanai and Maruyama, 1966)

1.3 THE YANAI-MARUYAMA WAVE IN THE ATMOSPHERE

The earliest accounts of observations identified as mixed Rossby-gravity waves were reported in the atmospheric literature in the late 1960's at about the same time as the equatorial wave theory was being developed. Initially these waves were noticed in central Pacific island upper air station wind records of the lower stratosphere from the spring of 1958, as a 4-5 day oscillation of the meridional wind with a wavelength equal to one fourth the Earth's circumference, (i.e. $\lambda = 10,000$ km, $s = 4$), (Yanai and Maruyama, 1966). The characteristic signature of westward and upward phase propagation is noted in figure 1.2. Additional evidence for identification with the mixed Rossby-gravity wave was provided later as more sophisticated spectral analysis techniques were used to show that the 4 - 5 day meridional velocity variance was more pronounced equatorward of about 5 degrees of latitude, while the zonal velocity variance peaked off equator, (Maruyama, 1968), figure 1.3. Also reported at this time, was a prominent peak in the zonal wind variance, identified as a Kelvin wave with a 15 day period and wavelength equal to one circumference of the Earth, (i.e. $\lambda = 40,000$ km, $s = 1$; Wallace and Kousky, 1968). The generation of these waves in the tropical atmosphere remains a subject of controversy to this day, although strong evidence suggests a complicated mechanism involving mid-latitude radiation in the stratosphere coupled with latent heat release in the troposphere. The interaction of these two most energetic wave modes with the mean zonal flow, eventually was hypothesized as the mechanism of the Quasi-Biennial Oscillation (QBO) by Lindzen and Holton, (1970). However, because the presence of the Yanai-Maruyama waves are usually associated with a gradually weakening westerly flow, the link to the QBO was hypothesized immediately even though the theory was formally developed later.

These waves initially noticed in the lower stratosphere, were found to be associated with an upward flux of westerly momentum at the level of the Tropopause, (Maruyama, 1968). Maruyama obtained an estimate of the cospectrum of zonal velocity and upward velocity, which can not be directly measured, from the quadrature spectrum of zonal velocity and temperature. Yanai and Hayashi, (1969) estimated an upward energy flux (actually pressure

CHRISTMAS 100 MB APRIL-JULY 1962

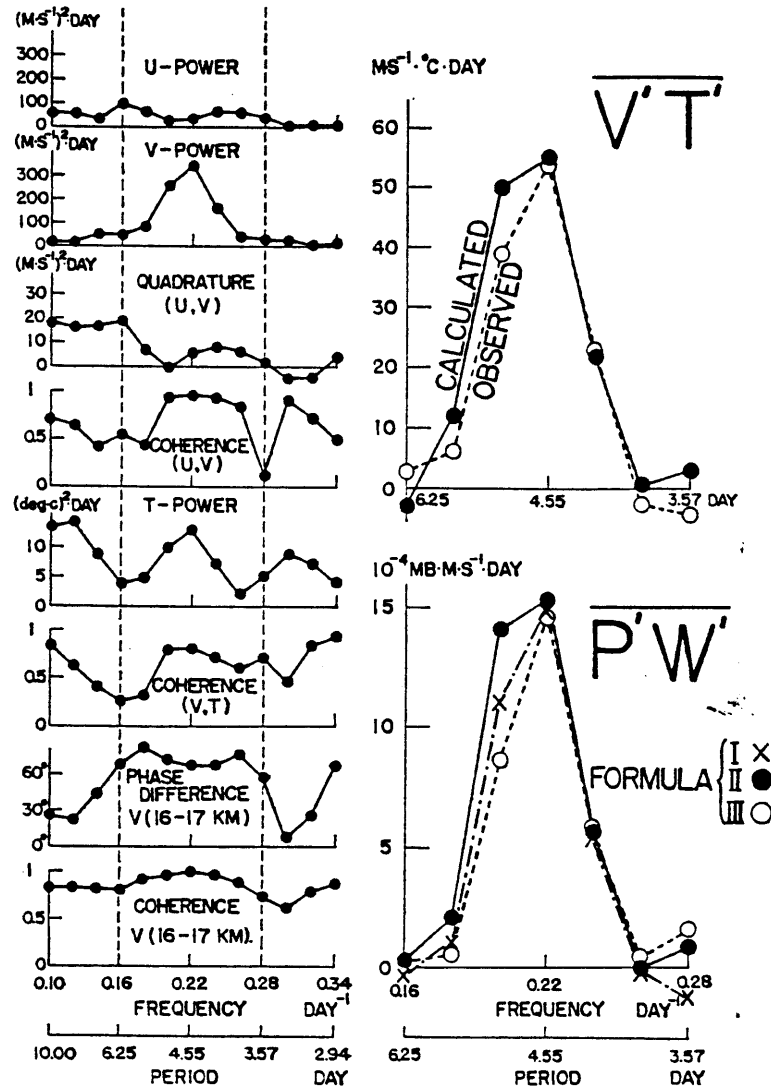


Figure 1.4: The left panel presents curves of various spectral estimates. The two vertical dashed lines indicated the frequency range in which $\overline{v'T'}$ and $\overline{p'w'}$ are calculated. Upper right are the spectral curves of $\overline{v'T'}$. The full line denotes $\overline{v'T'}$ calculated from the thermal wind relation. The dashed line denotes $\overline{v'T'}$ obtained by the use of observed temperature. Lower right are the spectral curves of $\overline{p'w'}$ obtained from the $\overline{v'T'}$ curves using theory. (Figure 11 from Maruyama, 1968)

work, $p'w'$) at the level of the Tropopause by relating this flux to a poleward sensible heat flux, $v'T'$. Energy propagating upwards from the troposphere into the stratosphere, is consistent with the downward propagation of phase as initially noticed by Yanai and Maruyama (1966), reproduced in figure 1.4. The energy for the lower stratospheric waves is thought to be generated in the upper troposphere, from coupling to mid-latitude eddies of the subtropical jet, and in the lower troposphere, from either lateral shear instability of the mean flow or deep moist convection. From a scale analysis of tropical motions, Charney (1963) demonstrated that motions in the upper and lower troposphere are essentially uncoupled because the vertical wavenumber is proportional to N^2/f^2 . Thus, the smallness of the Coriolis parameter f in the tropics, makes possible only small vertical wavelength waves, except during deep moist convection events when N^2 is also small.

Furthermore, an equatorward flux of pressure work, associated with poleward flux of eastward momentum, is estimated, using the Eliassen-Palm approximation, at the tropopause level (Zangvil and Yanai, 1980; Yanai and Lu, 1983). In Yanai and Lu's study it was noted that the waves were not present in 1972 when no convergence of meridional pressure work at mid-latitudes at this frequency and wave number was evident. However, they were present in 1967 when a strong convergence was noted from 30N to 20S, figure 1.5. This equatorward flux of wave energy suggests a possible mechanism for exciting the waves in the lower troposphere. The poleward flux of eastward momentum ($u'v' > 0$) implies that eddy kinetic energy is converted to kinetic energy of the mean flow, since in the Northern (Southern) Hemisphere, the meridional shear of the mean zonal flow is positive (negative).

From the earliest observations, the subject of remote forcing by mid latitude radiation was suggested as a possible excitation mechanism, but why the particular wave mode observed was selected was unknown. Excitation by mid-latitude radiation was suggested by many observationalists (Yanai and Lu, 1983) who demonstrated that fluxes of wave energy at the level of the tropopause in midlatitudes were directed equatorward. The interpretation was that the waves are forced by midlatitude disturbances in the lower levels and then propagate upwards through the tropopause to participate in the

QBO. Mak (1969) with a numerical study, followed by Lamb (1973) with an analytical study investigated this hypothesis with some corroborating success.

To investigate the hypothesis of excitation by mid-latitude radiation, Mak (1969) forced a dry two-layer numerical model stochastically at the poleward boundaries. Each layer had a zonal flow with poleward meridional shear. The lower level realistically represented the weak easterlies at the equator and weak westerlies at mid latitude and the upper layer had the strong westerlies of the subtropical jet and weak easterlies at the equator. Friction was included and parameterized as a vertical stress proportional to the vertical shear between layers and a linear surface drag on the lower layer. The model was successful at exciting the $s = 4$, $p = 5$ days, peak in the meridional velocity spectrum (figure 1.6). These waves had energy peaks located at the zero group velocity points on the dispersion curves of the finite bounded theory. The forced waves with other frequencies did not show up as peaks on the spectrum because the energy propagated away. However not all zero group velocity waves were excited, just the mixed Rossby-gravity wave, and to a lesser extent, the first baroclinic mode Rossby wave.

Lamb (1973) investigated the possibility that the waves are remotely forced specifically addressing the question of why the particular mode observed is selected above all others. A channel model was forced at the north and south walls with a wide spectrum in vertical and zonal wavenumber and period. Peak responses in the upward energy flux were found close to the free waves of the channel model. The forced modes with the maximum vertical energy flux, had a small complex component to the vertical wavenumber, with the real component of the wavenumber identical to the free mode. These peak wave modes were found to be the most efficient at allowing energy to propagate upwards.

The mechanism of remote mid-latitude excitation highlights the two different interpretations of waves, that is meridional modes vs rays. Rays are packets of energy propagating outward from the region of forcing. Rays contain waves with a continuum of wavenumber and frequency distributed about a central wavenumber and frequency, with the frequency $\omega(k, l, m)$, a function of the wavenumbers. When the phase speed is the same for all waves in the packet, the packet is nondispersive. This is true for packets of Kelvin waves whose dispersion relation is give by $\omega = kc$, such that the group

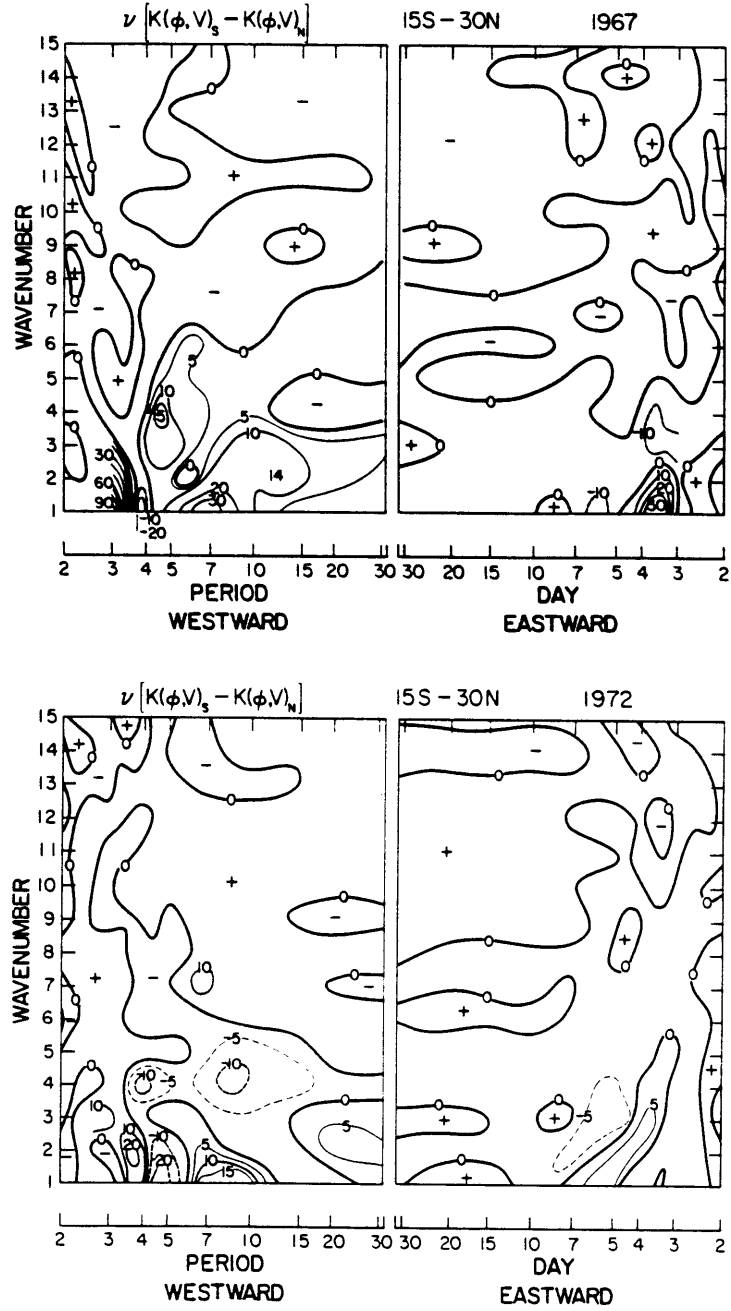


Figure 1.5: Wavenumber-frequency diagram of the meridional convergence of wave energy flux in the latitude belt 15°S to 30°N for (a) 1967 and (b) 1972. (Figures 18 and 19 from Yanai and Lu, 1983).

velocity is equal to the phase velocity. All Kelvin waves with a given baroclinic structure, determined by the eigenvalue of the vertical structure equation, $c = (g'h)^{1/2}$, have the same phase speed c . In ray theory midlatitude Rossby waves are prohibited from propagating equatorward beyond their critical latitude, where the zonal phase speed c , is equal to the mean zonal flow speed U . For waves propagating equatorward from mid-latitude, there is a more stringent requirement on the phase speed of the wave, such that additionally the phase speed of the wave must be larger than the local Rossby phase speed, $U - \beta/(k^2 + L_d^{-2})$ where L_d is the local Rossby deformation radius (Charney and Drazin, 1961). Otherwise the meridional and vertical wavenumbers are imaginary and the waves are trapped to the forcing region. However, in the case of the observed mixed Rossby-gravity wave, the phase speed is westward and large compared to the generally weak easterlies observed in the tropics. There is then no critical latitude since the wave propagates westward at the equator relative to the mean flow at a speed on the order of 16 m s^{-1} (Yanai and Lu, 1983).

On the other hand, the interpretation as meridional modes allows for a consideration of boundary forcing. Then modes are resonantly excited when the free wave dispersion relationship matches the forced frequencies and wavenumbers. Energy will build up in the spectrum where there is a zonal group velocity zero. Thus, the mixed Rossby-gravity wave, which possesses a zero eastward group velocity when the equatorial beta plane equations are solved on a plane with zonal boundaries at some latitude, is potentially a candidate for resonant excitation by midlatitude forcing.

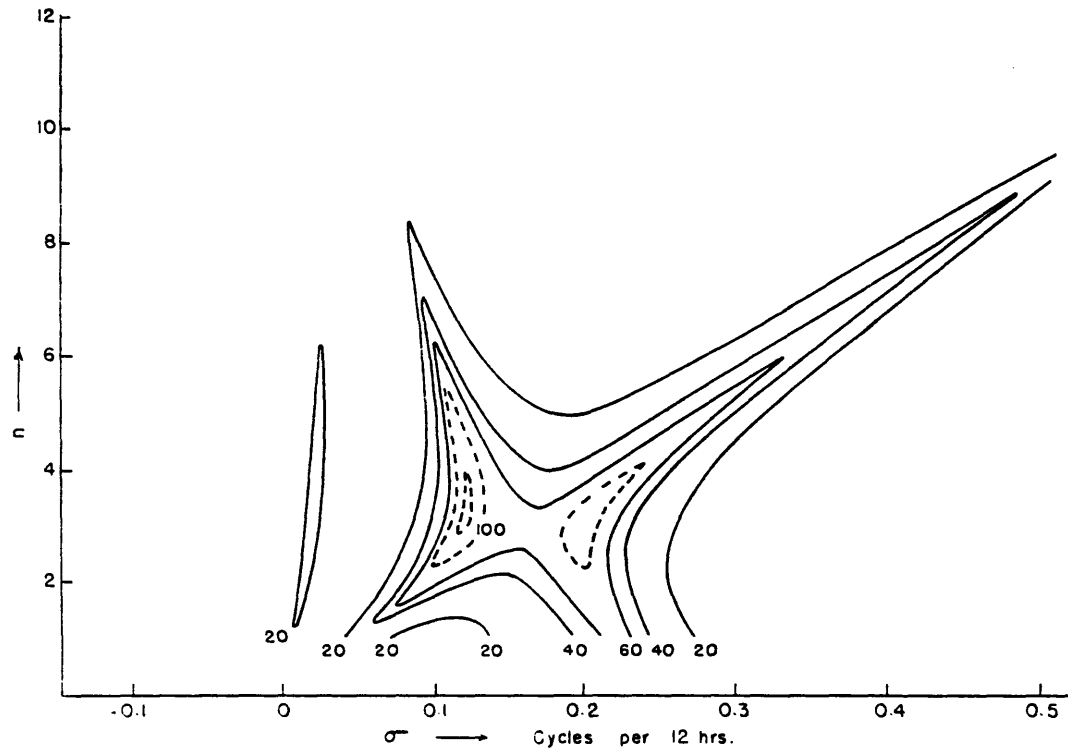


Figure 1.6: Variance in the even (symmetric meridional mode) baroclinic meridional velocity solutions of Mak's numerical model, as a function of frequency and zonal wavenumber n , where $n = 2\pi R/\lambda$, R is the Earth's equatorial radius and λ is the zonal wavelength of the wave. In the meteorological definition, negative frequency would imply eastward propagation of phase. (Figure 7 from Mak, 1969).

1.4 THE INSTABILITY WAVES OF THE EQUATORIAL OCEANS

The oceanic analogues to the Yanai-Maruyama waves of the tropical atmosphere, are prominently observed in all equatorial oceans, and in eddy-resolving numerical ocean models. The existence of the ocean waves was first reported nearly 10 years after identification of the Yanai-Maruyama waves. Meanders of the strong equatorial Atlantic currents were observed by Duing et al (1975), shown in figure 1.7. Both the South Equatorial Current (SEC; figure 1.7a) and the Equatorial Undercurrent (EUC; figure 1.7b, c) were observed to meander about the equator at a period of 16 days and a wavelength of 2600 km. This meandering is most dramatically demonstrated by the meridional excursions of the salinity maximum associated with the core of the EUC (figure 1.7d,e). Because the equatorial currents are so strongly confined to the equator with meridional scales close to wave scales, the anti-symmetric mixed Rossby gravity waves are manifest as meanders of the equatorial currents and the corresponding equatorial fronts. The currents may be unstable during part of the year during which the shear is strongest, and numerical models (Cox, 1980) suggest these instabilities give rise to a downward radiating mixed Rossby-gravity waves mode. These tropical instability waves, may or may not be a separately observable feature from the mixed Rossby-gravity waves. However, there is some confusion because the present observations cannot be used to distinguish between the instability waves and the mixed Rossby-gravity waves, particularly in the Pacific where significant energy is observed in the zonal velocity component. In addition, a first baroclinic mode Rossby wave may be present in the observations as suggested by the numerical models (Cox, 1980; Semtner and Holland, 1980).

In the eastern Pacific, satellite infrared images revealed westward travelling meridional excursions of the Pacific equatorial sea surface temperature front (Legeckis, 1977). The cusp to cusp zonal wavelengths were measured at about 800-1200 km, and travelled west with a speed of about 40 cm s^{-1} over ground, yielding a period of 20 to 30 days, shown in figure 1.8. It was thought that these SST meanders at the surface, excited trapped equatorial waves which radiated downward and eastward into the deep ocean as long waves. This became the hypothesis for the existence of the velocity fluctuations in records of bottom mounted current meters and electric field

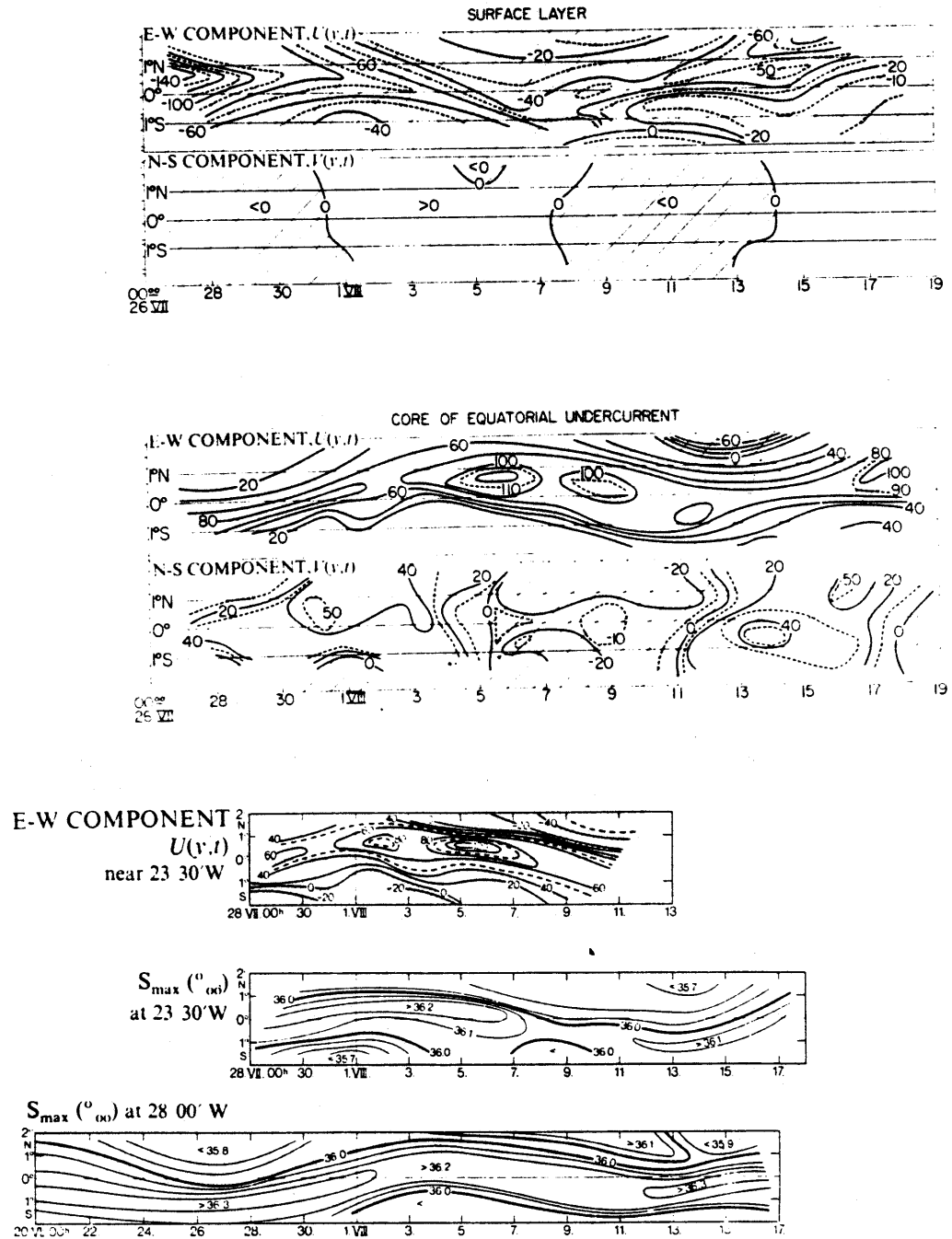


Figure 1.7: Time series at (a) surface and (b) core of equatorial Undercurrent of maximum zonal velocity and corresponding meridional velocity, at 28°W. Timeseries at the Undercurrent core of (c) maximum zonal velocity and (d) salinity at 23.5°W and (e) salinity at 28°W. Hatched areas represent westward or southward flow. (Figures 3, 4 and 5 from Duing et al., 1975)

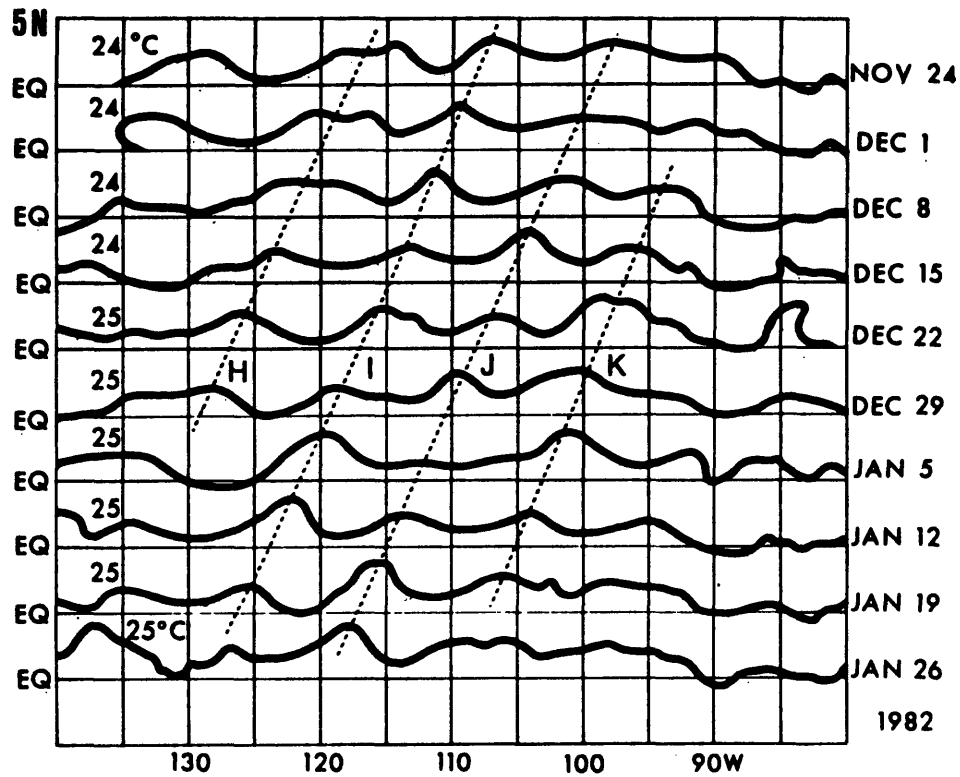


Figure 1.8: Progression in time of either the 24 or 25°C isotherm contour representing the temperature front north of the equator in the eastern Pacific taken from 7-day MCSST analyses during late November 1981 through January 1982. Dotted lines labeled H through K show westward propagation of phase of peaks. (Figure 7 from Legeckis et al., 1983).

recorders, observed during the 1975 ENSO by Harvey and Patzert (1976). They found upward and westward phase propagation with a 25 day period and a 1000 km wavelength.

In the Atlantic Ocean in the Gulf of Guinea, Weisberg, Horigan and Colin (1979) made the first comparison of the spectral properties of current meter velocity oscillations to the mixed Rossby-gravity wave. The oscillations were observed to have a 31 day period and a 1220 km wavelength. They show that the fluctuations observed at various longitudes along the equator display the following characteristics of the mixed Rossby-gravity wave: equatorial trapping, symmetry about the equator in the meridional velocity, nodes in zonal velocity and temperature on the equator, rectilinear polarized coherent motions on the equator and elliptical polarization off the equator, and westward and upward phase propagation. In addition some evidence for eastward propagation of the wave packet is shown (figure 1.9, from Weisberg, 1984).

Based on tide gauge records at Fanning Island, 4°N, 159°W in the Pacific, Wyrtki (1978) related a 34 day oscillation in sea level, with an amplitude of 7 cm to meridional excursions in the meanders of drifting buoy trajectories at 6°N which is in the North Equatorial Countercurrent (NECC). These meanders are observed in the boreal fall when the NECC is at its strongest. The sea level oscillations can be accounted for by the meridional displacements of the sloping dynamic topography associated with the NECC which is downward north of the ridge of dynamic topography on which Fanning Island is situated. More recently Geosat and Seasat altimeter observations lend support to the existence of these off-equatorial oscillations in sea level which accompany the instability waves, (Perigaud, 1989, 1990; Malarde et al., 1987). The Geosat analyses, (Perigaud, 1989, 1990), indicate zonal belts of sea level anomalies at 5°N and 12°N. The periods of high wave activity in the belt at 5°N in the eastern Pacific corresponds to periods of increased shear strength between the SEC and the NECC. However, the periods of high wave activity at 12°N are not as well correlated with periods of strong shear between the NECC and the North Equatorial Current (NEC), although some connection is suggested. The most energetic wavelength and period obtained by the Geosat analysis at 5°N, are 1200 km and 33 d, which compare well with the estimates found for Legeckis' SST meander analysis,

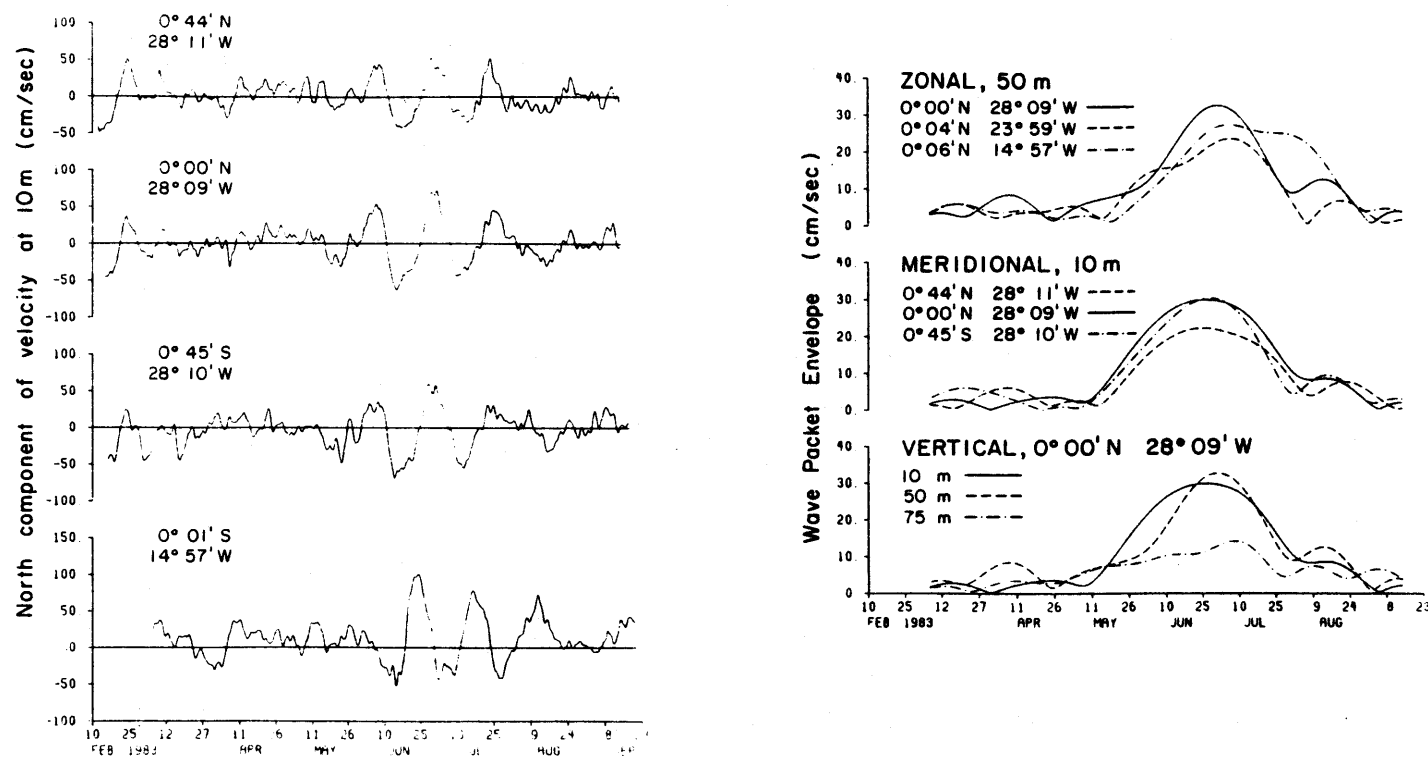


Figure 1.9: (a) Meridional velocity component at 10m during SEQUAL, low-pass filtered; (b) Envelopes of complex demodulated wave packets about a central frequency of 4×10^{-2} cpd with a bandwidth of 4.4×10^{-2} cpd, as a function of time at various locations indicating zonal and vertical propagation of energy. (Figures 1 and 4 from Weisberg, 1984).

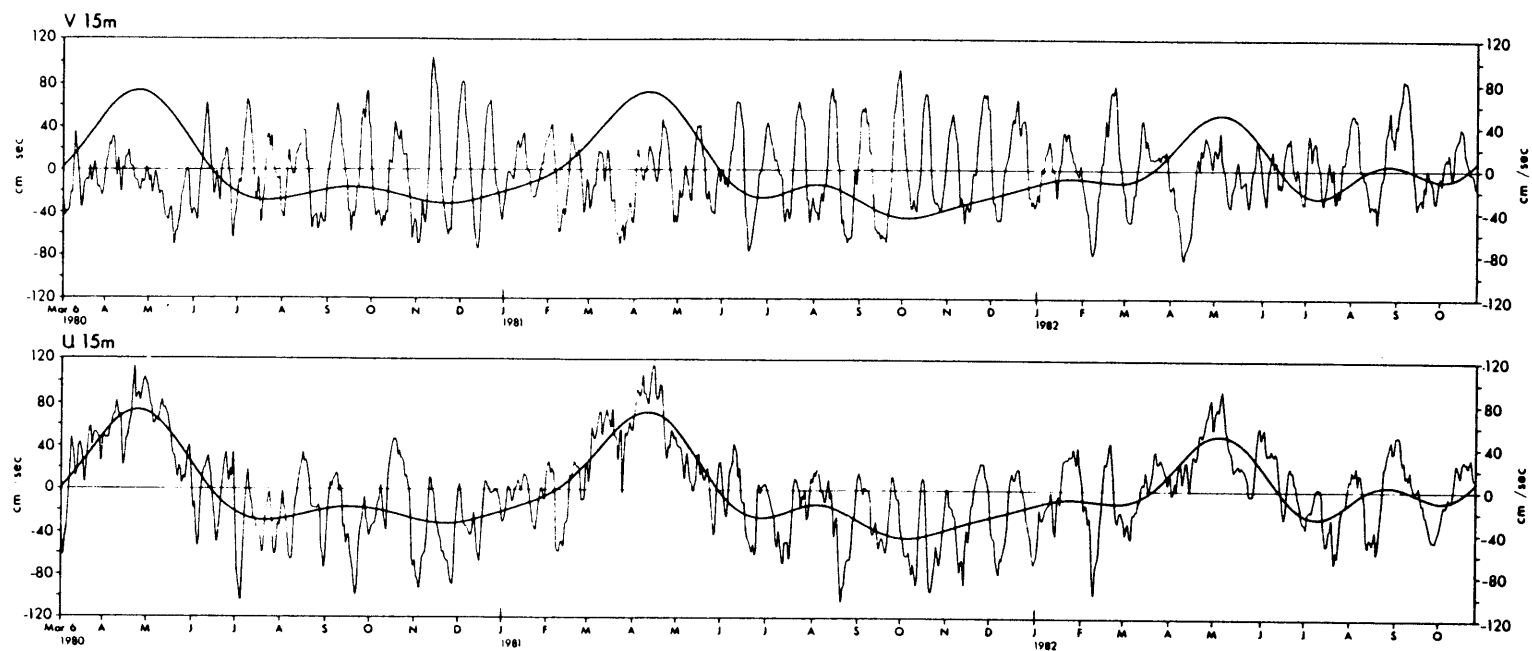


Figure 1.10: Meridional and zonal velocity records at 110°W , 0°N , 15 m depth. A curve of the low-pass filtered (periods $> 100\text{d}$) zonal current is superimposed. (Figure 2 from Philander et al., 1984).

and Wyrtki's combined analysis of drifting buoy trajectories and island sea level records.

In the Pacific, Brady (1987; and detailed in chapter 2 of this thesis) at 110°W, and Halpern, Luther and Knox (1989) at 95, 110, 124, 140 and 152°W, found evidence for the mixed Rossby-gravity wave in moored current meter observations which revealed oscillations in the meridional velocity at 21 day period and 1600 km wavelength, figure 1.10. Westward and upward phase propagation was noted. Large significant fluxes of wave momentum and heat were observed at 110°W, implicating the waves in the large scale low frequency momentum and heat balances.

In the equatorial Indian ocean, Luyten and Roemmich (1984), observed a 26 day oscillation in meridional velocity with an array of moored current meters. The oscillations had westward and upward phase propagation, suggesting downward energy propagation with a zonal wavelength of 1400 km. Analysis of drifting buoy tracks in the western equatorial Indian Ocean revealed meanders of the eastward flowing monsoon drift with the same period (Reverdin and Luyten, 1985).

These waves are strikingly observed in in the SST patterns of both the Atlantic and Pacific versions of the Philander and Pacanowski multi-level primitive equation model (Philander et al., 1986). The models of both oceans recreate the seasonal variability of the large scale circulation, and show that the characteristics of the waves are affected strongly by the mean state. The preliminary report finds that the waves are variable in time and space but appear to be related to the seasonal intensification of the circulation, have westward phase propagation in both ocean models and eastward group velocity in the Atlantic, wavelengths of order 1000 km and periods of order 30 days. An analysis of the energetics was not presented because, according to the authors, it was complicated by the inhomogeneity of the large scale flow and waves. However, the vertical velocity is estimated and found to be large and upward in the troughs of the SST meanders and downward in the peaks, suggesting that the waves accomplish an upward vertical heat flux.

Although a simple description of the observations can be qualitatively compared to the linear mixed Rossby-gravity mode, further analysis yields a more complicated picture. The waves display behavior not expected in

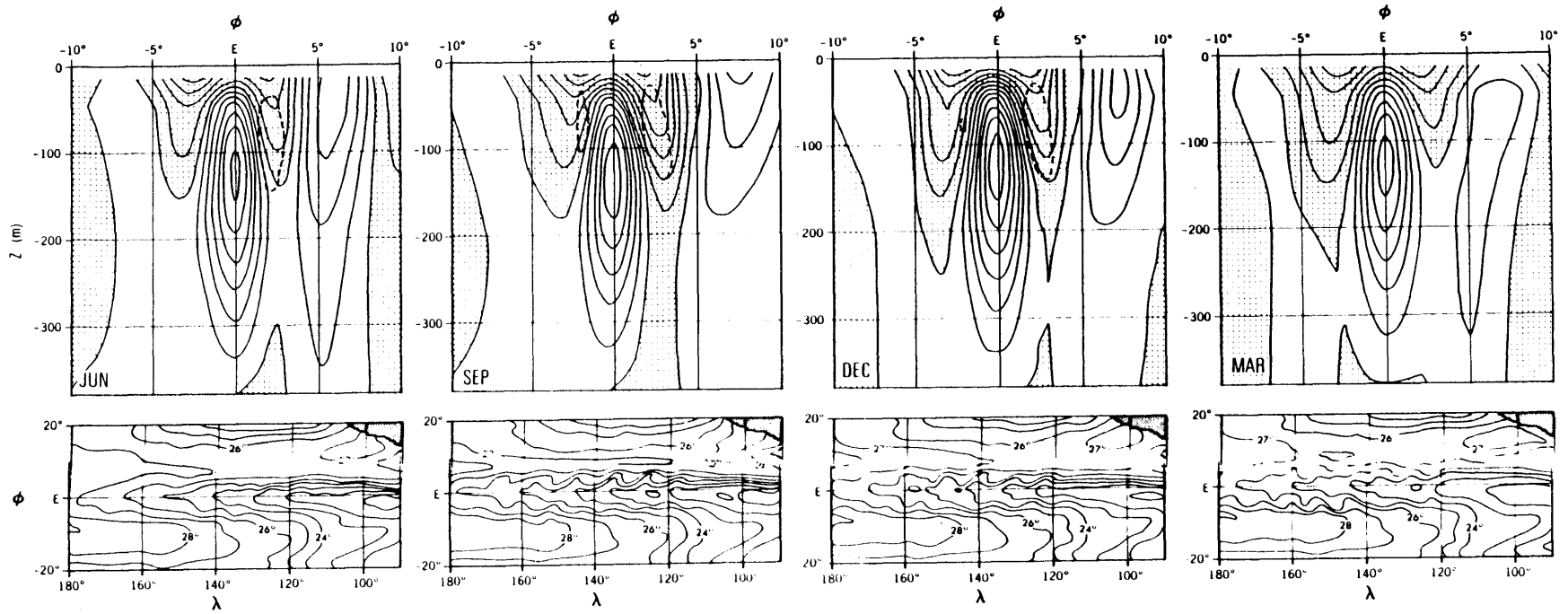


Figure 1.11: Lower panels are surface temperature from the model in the middle of indicated month, with corresponding mean zonal flow in the upper panels. Stippled region is westward flow. Contour interval is 10 cm s^{-1} . Dashed line denotes location of zero absolute vorticity gradient. (Figure 2 from Cox, 1982).

simple linear wave theory. Within a given ocean, wave characteristics such as wavelength, period, amplitude are observed to vary zonally and meridionally. Halpern, et al. (1987), in describing the moored current meter timeseries in the equatorial Pacific, show that though the period changes only slightly by about 4% from the dominant period of about 20 days over the equatorial domain of 110°W to 140°W, the wavelength varies from 1320 km as obtained between 134°W and 140°W, to 1600 km at 110°W.

Deviation from the linear theory is also noted when comparing the behavior of the SST fronts displayed in satellite images to the flow characteristics determined by the moored observations. Halpern et al. (1987) indicate that the relationship of the measured current structure to the motion of the SST front is not as simple as assuming the SST fronts are passively advected by the wave field. At some locations the position of the front corresponds qualitatively well to the measured flow, while at other locations this is not the case. It is also noted that the wavelength and period obtained from observing westward propagation of surface fronts and crest to crest zonal separation, differs from the estimates obtained from the moored time series data. In the examples reported by Legeckis (1987) and Pullen et al. (1987), the SST fronts display wavelengths of about 1000 km and period of about one month, while the moored observations yield a longer wavelength and shorter period over the same time period and location. Furthermore, the waves seem to effect substantial fluxes and flux divergences of heat and momentum which have potentially important consequences for driving the mean flow, for which mixed Rossby gravity linear wave theory is not particularly suited.

Wave Genesis and Energetics

The meridional SST front is formed from the juxtaposition of the eastward flowing warm water of the North Equatorial Countercurrent (NECC) located on the poleward flanks of the westward flowing cold water of the South Equatorial Current (SEC). The cold water near the equator is brought to the surface layer from the depths of the upper thermocline by the eastward and upward flowing Equatorial Undercurrent (EUC). The appearance of these waves along this front appears to be related to the annual

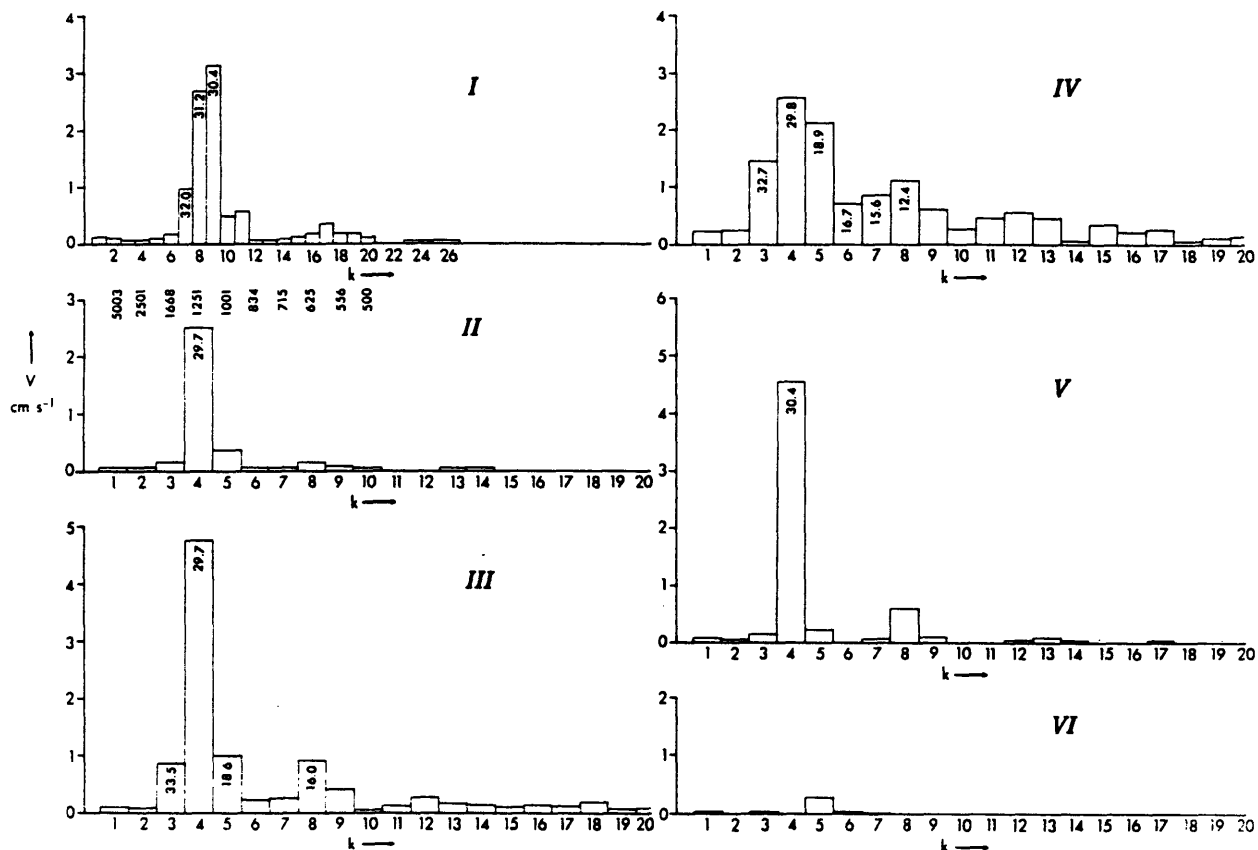


Figure 1.12: Meridional velocity spectra from Cox's (1980) channel model after nine months of integration initiated with random noise. Experiments I to VI are explained in the text. The wavenumber for each band is shown above II and the period of each band is given within each spectral estimate. (Figure 5 from Cox, 1980).

and inter-annual variability of the tropical currents, which is manifested in a strengthening of the lateral shear and consequently the front. During ENSO events when the trade winds are weak, when the velocity shear and the SST front are weak, the waves are not observed in satellite images (Legeckis, 1977) and are weak in current meter records (Halpern et al., 1989). During the phase of the annual cycle when trade winds are strong, when both the lateral velocity shear and the SST front are enhanced, the waves are very energetic.

Existing theory suggests that the zonal current pattern in the equatorial region, characterized by regions of strong meridional shear especially between the NECC and SEC and possibly along the northern and southern flanks of the Equatorial Undercurrent (EUC), is barotropically unstable to fluctuations with the length and time scales of the observed waves (Philander, 1978; Ripa, 1983). If this is the case, energy is converted from the mean flow to the waves primarily through the lateral shear production term. Because the observed modulation in amplitude of the waves is associated with annual cycles in the large scale circulation near the equator, it is thought that these waves are radiated from unstable regions within the currents. The reduced gravity linear stability analysis of Philander (1976; 1978) yielded a most unstable mode (maximum growth rate) which had scales comparable to the observations when realistic basic state shear was used. In addition, observational evidence for the growth of the kinetic energy of the waves by lateral shear production at the expense of the mean zonal flows has accumulated from both the Atlantic and Pacific Ocean current meter array analyses. In the Atlantic at 28°W, Weisberg (1984) observed a northward pulse of eastward momentum, $u'v'$, coinciding with negative meridional shear of zonal velocity which had the appropriate rate of production to account for the observed growth of the wave packet. A more detailed estimate of kinetic energy conversion including all three shear production terms for the narrow 21 day band at 110°W likewise yields a rate adequate to maintain the growth of the waves is calculated in Chapter 4 of this thesis. Furthermore, a growth timescale ranging from two to three weeks is suggested for the eddy band, in agreement with Philander's (1978) theoretical prediction. The analysis presented in Chapter 4 strongly indicates that in the surface layer, at the 20 m level, the positive kinetic energy conversion through the local shear production term associated with barotropic instability of a zonal current, $-\langle u'v' \rangle \partial U / \partial y$, is

nearly compensated by a negative conversion, $-\langle v'^2 \rangle \partial V / \partial y$, due to the term associated with the mean meridional mass divergence driven by the mean poleward Ekman drift. Below the 20 m level, the estimates of this term rapidly decrease to zero, so that the local shear production term dominates and the kinetic energy conversion from the mean flow to the waves yields a net positive conversion to 150 m.

These waves also effect large negative meridional eddy heat fluxes. These southward heat fluxes are associated with a downward sloping mean thermocline to the north, such that the eddy heat fluxes are downgradient. This represents a potential energy conversion from the mean available potential energy of the sloping thermocline into eddy potential energy. This potential energy conversion is much smaller than the conversion of kinetic energy, yet the equatorward eddy heat flux is enormously large compared with the net air sea exchange with the atmosphere, whereby heat is imported into the equatorial region (Bryden and Brady, 1989). Luther and Johnson (1990) have suggested that the meridional flux of heat at 1.5°S, 140°W, measured at a mooring, occurs in pulses when the flow is poleward and the water is anomalously cold, and when the meridional temperature gradient is poleward such that the flux is downgradient.

Philander's original linear stability analysis (1976) suggested that the shear zone between the SEC and the NECC was unstable. However, more recent observations from mooring data at 152°W (Lukas, 1987) and numerical stability analyses (Cox, 1980) place the potentially unstable region within the subsurface shear between the EUC and the SEC, based on the change in sign of the potential vorticity of the mean flow. The stability analysis done by Cox involved numerically examining the waves generated by the instability of a zonal mean flow in a zonally cyclic channel, figure 1.11. Walls, not the usual sponges, were placed at the poleward boundaries at $\pm 20^\circ$ latitude. Initially the flow is perturbed with a meridional velocity which is a random function with all resolvable wavelengths. Experiments (I-VI) were conducted to test the dependence of the growth rate, period, and wavelength of the most unstable mode to vertical (IV) and horizontal (III) diffusion, zonal resolution of the model (I + II), stratification (V) and non-linearity (VI). The resulting spectra are shown for comparison in figure 1.12. The most unstable mode had a wavelength of 1250 km and a period of 29.7 days with the higher resolution of

0.5°, and 1112 km and 30.4 days with the 1° resolution. In both cases the growth rate of the eddy energy was about 2 months. When the coefficients of horizontal mixing of heat and momentum were reduced to one-tenth of the original values, both the eddy energy and the growth rate were slightly enhanced but the period and wavelength remained unchanged. When the vertical momentum mixing coefficient was reduced by one half, reducing the vertical dissipative sink, the flow became nonlinear much more quickly putting energy into neighboring wavenumbers. Reducing the mean vertical stratification, enhanced the growth rate to about 1.5 months. As Philander (1976) predicted, reducing the stratification increases the divergence which tends to destabilize westward jets, such as the SEC, while stabilizing eastward jets such as the EUC. Still, the growth rate of about 1.5 to 2 months predicted here was much slower than Philander's prediction of 2 weeks and the growth rates estimated from the mooring observations at 110°W presented here in Chapter 4. In addition, the rms meridional velocity amplitude after 9 months of integration, is only 3-5 cm s⁻¹, which is an order of magnitude smaller than the amplitudes observed in the real ocean. When the horizontal Reynolds stresses were eliminated in the model formulation, disallowing eddy kinetic energy growth through shear production, the instability was cut off. Only the variability associated with a neighboring higher wavenumber grew very slowly as a result of baroclinic conversion. Thus, lateral shear production was determined to be the primary source of eddy energy growth in Cox's model.

Computing the energy budget of the upper 233 m of the basin (the upper 6 levels in the model), Cox found that an important sink for the growth of these waves is a downward flux of energy due to equatorially trapped vertically propagating wave modes. These waves are excited by the initial disturbance as projected onto the set of equatorially trapped waves. This energy sink was almost as important as vertical friction, which was somewhat larger than horizontal friction. The model showed a similar downward energy flux to that estimated by Weisberg et al. (1984) for the Atlantic. Cox hypothesized that this downward flux of energy is important; it prevents the instabilities from growing so large that non-linear effects would dominate leading to the production of closed rings from highly convoluted meanders, as happens in the Gulf Stream.

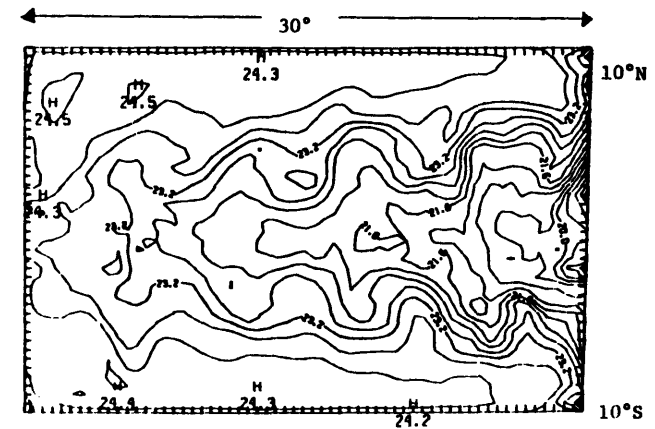
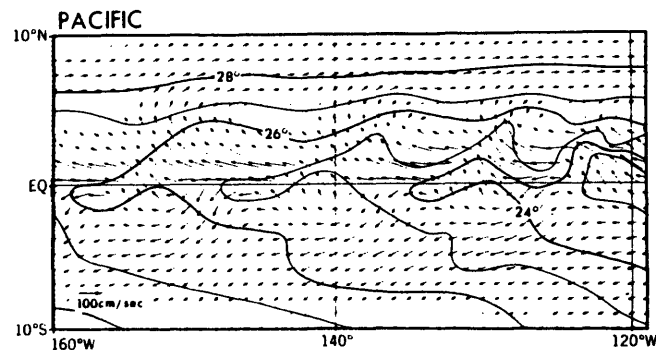
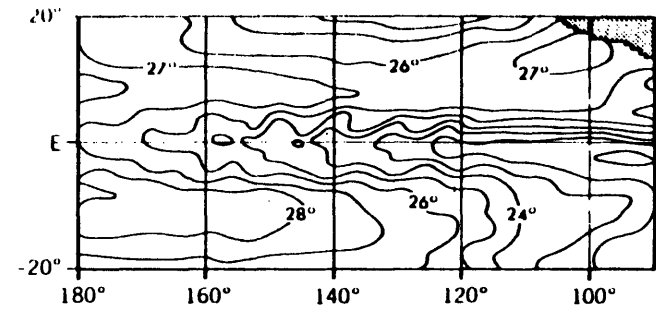


Figure 1.13: Model predictions of sea surface temperature for the (b) Cox model, (c) Philander et al. model (1986), and (d) the Semtner and Holland (1980) model, compared to satellite observations of sea surface temperature (a). (Taken from figure 2, Cox, 1980; figure 3, Philander et al., 1986; figure 6, Semtner and Holland, 1980; and figure 2a from Tropic Heat cover document for Tropical Instability Wave Experiment, 1987).

Evidence for a combination of a mixed Rossby-gravity wave and a first latitudinal mode ($n = 1$) Rossby wave is demonstrated in the meridional velocity field of the near surface layer of the Pacific Basin Cox model. Because of the different behavior in the propagation of energy downward, the waves disperse below the region of excitation and become more distinguishable as they separate since the mixed Rossby-gravity energy travels eastward faster and downward more slowly than the Rossby wave, which is almost at the point where the zonal group velocity is zero, ($\omega k / \beta = -1/2$). Observationally, these waves are hard to differentiate in the near surface arrays. It is possible that the energy in the zonal velocity component observed at the equator at 110°W is due to the $n=1$ Rossby wave, since the mixed Rossby-gravity wave has a zero in zonal velocity on the equator. In order for the $n=1$ Rossby wave to share the same wavenumber and frequency as the mixed Rossby-gravity wave, it must have the vertical structure of a first baroclinic mode.

Semtner and Holland (1980), in a multi-level primitive equation numerical model, found similar evidence of waves radiated by the instability of the large scale equatorial flows. This model differs from the Cox model in that in the off equatorial region the primary source of wave energy is due to baroclinic instability, whereas near the equator in the Undercurrent, the source is primarily due to barotropic instability. The model was forced with steady easterlies, unlike the more realistic monthly varying forcing of the Cox model. The primary wave excited was a first baroclinic mode gravest meridional ($n=1$) mode Rossby wave. This mode, excites a disturbance in the cold tongue which is a series of westward propagating divergences and convergences of the isotherms at the equator at the surface (figure 1.13c), which does not resemble the frontal meandering structure observed in the Legeckis images (figure 13a). In the deeper levels, the model Undercurrent meandered at periods greater than 100 days and the meandering motion could not definitively be related to any equatorial wave mode because the meanders propagated slowly eastward.

This fact about the last model mentioned illustrates one of the drawbacks in comparing the real ocean observations to a variety of available models. It is sometimes obvious which models are useful in understanding the real ocean and thereby appropriate for further application and sometimes it is not. Of the model analyses discussed, all qualitatively resemble the

satellite data to some degree, some better than others as figure 1.13 indicates. But the models differ so much in the formulation, forcing, and physics, that it becomes difficult to isolate a particular model characteristic that is responsible for the differences observed in the solutions. In addition, there is not enough known from observational data analyses yet to obtain an overall picture with enough detail and basic understanding which can be compared definitively to the phenomena observed in the models. Part of the problem is due to the fact that the models are not analyzed like ocean data. Ocean time series data is obtained in specific locations, whereas model solutions tend to be shown as either instantaneous mappings or time histories of various model quantities which are often spatially integrated. Tangible progress will only be achieved when models can be used to bridge the gaps in our understanding produced by the difficulty and expense in obtaining the same amount of real ocean data.

Effect on the Mean Momentum and Heat Balances

In addition to providing an efficient mechanism for radiating energy away from the region of excitation, tropical instability waves are capable of transporting significant amounts of momentum and heat and thus have a strong effect on the mean momentum and heat balance. In the Semtner and Holland model the disturbances produced a large equatorward eddy heat flux which served to warm the cold upwelled water near the equator and cool the warm water off the equator. The equatorward heat flux is down gradient. The diffusivity was estimated to be about $10^8 \text{ cm}^2 \text{ s}^{-1}$. In the mean momentum balance, the eddies produced a negative divergence of the Reynolds stress, which was large at the core of the EUC, such that the eddies decelerated the eastward flow of the EUC core. Below the core, a smaller accelerative effect is observed. An eddy diffusivity for momentum was estimated at $2 \times 10^7 \text{ cm}^2 \text{ s}^{-1}$.

These eddy-driven effects in numerical models are comparable to the direct measurements by current and temperature time series at 152°W and 110°W by Bryden and Brady (1989). They show that the largest effect on the mean momentum balance is through the Reynolds stress divergence term, $-\partial\langle u'v' \rangle / \partial y$, which when integrated over the vertical extent of the current meter mooring, acts as an equivalent westward stress of -0.21 and

-0.12 dynes cm^{-2} , at 110 and 150°W respectively. The average estimate from these arrays, -0.16 dynes cm^{-2} , compares well to the residual in the mean zonal momentum balance involving only the mean terms, -0.11 dynes cm^{-2} obtained on the equator from the mean diagnostic model of Bryden and Brady, (1985). Hansen and Paul (1984) presented a much larger equivalent stress estimate of -0.31 dynes cm^{-2} , obtained from an analysis of the tracks of drifting buoys drogued at 50 m. For comparison, the wind stress in the region is about 0.5 dynes cm^{-2} , so the wave stresses are appreciable.

In the mean heat balance, the waves are found to transport equatorward enormous amounts of heat. Bryden and Brady found an equivalent net heating of 95 W m^{-2} at 152°W and 380 W m^{-2} at 110°W, integrating the eddy flux divergences from the surface to the deepest measurement. This enormous heating is much larger than the observed surface heat gain from the atmosphere, which is in the range from 50 to 85 W m^{-2} . From the meridional eddy heat convergence in the numerical model of Philander et al. (1986), a heat gain on the order of 100 W m^{-2} is indicated. Hansen and Paul find 180 W m^{-2} in the drifter analysis. Imawaki et al. (1988) find that the daily mean convergence of heat in the surface layer, as indirectly estimated from a residual heat balance with mooring measurements, is large and fluctuated with a period ranging from 15 to 20 days during the analysis period. It cannot be determined from these early observational efforts whether or not the enormous net heating implied by all these estimates is compensated at any specific depth by vertical divergence of the vertical eddy heat flux, or by some other process such as mean advection. It must be partially compensated because such a large local heat content change is not observed.

TABLE 1.1: A Comparison of Mixed Rossby-gravity Wave Observations

A: OBSERVATIONS IN THE OCEAN

OCEAN	OBSERVER (comments)	$2\pi/\omega$ (days)	$2\pi/k$ (km)	$\omega k/\beta$
ATLANTIC	Duing et al., 1975. (GATE)	16	2660	-0.47
	Weisberg, et al., 1979. {5} (SEQUAL, Gulf of Guinea) [$c = 0.5 \text{ m s}^{-1}$, $\omega/k = -0.46 \text{ m s}^{-1}$]	31	1220	-0.52
PACIFIC	Harvey and Patzert, 1976. (near Galapagos Isl., 2 month series of bottom current and pressure)	25	1020	-0.8
	Legeckis, 1977. (satellite IR images of SST wave crests)	20-30	1100	-0.6-0.7
	Wyrski, 1978. (4°N , 159°W ; in NECC; period from Island sea level and wavelength from Drifting Buoy paths)	34	1100	-0.53
	Brady, 1987. {4} (0°N , 110°W ; 20-250m EPOCS current meter array, $c = 1.3 \text{ m s}^{-1}$, $w/k = -0.9 \text{ m s}^{-1}$)	21	1660	-0.57
	Halpern et al., 1988. (EPOCS, and TROPIC HEAT current meter arrays at 95°W , 110°W , 124°W , 140°W , 152°W)	20	1600	-.62
INDIAN	Luyten and Roemmich, 1984.	26	1400	-.54
MODELS	Cox 1980. {2} (Pacific Simulations, seasonal wind forcing)	30	1250	-.53
	Semtner and Holland, 1980. (Steady winds)			
	Philander, Hurlin and Pacanowski, 1986. (Pacific and Atlantic simulations, monthly mean winds)	30	1000	-.66

TABLE 1.1B: OBSERVATIONS IN THE ATMOSPHERE

ATMOS- PHERE	Yanai and Maruyama, 1966. (stratosphere)	5	4	-.4
	Zangvil and Yanai, 1980. {1} (200 mbars)	4-5	4	-(.4-.5)
	Yanai and Lu, 1983. (200 mbars)	5	4	-.5
MODEL	Mak, 1969. {3}	4	4	-.5

Table 1.1: A list of observations of mixed Rossby-gravity waves in the ocean, the atmosphere, and numerical models. The numbers appearing in brackets denote the corresponding points in figure 1.14.

1.5 SUMMARY AND FINAL REMARKS

As has been discussed, the gravest symmetric meridional velocity mode, the mixed Rossby-gravity wave is widely observed in all equatorial regions. It appears to be intrinsically involved in the large scale circulation processes of both the atmosphere and the ocean. In the atmosphere, the waves contribute to driving the quasi-biennial oscillation. In the ocean, the waves appear to transport significant fluxes of heat and momentum, but the overall picture of the wave-mean flow interaction is much less certain. In the ocean it appears that the waves derive their energy from the mean flow through the process of instability whereas in the stratosphere and upper troposphere, the waves feed energy into the mean flow and possibly derive their energy from lower layers of the atmosphere or from mid-latitude radiation.

Table 1.1 brings together the existing observations of mixed Rossby-gravity waves in the atmosphere, the oceans and numerical models, listing parameters by which all observations can be compared such as the wavelength $2\pi/k$, the period ω , and a comparative parameter, $\omega k/\beta$. The observations listed in Table 1.1 have been identified as the mixed Rossby-gravity wave due to similarities between the simple linear wave theory and the observed kinematical behavior. Though the characteristics of the medium of propagation--the large scale, slowly varying mean state--vary in detail, a similarity is noted in the value of the parameter, $\omega k/\beta$, which for nearly all observations approaches a value of $-1/2$. Strictly, in linear theory with no mean flow, the mixed Rossby-gravity wave curve has no special point at $\omega k/\beta = -1/2$, where, for the Rossby and inertio-gravity waves, the group velocity is zero. In addition, the similarity between all observations in Table I is obvious only in non-dimensional wavenumber-frequency space, Figure 1.14. Figure 1.14 plots the observations in Table I for which statistically confident and independent estimates of both the zonal and vertical phase speeds allow the non-dimensionalization of the wavenumber and frequency. The observations cluster near the point on the non-dimensional mixed Rossby-gravity wave curve, $(s, \sigma) = (-\frac{1}{\sqrt{2}}, \frac{1}{\sqrt{2}})$. It is easy to understand why the wave is preferentially observed in the numerical models, particularly those with walls placed in the midlatitudes. It is a zero zonal group velocity mode

for free waves in these models. It is harder to understand why the observed waves in the atmosphere and oceans cluster near this point and moreover, why there is such similarity between the waves observed in the different media.

Unfortunately, most of the theoretical work on this problem, is based on a zonally-constant basic state, with either meridional or vertical shear, or is modeled by a reduced gravity, one and a half layer theory. In reality, this basic state is too simplistic for comparison with the observations. All of the equatorial oceans contain swift, slowly-evolving currents and thermal structures that are strongly sheared both meridionally and vertically. Thus, numerical models with large scale flows which are nearly as complicated as those of the real ocean are appealing. To be adequate for studying this problem, the numerical circulation must be in constant transition from one forced state to another as is the case of annual forcing in the Pacific; the model currents must be strongly sheared both vertically and laterally and as well as have zonal variations; and it must be possible for the mean flow to be three dimensionally non-divergent, as is the case for the Undercurrent which has an associated mean vertical and meridional velocity fields. There has been some theoretical success with the long wave approximation in understanding wave-mean flow interaction with Kelvin, Rossby, and Inertio-gravity waves (McPhaden et al., 1986; McPhaden and Knox, 1979; Philander, 1979; Boyd, 1978; Proehl, 1988). However, this theory is not appropriate for the observed mixed Rossby-gravity wave, which is not a long wave but a mesoscale wave where the wavelength scales as $2\pi L_d$, where $L_d \sim 250$ km.

Many questions regarding the genesis of these waves and their importance to the evolution of the circulation in the equatorial oceans remain unanswered. For instance, why is there a similarity in the dispersion characteristics of the waves observed in the atmosphere, the oceans and in models? It is curious that, within the observational errors expected, linear equatorial wave theory with no mean flow can describe the observations reasonably well, even though the mean flow is strong, variable and differs from ocean to ocean to atmosphere. The controversy surrounding the genesis of the Yanai-Maruyama waves observed in the atmosphere is not yet resolved either.

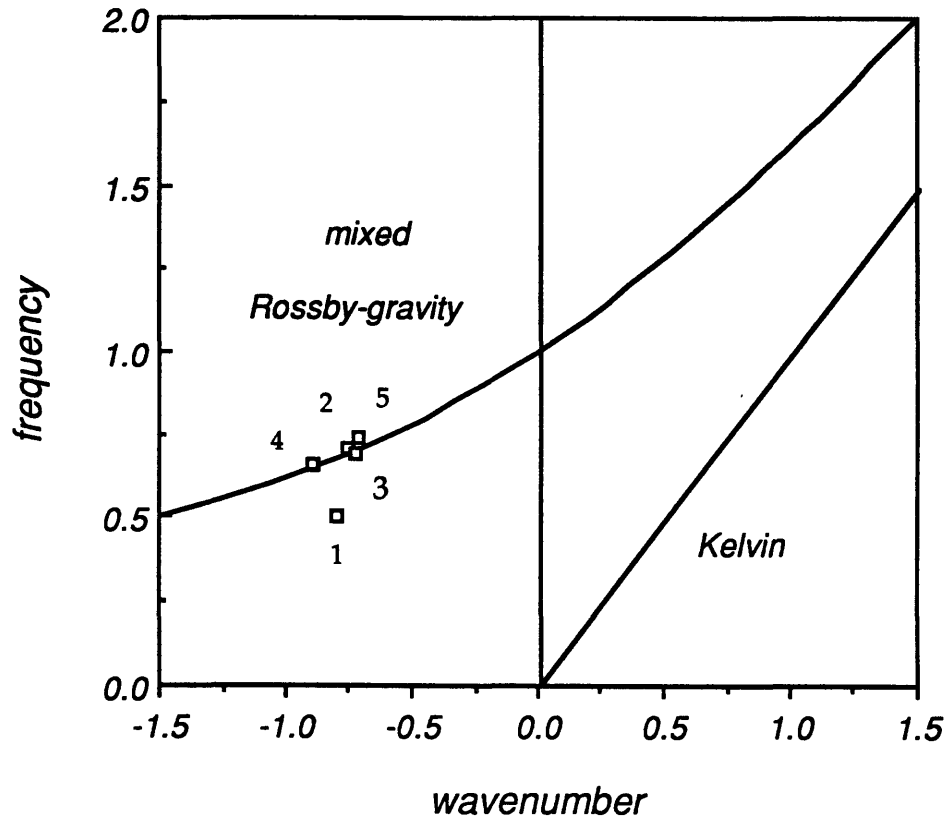


Figure 1.14: Nondimensional dispersion curves for the mixed Rossby-gravity and Kelvin waves. Plotted points of zonal wavenumber and frequency correspond to a subset of the observations listed in Table 1 for which independent estimates of the vertical phase speed are obtained. See table 1 for identification of observation. The cross indicates the observed frequency bandwidth (periods from 36.8 to 14.2 days) and error in zonal wavenumber estimate associated with the observation of point #4.

To explain the ubiquitous region on the dispersion curve, it might be speculated that the presence of a sheared mean flow triggers this particular wave mode preferentially like a resonance. This can be seen for the case where the mean flow is only a function of latitude. Then, the meridional structure equation for $V(y)$ with the inclusion of a laterally sheared mean flow can be derived from the wave equations of the Appendix and is written,

$$V_{yy} + \{ \omega_o^2/c^2 - k^2 - k\beta^*/\omega_o - f^{*2} \} V = \frac{2U_y k \omega_o}{(\omega_o^2/c^2 - k^2)} \{ V_y - \frac{\omega_o^2/c^2 + k^2}{2k\omega_o} f^* V \}$$

where $\omega_o = \omega - Uk$, $f^* = f - U_y$, $\beta^* = \beta - U_{yy}$, and c is the separation parameter as before. Note that with lateral shear U_y included, the left hand side of the equation looks the same as the regular meridional structure equation except that ω is replaced by ω_o , f is replaced by f^* , and β is replaced by β^* . Also, new terms appear on the right-hand side which are proportional to U_y and inversely proportional to $\omega_o^2 - k^2c^2$. Thus, when $\omega_o^2 - k^2c^2 \approx 0$, the term on the right hand side is very large. However, for a constant non-zero shear U_y , a solution can be found that both satisfies the right and left sides separately when $\omega_o = -kc$. Thus, the solution must make the numerator of the right-hand side identically zero and also be a solution of the left hand side, that is it must be an equatorial wave. This is possible for the mixed Rossby-gravity wave. With the numerator on the right hand side set to zero at $\omega_o = -kc$, V must satisfy,

$$V_y + \frac{f^*}{c} V = 0.$$

For a constant U_y , such that $\partial/\partial y = \partial/\partial y^*$ since $y^* = y - \frac{U_y}{\beta}$, $\beta^* = \beta$, and $f^* = \beta y^*$,

$$V(y^*) = V_o \exp \left\{ -\frac{\beta}{2c} y^{*2} \right\},$$

which is a modified solution of the mixed Rossby-gravity wave with y replaced by y^* and hence is a solution to the left hand side as well. Thus, for this oversimplified case, the mixed Rossby-gravity wave separately satisfies both sides of the equation, when $\omega_o = -kc$. Furthermore, the mixed Rossby-gravity wave is the only equatorial wave which can accomplish this, since it

has the only dispersion curve to intersect the line $\omega_0 = -kc$. The intersection occurs at the point $\omega_0 k / \beta = -1/2$.

Another way of preferentially exciting the mixed Rossby-gravity wave mode at the site where $\omega k / \beta = -1/2$, can be heuristically viewed by considering the free equatorial wave solutions for a region forced externally at walls placed at a northern and southern boundary. Then, the free mixed Rossby-gravity dispersion curve splits into two curves, each with an inflection at the point $\omega k / \beta = -1/2$ as discussed by Cane and Sarachik (1979). This point is a zero zonal group velocity point. Thus, if the region were forced by incoming midlatitude radiation, energy would tend to build near this point as resonances occurred. This scenario was modeled numerically by Mak (1969) for a two-layer atmosphere, as discussed earlier, and peaks in the energy spectrum were observed at these points.

A problem with this scenario is that it implies that energy must be supplied from extra-equatorial regions. This is in opposition to what is observed—that the energy for the maintenance of the waves is locally generated through lateral shear instability of the large scale flow as discussed here in Chapter 4 and shown by Weisberg (1984) for the Atlantic Ocean. It may be that the instability is triggered by this resonant wave, and then additional feedback results for continued growth. Cox (1980) in his numerical stability analysis, however, observed that the mixed Rossby-gravity wave was generated without lateral forcing but not without the non-linear advection terms which couple the mean flow and wave energetics through the conversion terms. He speculated instead that the mixed Rossby-gravity wave was possibly excited by the instability in the unstable surface layer, and then, along with the gravest latitudinal mode ($n=1$) Rossby wave, propagated energy downward into the deep ocean where it could be effectively dissipated.

Chapters 4 and 6 of this thesis discuss the role of the waves observed at 110°W in the energetics of the equatorial ocean. Essentially, when the winds are westward, the winds continually pump energy in the form of available potential energy stored in the east-west sloping thermocline. Some of this energy is removed by turbulent dissipation in the mixed layer. But in order to achieve a steady state in the upper ocean, the remaining energy input must be balanced by either a downstream increase of kinetic energy, turbulent dissipation, conversion to eddy kinetic energy or export out of the upper

ocean. In the western Pacific ocean, the available potential energy can be converted into a downstream increase in mean kinetic energy since the velocity of the Undercurrent increases as it flows eastward. However, the kinetic energy of the Undercurrent in the central Pacific remains fairly constant and starts to decrease approaching the eastern boundary. By the time it has reached the central and eastern Pacific, it has attained enough speed that the lateral shear with the westward flowing South Equatorial Current is large enough to become unstable. The instability process near the equator is not well understood theoretically. At this point mean kinetic energy can be converted to kinetic energy of the waves by the work of the waves against the mean shear. To limit the growth of the waves, energy is radiated vertically into the deep ocean and ultimately dissipated.

Because of the comparisons to the atmospheric waves, it is interesting to speculate whether or not there is a net effect on the slowly varying large scale ocean mean flow, as there is in the atmosphere in driving the QBO. In other words, are these waves somehow involved in ENSO? The waves disappear during the ENSO, and reappear soon after the normal structure of the thermocline and circulation returns. At present, it is not known what effect the waves have on the large scale currents on interannual timescales. To investigate this problem, it will be necessary to establish long records over a wide region of the equatorial Pacific. The necessary degree of observational sophistication will not occur for some time given that there are no plans for such an array in the immediate future. A problem more easily investigated is whether these vertically propagating waves drive the deep jets. It would seem that much smaller arrays with good vertical resolution or instrumented with profiling current meters may provide some answers in this direction, but again no such arrays are being planned. Currently, our investigations based on available data sets are just at the point where we can estimate some of the effects of these waves at a single location in the surface layers. An evaluation of the effects over the whole domain of an equatorial ocean basin and with better depth resolution is ultimately required to answer these questions.

CHAPTER 2:

Interpretation as an Equatorial Wave

2.1 INTRODUCTION

Linear equatorial wave theory has been found to be a useful tool in identifying and understanding the observed equatorial variability. Wunsch and Gill (1972) were first to identify peaks in the sea level spectrum at island stations across the equatorial Pacific Ocean, as low baroclinic mode equatorial inertio-gravity waves with zero group velocity. Knox and Halpern (1982), recognized the near nondispersive behavior of a pulse in eastward transport, which travelled eastward at a speed of about 3 m s^{-1} past three equatorial moorings located at 152°W , 110°W , and 95°W , as a first baroclinic mode Kelvin wave, possibly forced to the west of the observed sites by a wind relaxation event. Lukas and Firing (1985) associated the gravest meridional mode annual Rossby wave with the annual temperature variability observed below the thermocline in the central Pacific Ocean in CTD casts taken over 16 months during the NORPAX Hawaii-to-Tahiti Shuttle experiment. Literature contains many other examples where simple linear equatorial wave theory seems adequate to describe at least qualitatively the observed behavior of equatorial variability in both the oceans and atmosphere. Here the propagation characteristics of the 21 day wave oscillations are determined and compared with the propagation characteristics of linear mixed Rossby-gravity waves.

The variability under discussion here appears in satellite images as a train of waves propagating westward along the upwelling front, figure 1.13(a). Variability with similar structure and propagation characteristics is observed in the other equatorial oceans as well as the tropical atmosphere, and tentatively has been identified as a mixed Rossby-gravity wave. Here the waves appear as large oscillations in moored time series of meridional velocity and temperature with a significant peak in the spectral domain at a

central period of 21 days. These observations will first be discussed in terms of the vertical and meridional structure of the wave variance. Next, the horizontal and vertical phase propagation is determined in order to estimate both zonal and vertical wavenumbers of the disturbance. Comparison of the propagation characteristics of the 21 day variability with the dispersion curves from linear equatorial wave theory shows that the phase propagation behavior is consistent with a vertically propagating mixed Rossby-gravity wave. Though the structure of the wave field does not strictly follow the behavior expected for a simple linear equatorial wave, the similarities are striking.

2.2 DATA

The velocity and temperature time series featured here are obtained from a triangular current meter mooring array deployed at 110°W as part of the Equatorial Pacific Ocean Climate Study (EPOCS; Freitag et al., 1987, Halpern, 1987). Two of the moorings are located about 0.5° latitude north and south and about 1° longitude west of the third mooring located on the equator. Table 2.1 provides the details of the spatial configuration and temporal information of the array. On each mooring, vector-averaging current meters were placed at the nominal depths of 20, 50, 75, 100, 150, 200, and 250 m.

Numerous EPOCS moorings were deployed continuously at this location from 1979 to 1983. The particular records used in this study were chosen because they are the group of longest records that gave the best spatial resolution. Many of the other settings of the triangular array have gaps in time and missing records at key depths. The records discussed here are from the original hourly records that were first low-passed with a 24 hour half-width gaussian filter. For all of the calculations reported here, the two shorter pieces were first joined by linearly interpolating over the 2 to 3 day gap, and then depending on the purpose of the calculation shorter lengths were used. Since all but the first 12 days of the T16 record are lost, for the calculation of the horizontal distribution of eddy fluxes and for the horizontal cross-correlation, a 184 day long piece beginning on August 13, 1980 is used at all

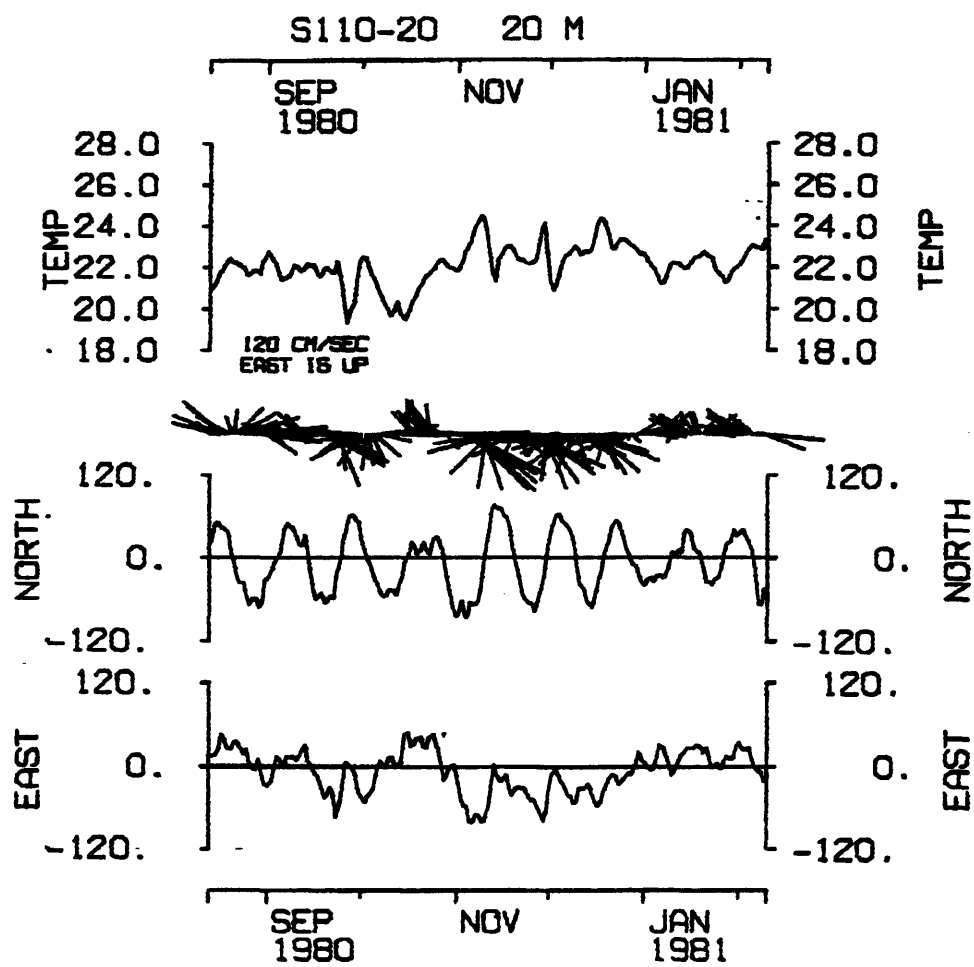


Figure 2.1: Timeseries of east and north velocity and temperature at 110°W, 30°S.

locations. For vertical cross-correlations, the longer 312 day long piece is used at the equatorial mooring.

The meridional distance between the northern and southern moorings is 59.3' latitude or 110 km, and the zonal distance between the average zonal location of the northern and southern mooring and the equatorial mooring is about 54.9' longitude or 102 km.

For descriptive purposes, the 20 m 184 day long record on the southern mooring is displayed in figure 2.1. The large amplitude (30 cm s^{-1}) oscillations in both the meridional and zonal velocity time-series of the 20m record in figure 2.1, are the central focus of this work. The energy preserving spectrum of the variance in the meridional and zonal velocity components (figure 2.2a) demonstrates a large peak observed at the central period of 20.4 days over a bandwidth corresponding to periods from 14.2 to 36.8 days. The meridional velocity spectrum from a longer record of 312 days shows that the peak is actually much narrower, with the central period closer to 21 days (at 20.8 days) over a bandwidth from 22.3 to 19.5 days ($14/312$ to $16/312 \text{ d}^{-1}$).

TABLE 2.1

SPATIAL AND TEMPORAL DESCRIPTION OF THE ARRAY AT 110°W

Northern deployments, T12 and T14:

T12 : August 11, 1980 to January 29, 1981 171 days

Lat. 0° 29.4' N

Long. 110° 29.1' W

T14 : February 2, 1981 to July 6, 1981 154 days

Lat. 0° 32.5'N

Long. 110° 30.3'W

Equatorial deployments, T8 and T15:

T8 : August 10, 1980 to February 4, 1981 172 days

Lat. 0°

Long. 109° 33.5'W

T15 : February 7, 1981 to July 8, 1981 151 days

Lat. 0° 0.6'N

Long. 109° 33.8'W

Southern deployments, T11 and T16 :

T11: August 13, 1980 to February 2, 1981 173 days

Lat. 0° 29.9'S

Long. 110° 28.3'W

T16: February 4, 1981 to February 16, 1981 12 days

Lat. 0° 31.1'W

Long. 110° 30.0'W

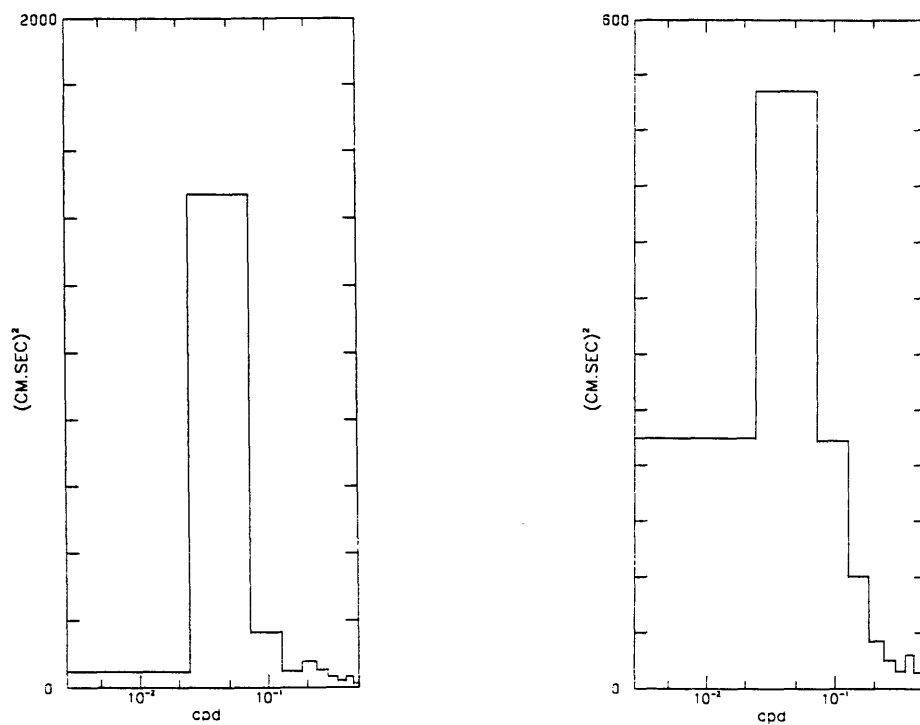


Figure 2.2: Energy preserving meridional velocity spectrum (a) and Zonal velocity spectrum (b) for the 184 day timeseries at 110°W at the equatorial location at 20 m depth.

2.3 HORIZONTAL PHASE PROPAGATION

Cross-correlation of records of spatially separated instruments supply phase differences which indicate both the direction in which the phase of the disturbance propagates and, assuming one wave or narrow wave number band wave packet is associated with an individual frequency band, the central wavelength of the disturbance. In general, the three-dimensional wave-number vector of the disturbance \mathbf{k} , equal to (k, l, m) , where k , l , and m , are wavenumbers in the east, north and vertical (x, y, z), directions respectively, is related to the phase difference ϕ , between two spatially separated records, at locations \mathbf{x}_1 and \mathbf{x}_2 respectively, by

$$\phi = \mathbf{k} \cdot (\mathbf{x}_1 - \mathbf{x}_2).$$

Then the east-west wavenumber k and the north-south wavenumber l , can be determined from coherent phase differences obtained in the triangular array from cross-spectra of records at the same depth level. At least three records at each depth level are needed. To obtain the best possible estimates of phase differences between records, averaging over a wide frequency band is necessary. The band chosen, encompassing periods in the range of 36.8 to 14.2 days, centered at 20.4 days, allows for 18 degrees of freedom in the calculation using the 184 day long record which covered the period during which the oscillations are most energetic. For this number of degrees of freedom, the coherence must exceed 0.56 in order to be significantly different from zero at the 95% confidence level.

Results

Table 2.2 lists the velocity the coherence and phase of the cross-spectral estimates for the frequency band above, using the horizontally spaced records in the triangular array. In zonal velocity, except at the 20 m, 50 m and 250 m triad of records, the coherence of the cross-spectra of the zonal velocity records (figure 2.2b, $u \times u$) was not significant at the 95% confidence level. Only the cross-spectra of the temperature records at 20m gave at least the two estimates significant at the 95% confidence level necessary for an estimate of the zonal wavenumber. However, for the cross-spectral estimates for zonal velocity and temperature, the phase difference errors tends to be the same order as the phase. For this reason, only the results obtained with the meridional velocity

records are used to determine the horizontal wavenumber estimate, since the coherences are all very high and thus the phase errors relatively low.

The cross-spectral analysis of the meridional velocity records for all possible pairs at each depth, is shown in figure 2.2a. A positive phase difference signifies that the second record leads the first. Thus the convention adopted is that a positive zonal phase difference implies westward phase propagation. A complete triad is necessary to determine both the meridional and zonal phase speeds. Complete and highly coherent current meter triads are located at the 20, 50, 100, and 250 m levels. Negligible north-south phase propagation is observed at all depths within errors. The zonal phase differences obtained at these four levels of 23.5°, 26°, 18°, and 23.5°, respectively show little variation, and indicate consistently westward phase propagation. For a single estimate for the array, a coherence weighted expectation value yields an average zonal phase difference of 22.6° ($\pm 7^\circ$). With a zonal separation between moorings of 104 km, an average zonal wavelength of 1660 km is obtained. Converting the phase error into an error in wavenumber of $\pm 1.16 \times 10^{-3} \text{ km}^{-1}$, gives a range of wave length from 2400 to 1270 km. The resulting westward phase speed is $-94 (\pm 30) \text{ cm s}^{-1}$ for the central period of 20.4 days.

It is noted that the 20m, 50m and 250m level cross-correlations in the east velocity component give 22.5, 14.5°, and 5° respectively, and the 20m temperature cross-correlation gives 13.5°. Though the errors in phase are much larger, these results are consistent with the results from the meridional velocity component within errors.

TABLE 2.2: HORIZONTAL CROSS-CORRELATIONS OF U, V, and T:**(a)**

V x V	N x E		E x S		N x S	
depth (m)	Coh	$\phi(^{\circ})$	Coh	$\phi(^{\circ})$	Coh	$\phi(^{\circ})$
20	<u>.98</u>	26/6	<u>.98</u>	-21/5	<u>.96</u>	6/9
50	<u>.99</u>	30/5	<u>.98</u>	-22/5	<u>.98</u>	9/5
75					<u>.90</u>	5/15
100	<u>.91</u>	25/14	<u>.92</u>	-11/13	<u>.90</u>	14/15
150	<u>.93</u>	22/12				
200					<u>.90</u>	3/15
250	<u>.96</u>	22/9	<u>.95</u>	-25/10	<u>.95</u>	-1/10

(b)

U x U	N x E		E x S		N x S	
depth (m)	Coh	$\phi(^{\circ})$	Coh	$\phi(^{\circ})$	Coh	$\phi(^{\circ})$
20	<u>.96</u>	22/9	<u>.91</u>	-23/14	<u>.84</u>	2/20
50	<u>.84</u>	38/20	<u>.66</u>	9/37	.35	64
75					.45	-116
100	<u>.91</u>	-3/14	.39	-94	.40	-124
150	<u>.62</u>	-6/42				
200					.49	-29
250	<u>.67</u>	40/36	.50	8	<u>.63</u>	70/41

(c)

T x T	N x E		E x S		N x S	
depth (m)	Coh	$\phi(^{\circ})$	Coh	$\phi(^{\circ})$	Coh	$\phi(^{\circ})$
20	<u>.91</u>	27/14	<u>.72</u>	0/30	.5	40
50	<u>.90</u>	34/15				
75					.55	47
100			.30	65		
150	.47	30				
200					.1	70
250	.21	-35	.22	-69	.23	40

Table 2.2: Horizontal cross-spectral analysis for the 36.8 to 14.2 d band of variability, obtained from the 184 d records. The coherence, phase difference, and phase error are listed for (a) north velocity V, (b) east velocity U, and (c) temperature T. A positive phase difference means that that the second record leads the first. Record pairs that are significantly coherent at the 95% confidence level, with a coherence greater than 0.56, are underlined.

2.4 VERTICAL PHASE PROPAGATION

Evidence for vertical propagation is observed as a coherent phase difference between 2 records separated vertically. The coherence and phase difference for this calculation are obtained from the 312 day records of meridional velocity on the equatorial mooring. Cross-spectral analysis is performed by piecewise averaging three 104 day long pieces giving an estimate at 20.8 days, with no subsequent frequency band averaging. With 6 degrees of freedom, all meridional velocity cross-spectra are significantly different from zero at the 95% confidence level with coherence values exceeding 0.88 except the 20 x 2 50 and 50 x 250 estimates, however those estimates are significantly different from zero at the 80% confidence level. Again, only the meridional velocity record is considered here because the cross-spectra of the zonal velocity records showed dramatic decreases in coherence with increasing depth separation, such that non-coherent estimates were obtained for many record pairs. The phase errors shown are calculated using the confidence limits at 80%.

Results

For all meridional velocity record pairs except those involving the record at 20 m, the deeper record leads the shallower (Table 2.3), which lists the vertical phase difference and coherence. This is a signature of upward phase propagation and hence, for a disturbance composed of a single equatorial wave, downward propagation of energy. This phase difference increases uniformly with separation.

These results can be interpreted within the context of simple equatorial wave theory. The behavior of the vertical propagation of linear, equatorial waves with no mean background flow is described by the vertical structure equation,

$$\frac{d^2G}{dz^2} + \frac{N^2(z)}{c^2} G = 0,$$

and appropriate boundary conditions, where G is the vertical structure function, c is the parameter used to separate the vertical structure equation from the meridional structure equation, and $N^2(z)$ is the mean buoyancy profile which is allowed to vary slowly as a function of depth in the WKB approximation. If this approximation is valid for the ocean regime measured here, vertically propagating plane wave solutions to the above equation will have a slowly depth-varying vertical wavenumber, $m(z)$. The vertical phase difference, $\Delta\phi$, between two depths z_1 and z_2 , is locally approximated as:

$$\Delta\phi = \frac{1}{c} \int_{z_1}^{z_2} N(z') dz',$$

with c determined by the meridional structure equation given the observed ω and k . If one vertically propagating wave is present and if the WKB approximation is valid, an alternate estimate for c can be obtained using all phase differences observed. To do this, the observed vertical phase differences can be fit to the corresponding integral of the mean N^2 profile, calculated using the 3 year mean EPOCS CTD data at 110°W, which encompassed the duration of this record, and integrated using a simple trapezoidal scheme. Consistency with the value of c estimated from the dispersion relation of the meridional structure equation for the observed ω and k , is expected for a vertically propagating meridional mode.

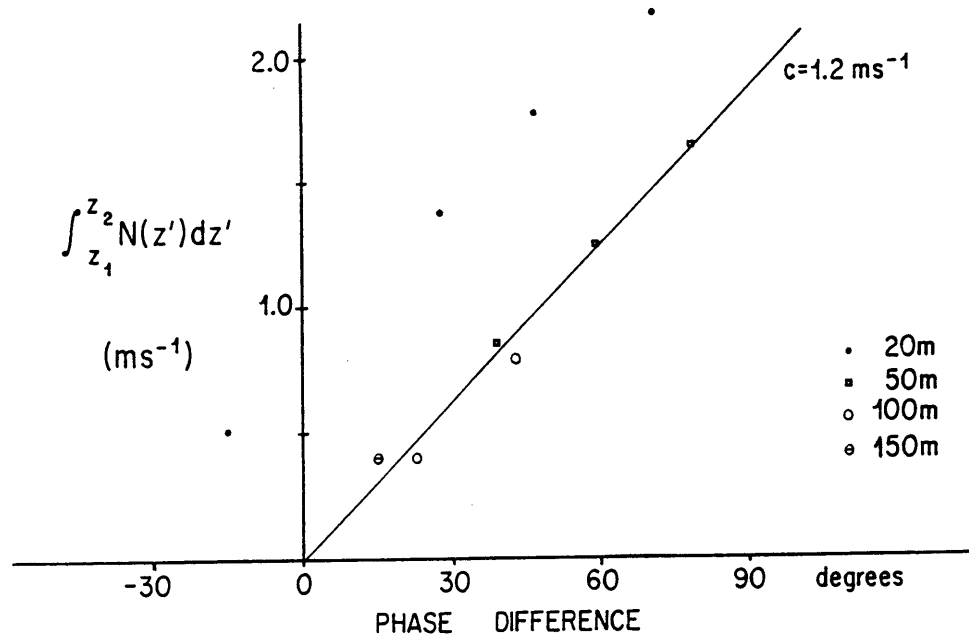


Figure 2.3: Plot of the integrated buoyancy profile versus the north velocity phase differences between instrument levels on the equatorial mooring at 110°W.

TABLE 2.3 VERTICAL CROSS-SPECTRAL ANALYSIS

$V(z_1) \times V(z_2)$	coh	$\phi(^{\circ})$	$\int_{z_1}^{z_2} N(z') dz'$
20 x 50	.96	-15/13	0.53
x 100	.95	28/15	1.38
x 150	.94	47/17	1.78
x 250	.80	71/35	2.18
50 x 100	.92	39/19	0.86
x 150	.94	59/15	1.25
x 250	.78	78/38	1.65
100 x 150	.98	23/9	0.40
x 250	.95	43/14	0.80
150 x 250	.92	16/19	0.40

Table 2.3: Cross-spectral analysis of the meridional velocity record between records separated in depth on the equatorial mooring. Coherence, phase difference and error, for the frequency band centered at 20.4 days, and the integral of the buoyancy period between two depths are tabulated. A positive phase difference indicates that the deeper record leads the shallower record.

Figure 2.3 shows all phase differences plotted against the corresponding integral of the buoyancy profile. There appear to be two distinct groups of points. Those obtained from cross-correlations using the 20 m record as one of the two record pairs appear biased toward a smaller phase difference or larger buoyancy profile integral. They do however, exhibit the same slope as the other group containing all other record pairs. Fitting a line to the remaining group of points by least-squares regression assuming a zero

intercept, yields an estimate of c of 1.2 m s^{-1} with a standard error of 0.08 m s^{-1} based on the least squares fit. Using the phase errors to estimate an error yields an error in c of 0.3 m s^{-1} . The set of points using the 20 m record determines a line with a similar slope, 1.1 m s^{-1} , yet requires an intercept of -38° at zero buoyancy integral.

This estimate of c of 1.2 m s^{-1} , compares well with the estimate of c obtained by the dispersion relation for mixed Rossby-gravity waves,

$$c = \omega^2 / (\beta + \omega k).$$

Using the observed values of $2\pi/21 \text{ d}^{-1}$ equal to $3.46 \times 10^{-6} \text{ s}^{-1}$ for ω and $2\pi/1660 \text{ km}^{-1}$ equal to $3.78 \times 10^{-6} \text{ m}^{-1}$ for k , substitution into the above dispersion relation yields an estimate of 1.2 m s^{-1} . Thus, the observed vertical and horizontal phase propagation is consistent with a vertically propagating meridional mode mixed Rossby-gravity wave. A value of c of 1.2 m s^{-1} gives an equatorial length scale or internal equatorial Rossby radius of 230 km. This value of c is used to non-dimensionalize the wavenumber and frequency estimates, such that the non-dimensional wavenumber and frequency pair (s, σ) are obtained from the dimensional pair (k, ω) by scaling with the appropriate length scale ,

$$(c/\beta)^{1/2},$$

and zonal time scale,

$$(c \beta)^{-1/2},$$

where β is the meridional derivative of planetary vorticity at the equator. This non-dimensionalization yields for s , a value of -0.87 , and for σ , a value of 0.66 , which are plotted along with the corresponding error range on the equatorial dispersion curves, (figure 2.4). The estimated point lies on the curve for the mixed Rossby-gravity wave, within the range of expected error. This suggests that the propagation behavior observed for the 21 day oscillations may be described as a vertically propagating mixed Rossby-gravity wave.

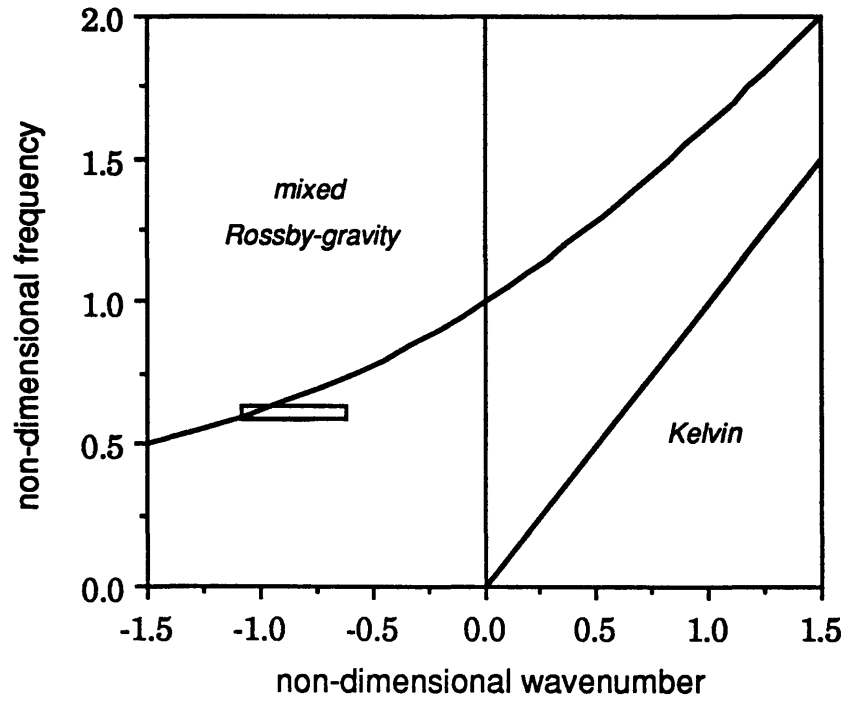


Figure 2.4: Nondimensional wave-number frequency curves for equatorial mixed Rossby-gravity and Kelvin modes. Box depicts error limits of the observed zonal wavenumber for the 20.4 day frequency band.

2.5 DISCUSSION

The results above depict a westward and upward phase propagating oscillation in meridional velocity. The zonal velocity and temperature records are more difficult to interpret, and do not seem to describe a mixed Rossby-gravity wave. They are spatially non-coherent, especially below 20 m at the equatorial and southern moorings. Locally, there is coherence between the velocity and temperature records such that statistically significant covariances are observed. This is not expected for strictly linear equatorial waves, since in general for mixed Rossby-gravity waves, u and v and v and T are out of phase. This may be due to the presence of another wave such as a first baroclinic mode, first meridional mode ($n=1$) Rossby wave which would have its largest signal in u and T on the equator because the Rossby wave is symmetric in these fields. This is backed up by the numerical model results of Cox (1982) and Semtner and Holland (1982) who showed the presence of both modes in their primitive equation models. It is also possible that the disturbance generated by the instability of the mean flow, excites the mixed Rossby gravity wave because it has a similar wavelength and period.

Since linear theory with a resting background is successful qualitatively in describing low baroclinic mode waves in the presence of a strongly varying zonal flow $U(y,z)$ in the region of the Undercurrent to the first order (McPhaden et al., 1986), it is used as a basis of comparison here. The vertical structure observed here, has the scaling appropriate to a second baroclinic mode wave, since c is observed to be 1.2 m s^{-1} . It appears however that the vertical structure is more like a vertically propagating disturbance than a mode-like one. It is the observation of upward phase propagation with depth, that indicates that the wave disturbance energy is propagating downward. The non-dimensional vertical group velocity theoretically determined from the mixed Rossby-gravity wave mode dispersion curve which the wave appears to fit is given by,

$$\frac{c_g^z}{c} = - \frac{1}{\mu s} \left\{ \frac{1 + \sigma s}{2 \frac{\sigma}{s} - 1} \right\},$$

where c_g^z is the dimensional vertical group velocity equal to $\partial\omega/\partial m$, and μ is the non-dimensional local vertical wave number equal to $N(c/\beta)^{-1/2}$.

Applying the appropriate values of the observed parameters, yields as an estimate for the vertical group velocity, -0.012 cm s^{-1} . A vertical group velocity of this magnitude is surprisingly small—allowing energy to reach the bottom of the ocean from the surface over a distance of about 5000 m, in a length of time on the order of 450 days. Weisberg et al. (1982) also observed upward propagation of phase and estimated a vertical group velocity of similar magnitude (-0.014 cm s^{-1}) for the mixed Rossby-gravity disturbance observed in the Gulf of Guinea in the eastern equatorial Atlantic Ocean. At such a speed, the time taken to set up a vertical mode is much longer than the duration of the waves which is about half of the year as observed from satellite observations. It will be shown in Chapter 4, that there is a local conversion of mean to eddy kinetic energy through shear instability.

The characteristics of vertically propagating phase and a small meridional phase difference compared to the zonal phase difference observed in the array at 110°W , suggest that the oscillations can be classified as a vertically and zonally propagating mixed Rossby-gravity wave meridional mode. But the existence of the large and highly-varying mean flow of the Undercurrent precludes the use of the resting ocean wave theory for classification. Especially if the energy source of the waves appears to be the shear of the mean flow, the mean flow should modify the wave solutions. In fact, the oscillations observed at 110°W do not compare well with many aspects of the resting ocean mixed Rossby-gravity wave. First, there are large meridional eddy fluxes of eastward momentum and heat as shown in figures 2.5 and 2.6. The large meridional divergence of these fluxes dramatically affects the mean zonal momentum and heat balance in the upper ocean as shown in Chapter 3. But, for the simple resting ocean mixed Rossby-gravity wave, the zonal velocity and the meridional velocity are in quadrature as are the temperature and meridional velocity. Thus, there should be no lateral momentum or heat fluxes. In addition, the distribution of zonal and meridional variance does not compare well with the distribution expected for the mixed Rossby-gravity wave. As reviewed in Chapter 1, the meridional velocity variance for the mixed Rossby-gravity wave has a Gaussian distribution with the maximum located on the equator. The meridional

velocity variance observed at 110°W shows a higher variance north of the equator in the upper part of the array as shown in Table 2.4. The ratio of zonal velocity variance to meridional velocity variance is observed at much higher levels than expected, since theoretically it can be written,

$$\frac{u^2}{v^2} = \sigma^2 \eta^2.$$

Thus, a node in u^2 is expected at the equator where $\eta = 0$, and at the northern and southern moorings the ratio of the variances is expected to be 0.025 using the observed values for σ and η . Instead the ratio is $O(1)$ in the array and there is significant variance in zonal velocity observed on the equator. There may be another wave present in the observations with the same zonal phase speed but with a theoretically larger zonal velocity signal. A gravest meridional mode, first baroclinic mode Rossby wave approximately overlaps the frequency-wavenumber characteristics of the wave observed at 110°W.

TABLE 2.4 AUTOSPECTRUM OF U AND V, u^2 and v^2 ($\text{cm}^2 \text{s}^{-2}$)

	N		E		S	
depth(m)	u^2	v^2	u^2	v^2	u^2	v^2
20	1092	952	535	1470	271	1615
50	670	994	213	1007	932	996
75	682	293			192	387
100	422	170	202	178	156	155
150	245	167	54	184		
200	147	204			61	202
250	108	235	60	261	19	185

Table 2.4: Autospectrum of east and north velocity components in the 36.8 to 14.2 day band.

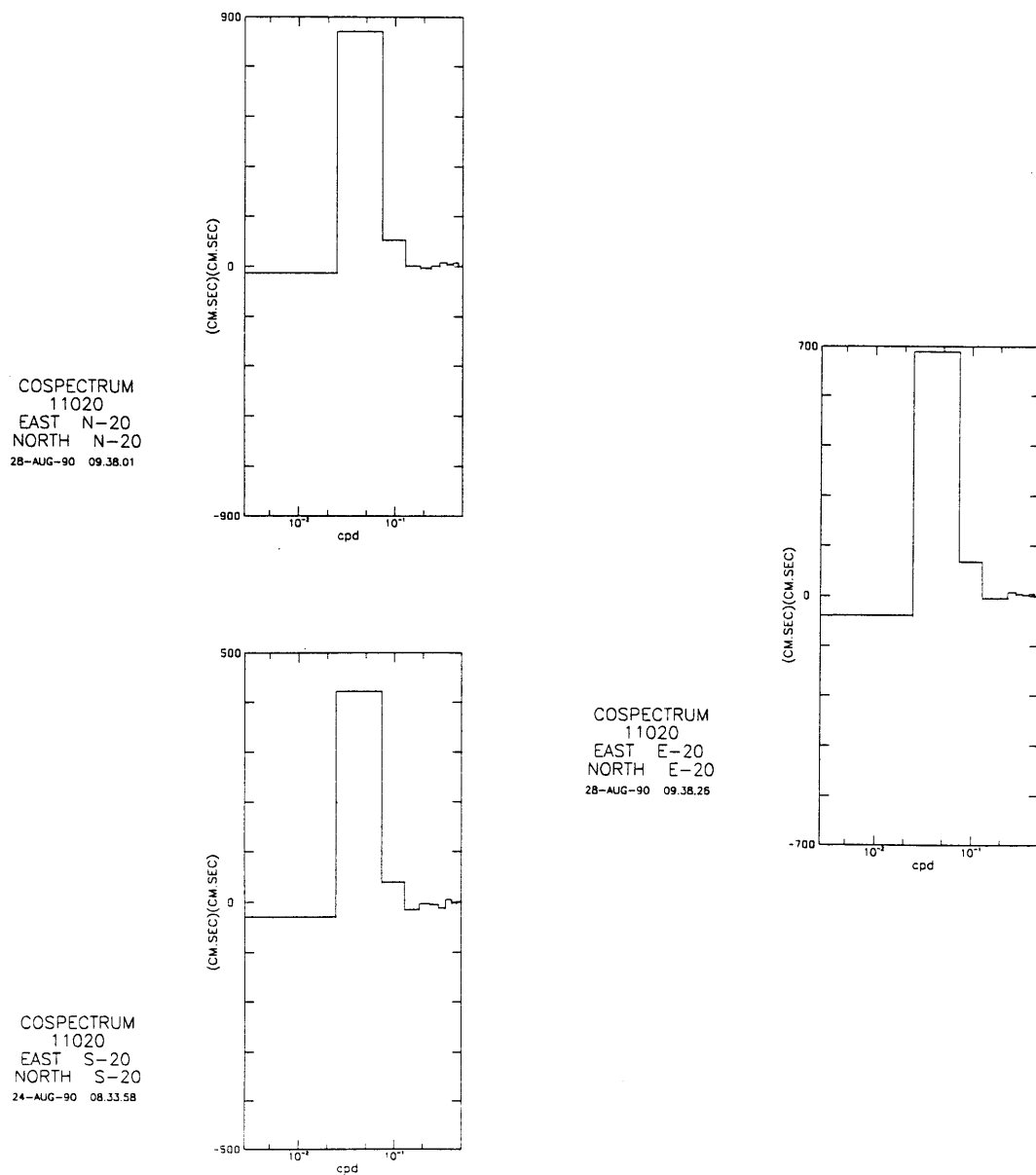


Figure 2.5: Cospectra of uv for the 184 day long timeseries at the northern, equatorial, and southern locations of the 110°W array at 20 m depth.

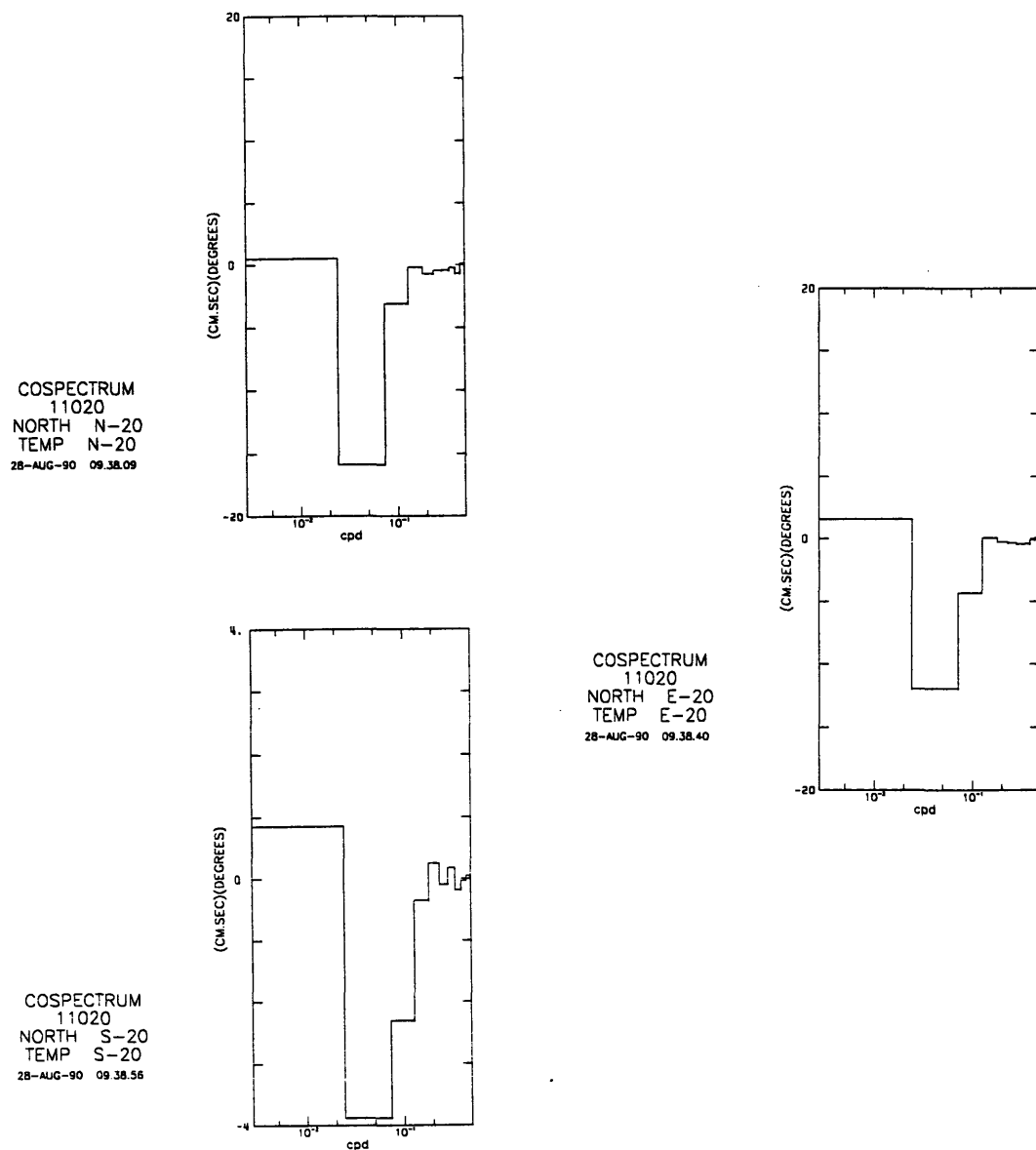


Figure 2.6: Cospectra of vT for the 184 day long timeseries at the northern, equatorial, and southern locations of the 110°W array at 20 m depth.

CHAPTER 3:

The Zonal Momentum Balance

3.1 INTRODUCTION

The main objective of this chapter is to understand the contribution to the zonal momentum balance of the slowly varying field of the Undercurrent of the tropical instability 21 day wave band (36.8 to 14.2 d). The zonal momentum equation for slowly varying zonal flow is examined by comparing the terms using the array measurements, introduced and described in Chapter 2, of mean and *eddy* quantities. The descriptor, *eddy*, is used for motions of the 21 day wave band. While the mean is taken to be the time-average over the 184-day record.

3.2 THE MEAN FLOW

The Zonal Velocity Field

The meridional and vertical distribution of the mean velocity components, U and V , and temperature T , is shown in table 3.1. The "mean" of a quantity is defined here as an average in time over the length of the time-series which is 184 days in length from August 13, 1980 to February 13, 1981. Westward flow at the 20 m depth is observed in the mean zonal velocity field, while eastward flow is found deeper. Although there is no record at the 75 m equatorial station, it would appear that the core of the Undercurrent is located somewhere south of the equator, as suggested from the generally negative meridional shear in the zonal velocity field at all depths. For the array, the maximum mean zonal velocity of 92 cm s^{-1} is located at 75 m at the southern location. Compared with the 3 year mean geostrophic zonal velocity profile at 110°W obtained by Bryden and Brady (1985) which exhibited a maximum of

98 cm s⁻¹ at 60 dbars on the equator, this maximum is somewhat deeper and off the equator, but has a similar speed. For the same current meter array location, but for all deployments and hence longer record lengths than used here, Bryden and Brady (1988) obtained a velocity maximum on the equator at the 75 m level of 106.7 cm s⁻¹.

TABLE 3.1 MEAN ZONAL VELOCITY (cm s⁻¹)

depth (m)	north	equator	south
20	-32.2	-20.1	-8.3
50	20.8	48.3	57.9
75	50.1		92.2
100	57.7	89.0	85.1
150	37.7	49.9	
200	15.7		22.5
250	-0.9	3.7	6.8

Table 3.1: Mean of zonal velocity for the triangular mooring array over the 184 day long record starting August 13, 1980.

In most profiles, as seen in figure 3.1, the Undercurrent exhibits a remarkably linear velocity profile both above and below the core. Assuming that the shear of +0.023 s⁻¹, measured here between 20 and 50 m, and -0.008 s⁻¹ between 100, 150 and 200 m, is representative of this shear, a crude estimate of the core depth and speed can be obtained by extrapolating both shear profiles toward the core and identifying the intersection as the core. The resulting extrapolated zonal velocity maximum at 76 m of 108 cm s⁻¹ compares extremely well to the maximum velocity obtained by Bryden and Brady (1989) even though a linear extrapolation tends to overestimate the core speed. Fitting a quadratic to the meridional profile of zonal velocity at 75 m using

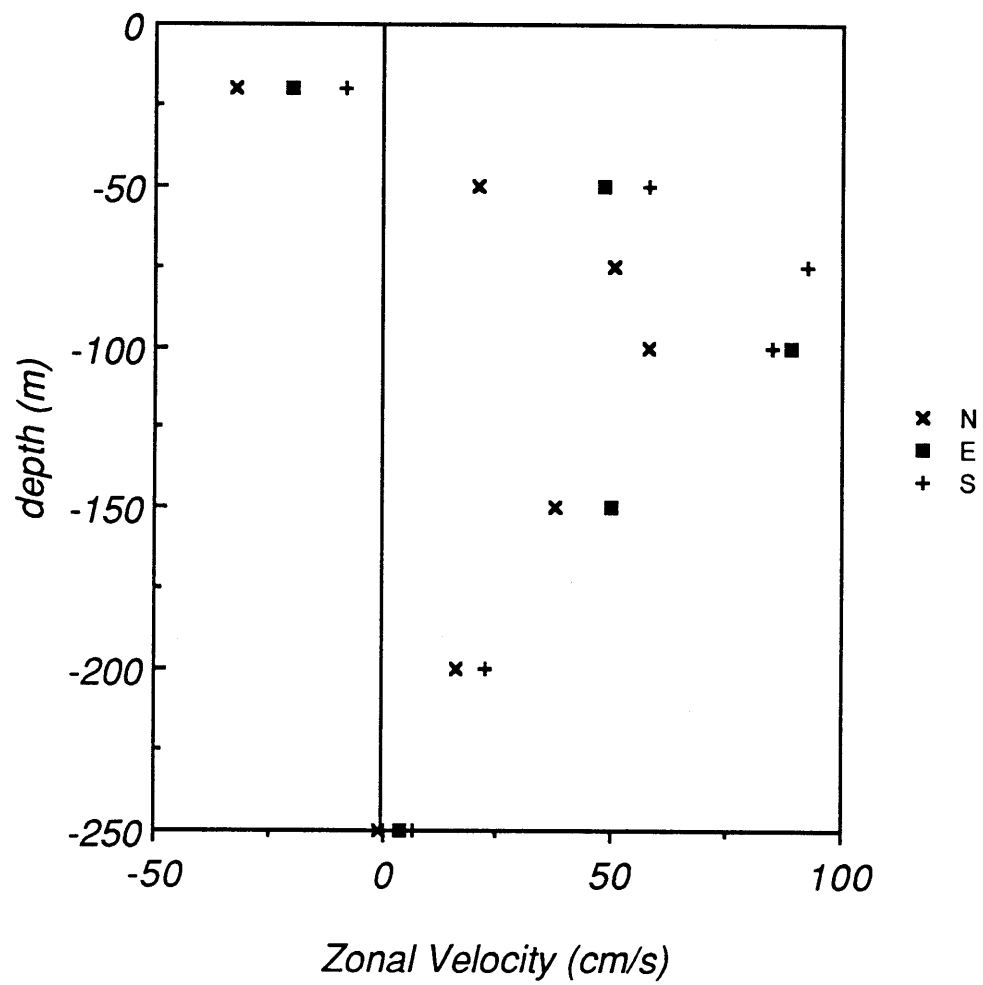


Figure 3.1: Profiles of mean zonal velocity U for the array.

the estimate determined above at the equatorial location, yields a zonal velocity maximum of 111 cm s⁻¹ located 15.3 km south of the equator.

TABLE 3.2 MEAN MERIDIONAL VELOCITY (cm s⁻¹):

depth (m)	north	equator	south
20	7.6	-1.3	-7.3
50	-3.3	-9.1	-8.3
75	-7.3		-8.7
100	-7.4	-9.6	-4.3
150	-8.5	-9.1	
200	-2.1		-5.3
250	-2.1	-3.0	-2.4

Table 3.2: Mean meridional velocity for 184 day long records at the EPOCS triangular mooring array.

The Meridional -Vertical Circulation

A mass divergence in the upper waters is observed in the mean meridional velocity field at the 20m depth level, with poleward flow measured off the equator. This distribution, which is characteristic of the equatorial surface layer, is a direct effect of poleward Ekman drift driven by the westward wind stress exceeding the equatorward geostrophic flow which balances the eastward pressure gradient force. A meridional mass divergence is observed down to the 75 m level, below which a convergence is found down to 150 m. This measured mean field is consistent with the existence of a meridional-vertical upwelling cell, superimposed on the eastward and upward flowing Undercurrent, such that geostrophic flow enters the Undercurrent laterally upstream to the west and deeper than when it leaves

the Undercurrent as upwelled water downstream to the east. If the mass divergence in the meridional velocity field were exactly balanced by a vertical convergence, a large vertical velocity of about $5 \times 10^{-3} \text{ cm s}^{-1}$ would result at 35 m depth. If this assumption holds at all deeper levels, a maximum vertical velocity of about $6.4 \times 10^{-3} \text{ cm s}^{-1}$ at 87.5 m, below the depth of the zonal velocity core. These values are twice the magnitude of the vertical velocity profile obtained by Bryden and Brady (1985). They found however, that a zonal mass convergence from the surface to the level of the core, due to the eastward and upward flowing Undercurrent, compensated for about half the meridional divergence due to the combined geostrophic and Ekman meridional velocity field at the edges of the upwelling zone. With this array, the zonal convergence cannot be reliably estimated. Thus, the vertical velocity estimated here may be a factor of two larger because of this.

In addition to the expected vertical profile of meridional mass divergence, this mean meridional velocity field contains a southward depth-independent velocity averaged over the entire array of -5.7 cm s^{-1} . This cross-equatorial flow may be a result of Undercurrent veering slightly toward the southern hemisphere at this location on average over the time period of this record. Joyce (1988) estimated that the mean wind-driven cross-equatorial component of the meridional flow near 110°W is also southward but much smaller at about -1 cm s^{-1} in the upper 200 m. A southward veering Undercurrent is also suggested by the southward displacement of the Undercurrent core as discussed above and is not inconsistent with the temperature field as discussed below.

TABLE 3.3 MEAN TEMPERATURE (°C):

depth (m)	north	equator	south
20	22.6	22.1	22.1
50	19.9	19.5	
75	17.0		17.7
100		15.2	15.4
150	13.5	13.6	
200	12.7		12.7
250	12.2	12.4	12.3

Table 3.3: Mean temperature for 184 day long records at the triangular EPOCS array.

The Temperature Field

The 184 day averaged temperature field (Table 3.3) exhibits some features of the characteristic thermal structure, although the array data greatly underresolves the sharpness of the equatorial thermocline and the thermostad of the lower thermocline. In terms of meridional distribution, colder water is observed on the equator at 100 m and above, while warmer water is observed below at the equator. No minimum is observed at 20 m. There it appears that the axis of the Cold Tongue, which is the surface manifestation of equatorial upwelling, is located somewhere south of the equator perhaps between the equatorial and southern moorings. This is not particularly unusual at 110°W, which is relatively near the coast of South American and therefore influenced by the coastal upwelling zone which extends northward along the coast of Peru and westward into the eastern equatorial basin nearly to this longitude (Lukas, 1984). The reversal in the meridional temperature gradient noted below 100m is characteristic of the

13°C thermocline, which appears as a thick layer of nearly uniform properties ($T \sim 13^\circ\text{C}$, $S \sim 34.9^\circ/\text{oo}$) beneath the Undercurrent all along the equatorial zone, with equatorward temperature gradients at the poleward edges of the thermocline, which geostrophically balance the subsurface countercurrents (Stroup, 1960; Tsuchiya 1975).

Errors in Mean Values:

There are two types of errors associated with the estimates of the record length average U , V , and T fields: the measurement errors associated with the current meter and thermistor biases, and the sampling error.

The measurement error associated with the VACM is principally due to the compass error. Since, the 360° of compass direction is digitized into 128 bins in the VACM, the error in the direction for each sample in time, $\delta\theta$, is equal to 2.8° , and is presumably random for each sample, but over time there may be a bias due to calibration offsets. Bryden (1976) showed that the bias in the compass direction is .05 radians ($= 2.8^\circ$), by comparing averages of closely spaced VACM records over 4 day intervals and the bias in the speed is very small at 0.35 cm s^{-1} . Assuming that this is representative of the magnitude of the bias over the length of the record here, then the error in U and V due to the bias in the compass direction, are :

$$\langle \delta U \rangle = \pm \langle v(\sin \delta\theta) \rangle \text{ and } \langle \delta V \rangle = \pm \langle u(\sin \delta\theta) \rangle$$

where the operators $\langle \rangle$ denote an average over the length of the record. If the directional bias is correlated with the 20 day meridional velocity oscillations, then the error in U is of the order of $\pm (30 \text{ cm s}^{-1}) (0.05)$, where $\sin \delta\theta = 0.05$, or $\delta U = \pm 1.5 \text{ cm s}^{-1}$. The error in V may be larger if the directional bias $\sin \delta\theta$, is correlated with the mean U . If so, then near the core of the Undercurrent, the error in V , is of the order of 5 cm s^{-1} ; the error decreases to less than 1.5 cm s^{-1} at the surface; and is typically 2 cm s^{-1} . Near the surface, the error is most likely due to the correlation with the 20 day oscillations of u which have a much higher amplitude there. Then the error in V is of the order of the error in U quoted above since the wave amplitude of u has a similar magnitude as for v , thus $\delta V = \pm 1.5 \text{ cm s}^{-1}$. With such error in the near surface meridional velocity, the error in the meridional divergence is $\pm \sqrt{2(1.5 \text{ cm s}^{-1})^2} = \pm 2.1 \text{ cm s}^{-1}$ over 110 km. This is much

smaller than the divergence observed, of 14.6 cm s^{-1} over 110 km at 20 m and of 5 cm s^{-1} over 110 km at 50 m. The error in the divergence is larger at deeper levels since the error becomes larger near the Undercurrent as noted above. The errors in the gradients of U due to the measurement error of U as noted above are much smaller than the gradients observed.

The measurement error for the mean temperature T due to bias in the thermistor measurement was estimated by Bryden (1976) to be 0.023°C which is much smaller than the observed differences in mean temperature across the array.

The sampling error addresses the bias in the estimated mean due to the finite length of the time series assuming ergodicity. The errors about the mean assume that the *true* mean can be calculated for an infinitely long time series, and lies within certain limits about the *estimated* mean for the finite times series to within a certain degree of confidence (or with a certain probability if the experiment were repeated, i.e. 95%). For this very short time series of only 184 days duration, this type of sampling error about the mean, equal to the square root of the variance divided by the number of degrees of freedom equal to the number of integral time scales in the record, is large because the record is only 184 days long. Near the core of the Undercurrent, the mean zonal velocity error is approximately 5 cm s^{-1} .

The estimate of the errors due to the sampling error is very large, and should be kept in mind throughout the calculations though it will be shown in the next section, that the actual error may be much smaller than this. The assumption that there is a stationary true mean to be estimated by the average over a finite length of record may not be meaningful, however, given that variability in the equatorial ocean has an enormous range of time scales from very high frequencies to interannual (ENSO) and climate scales. This is also suggested from recent ideas concerning the observations that the equatorial ocean-atmosphere system oscillates back and forth in irregular intervals between two different states, a normal state with warm water in the west and cold in the east with easterly winds, and the ENSO state with warm water in the east and westerly or weak easterly winds. Both states have positive feedback between the atmosphere and ocean which leads to the continuation of the state. It has also been suggested that there is chaos in the ocean-atmosphere feedback system that gives rise to the irregular periods and the

transitions between the two states (Vallis, 1986). Though it is more widely accepted that the transitions between the two states can be predicted from an understanding of the physics, the observations still suggest that the interval between states is irregular (Cane and Zebiak, 1985). Thus, an estimate of the *true* mean becomes ambiguous to the particular record chosen. In any event, given that one exists, it would require a very long time series to get meaningful confidence intervals about a true mean.

The object here is to choose the optimal set of records which best characterizes the wave-mean flow interaction within the Undercurrent. The records were chosen on the basis that there were few missing records so that the best horizontal and vertical resolution was obtained, and the waves appeared strong but with steady amplitudes. A consistent pattern of the interaction between the waves and the Undercurrent, as shown by the distribution of eddy fluxes, is shown in the sections which follow.

Unfortunately the set of records available at 110°W covers only a limited portion of the meridional extent of the Undercurrent. The meridional distance across the equator is only 1°latitude, approximately 110 km, while the width of the mean Undercurrent is nearly three times that distance as shown by Bryden and Brady (1985). Because the measurements are spaced too narrowly for good resolution of the Undercurrent, the calculations determined here suffer. However, these results show remarkable consistency in the spatial patterns of momentum and energy transfer as the following sections discuss. As the first attempt to quantify the interaction of the waves with the mean Undercurrent using the mooring data at 110°W, these results await confirmation by future studies using arrays designed specifically for this problem. The TROPIC HEAT Tropical Instability Wave Experiment will hopefully fulfill this need with its large-scale high-resolution array at 140°W.

Errors in Eddy Quantities

The types of errors involved in estimating the eddy fluxes used later in this chapter, are associated with the measurement error, mainly due to the bias in the VACM compass direction; the sampling error; and if the eddy quantity is inferred as is the estimate of uw , there may be error associated with assumptions about terms that cannot be estimated but may be important.

The measurement errors can be addressed assuming a directional bias of 0.05 radians, (Bryden, 1976). Writing the measured eddy fields as u_m , and v_m , then assuming the directional bias δ contributes the largest source of error and is small so that $\sin\delta \sim \delta$, u_m and v_m are estimated as,

$$u_m = u - \delta v \text{ and } v_m = v + \delta u,$$

then the error in $\langle uv \rangle$ is written,

$$\langle u'v' \rangle - \langle u_m'v_m' \rangle = \pm \langle \delta(v_m'^2 - u_m'^2) \rangle + O(\delta^2)$$

where $\langle \rangle$ denotes an average in time. Thus, the error in $\langle u'v' \rangle$ is largest where the variance in the measured velocities is the largest. Assuming that a directional bias of 0.05 radians is correlated with the variances, the error is at most equal to the size of the magnitudes multiplied by .05; this error is typically order $20 \text{ cm}^2 \text{ s}^{-2}$ but larger at the equatorial and southern moorings at about 50 and $70 \text{ cm}^2 \text{ s}^{-2}$ respectively. Thus, the measurement errors are small for the fluxes.

The sampling errors are addressed by the number of the estimates that are significantly different from zero at the 95% confidence level, shown in the tables. Because the estimate of the cospectra in the 21 day band (36.8 to 14.2 d) involves only 18 degrees of freedom, the confidence limits around the estimates are large. Still, most of the differences of the fluxes are significantly different from zero. Using as an estimate for error the confidence limits on the quadrature of uT , since it is the largest term in the estimate of uw , the errors in uw are much smaller than the estimated values of uw , and the vertical derivative of uw remains significantly different from zero at 50 m, and 100 m where the flux divergence is largest.

The motivation behind this study was to take the best set of data that resolved the Undercurrent and covered a period of time when the waves

were steady and strong, in a non-ENSO year. The frequency bandwidth for the waves was chosen to obtain enough degrees of freedom for reasonable tests of statistical confidence, while still being representative of the 21 day waves. A much longer record would be necessary to reduce the sampling errors to acceptable values but would then include time periods when the amplitude of the 21 day waves is much lower. An ideal set of data would have even better coverage of the Undercurrent; in depth there could be better coverage about the core where the gradients change so rapidly; and in latitude, the array could extend northwards into the South Equatorial Current and the theoretical region of instability and southwards a few more degrees latitude to the edge of the Undercurrent and the Upwelling zone. Such extensive measurements have not been made yet in the equatorial Pacific. Finally, the length should be long enough to sample the seasonal cycle many times and the interannual variability as well and to obtain more degrees of freedom in the band averages, and still there would be an argument over whether the ENSO years should be included in the ensemble. This study on the other hand, concentrates on the optimal three-dimensional array of existing measurements in the equatorial Pacific, which is limited in such scope, but the results are supported not only by the statistical confidence presented (though the confidence limits are wide), but also by the consistent pattern that results.

Geostrophic balance of the observed EUC

Before discussing the interaction of the waves and the Undercurrent, it is useful to determine how well the zonal mean state is in geostrophic balance with the curvature of the mean pressure field. This is done as a test to show that indeed the spatial resolution of the array is adequate for evaluating derivatives of various eddy fluxes and mean gradients. Geostrophic balance is not being tested, since that has been shown to work at the equator for many different sets of observations (Hayes, 1982; Lukas and Firing, 1984). The objective here is to assess how well meridional and vertical derivatives can be approximated as finite differences over the separation

distances in the array. To do this, the meridional derivative of the thermal wind balance will be evaluated:

$$\beta \frac{\partial U}{\partial z} = -g \alpha \frac{\partial^2 T}{\partial y^2}.$$

This would seem to be a tentative estimate given the sparse grid of U and T. Because of the sparseness of the estimates of mean temperature in the array, it is only possible to get an estimate of the geostrophic balance in the upper part of the array. To achieve the best results possible, since a vertical derivative of equatorial zonal velocity is needed, an estimate is obtained over a representative region above the core of the Undercurrent using the 20 and 50 m estimates of U and T. A value of $g\alpha$ of $0.235 \text{ cm s}^{-2} \text{ K}^{-1}$, is determined from the mean EPOCS CTD data at 110°W as used in the diagnostic model of Bryden and Brady (1985). The derivatives are estimated using centered finite differences of the first order for $\partial/\partial z$ and of the second order for $\partial^2/\partial y^2$, such that two vertically separated values are needed for $\frac{\partial U}{\partial z}$ and all three meridionally spaced values are needed for $\frac{\partial^2 T}{\partial y^2}$. It is assumed that in using the values at all three moorings in taking the second derivatives that the gradient in the zonal direction is much smaller than in the meridional direction. This is equivalent to assuming the *long wave limit*.

Above the core at an average depth of 35 m, an estimate of vertical shear of zonal velocity of -0.02 s^{-1} is obtained as the average of the vertical shear at each mooring site, while the average curvature in temperature is $1.9 \times 10^{-14} \text{ }^\circ\text{C cm}^{-2}$, obtained as an average between 20 and 50m with the southern temperature at 50 m estimated as the average between 20 and 75 m. Thus at 35 m, an estimate of βU_z of $-4.8 \times 10^{-15} \text{ cm}^{-1}\text{s}^{-2}$ is remarkably close to the estimate for $-g\alpha T_{yy}$ of $-4.4 \times 10^{-15} \text{ cm}^{-1}\text{s}^{-2}$. These estimates are closer than the sampling errors would suggest is possible, since this error in βU_z is $\pm 0.9 \times 10^{-15} \text{ cm}^{-1}\text{s}^{-2}$ and the error in $g\alpha T_{yy}$ is $\pm 4 \times 10^{-15} \text{ cm}^{-1}\text{s}^{-2}$. Below the core, the vertical shear of zonal velocity reverses, and is estimated as $.01\text{s}^{-1}$. There is some indication that the temperature curvature also reverses or at least becomes much smaller below the core; but because there are very few

temperature values below the core for taking the second derivatives, this calculation is not attempted.

The other terms in this balance which may be large enough to upset the thermal wind balance, V_{yzt} and v^2_{yyz} , are heuristically estimated and appear to be negligible. At 35 m, an estimate of V_{yz} (V_y is taken first from differences at the north and south sites at both 20 and 50 m, then the vertical difference is taken) which is the largest estimate with depth, is $3 \times 10^{-10} \text{ cm}^{-1}\text{s}^{-1}$. If this varies slowly at this amplitude, then at most, d/dt can be estimated as $2\pi/184 \text{ d}$, providing an upper bound estimate of V_{yzt} of 0.1×10^{-15} . This is more than an order of magnitude smaller than the geostrophic terms. At 20 and 50 m, estimates of $(v^2/2)_{yy}$ of -1.3×10^{-11} and $-1.2 \times 10^{-11}\text{s}^{-2}$ are obtained from the eddy 21-day band variance of the meridional velocity, giving for the vertical shear of this term, an estimate of -0.3×10^{-15} , which is also an order of magnitude smaller than the terms involved in the geostrophic balance.

Since there are large meridional shear gradients in both the mean fields of zonal velocity and temperature, which are not consistent with a model symmetric mean Undercurrent, it is of interest to examine what possible terms in the meridional thermal wind relation maintain these observed gradients. Normally, on the equator in a symmetric model, both fU_z and $-g\alpha T_y$ are by definition zero, hence the motivation for taking the second meridional derivative as was done above. Here, since f is zero and T_y large, especially above the core, the only possible terms that remain to balance this thermal gradient are $(V(V_y))_z$, $(v^2/2)_{yz}$, and $(\tau_y)_{zz}$, where τ_y is the meridional component of the wind stress. Below the velocity core the gradients are relatively small and therefore estimates are highly subject to error. Above the core, where estimates can be made at 35m and at 50m, it appears that a tentative balance between $-g\alpha T_y$ and $(v^2/2)_{yz}$ is suggested. At 35m the estimates are $-0.8 \times 10^{-8} \text{ s}^{-2}$, and $-0.6 \times 10^{-8} \text{ s}^{-2}$ respectively with meridional derivatives taken using the north and south sites, while at about 50m (47.5m for the eddy term estimate, using the values at 20 and 75 m for the vertical difference), the terms are estimated at $-0.5 \times 10^{-8} \text{ s}^{-2}$ and $-0.4 \times 10^{-8} \text{ s}^{-2}$ respectively. The mean inertial acceleration term is found to be negligibly small at 35 m as $-0.08 \times 10^{-8} \text{ s}^{-2}$ and at 50 m as $0.13 \times 10^{-8} \text{ s}^{-2}$. An equally suggestive term in this balance is the meridional wind stress divergence. As estimated here, a northward surface stress of $0.4 \text{ dynes cm}^{-2}$ distributed

exponentially with depth over an e-folding scale of 50 m (nearly twice as deep as the mean mixed layer at 110°W), would balance the observed value of $g\alpha T_y$ at 35 m of $0.8 \times 10^{-8} \text{ s}^{-2}$. This estimate compares well with an estimated annual average value of $0.3 \text{ dynes cm}^{-2}$ (W. Kessler, personal communication) at this longitude based on the FSU pseudo wind stress data. Thus it would appear that the eddy stress term may be at least as important in maintaining the meridional gradient of temperature as the northward wind stress.

Summary and Discussion

This section has presented the record mean U, V, and T fields in preparation for the following sections of this chapter, which require that meaningful estimates of the meridional and vertical derivatives of these fields can be established with the available array measurements. Although the array does not resolve well all of the details of the equatorial Undercurrent-upwelling system, enough gross features can be diagnostically evaluated, that confidence in the results presented in the next sections is warranted.

It is found that the observed vertical shear of the zonal velocity field is grossly in balance with the meridional curvature of the observed temperature field as expected from the thermal wind relation in the upper part of the array. The observed features of the equatorial Undercurrent and thermocline are not symmetric in this array. It is interesting to find that since fU_z can not balance $-g\alpha T_y$ (through the thermal wind relation since f is zero), the vertical shear of the eddy Reynold's stress divergence may be large enough to enter the balance at the same order as the effect of the northward wind stress divergence, which is the term suggested to balance $-g\alpha T_y$ by Joyce (1988).

3.3 MEAN ZONAL MOMENTUM BALANCE

Given the three-dimensional distribution of mean and eddy quantities measured by the array, many terms in the mean zonal momentum equation, written below, can be estimated. A residual acceleration tendency of the large scale slow zonal flow U , due to the combined effect of these terms, can be inferred through the mean zonal momentum equation:

$$U_t = -P_x + \tau_z^* + (f-U_y)V^* - UU_x^+ - WU_z^+ - (uv)_y^* - (uw)_z^+.$$

$$ZA = ZPG - TSD + CA - IA - RSD.$$

This equation describes how the large scale slowly varying zonal flow is accelerated (ZA) by the imbalance in the zonal pressure gradient force (ZPG) and vertical stress divergence due to wind-generated turbulence (TSD), by the Coriolis (CA) and inertial acceleration (IA) terms, and by the horizontal and vertical Reynolds stress divergence (RSD). Only the terms indicated with the asterisks can be estimated directly with the array measurements. Some of the remaining terms, those indicated with a cross, can be indirectly estimated from measured quantities. These terms require indirect estimation techniques which assume certain balances in both the eddy and mean heat equations. The terms that can not be estimated with this data set are the zonal pressure gradient (ZPG) and the turbulent vertical stress divergence (TSD) terms. Dillon et al. (1989) discuss the imbalance between the turbulent stress divergence and the zonal pressure gradient for the region above the Undercurrent core.

The results of the zonal momentum balance analysis will be presented in the order of the eddy Reynolds stress divergence terms, followed by the mean advection of mean zonal momentum.

EDDY REYNOLDS STRESS DIVERGENCE

Horizontal Stress Divergence

The directly observable meridional divergence of the northward flux of eastward momentum accomplished by the eddy field, uv , is the term generally reported in the literature. As table 3.4 shows, throughout the upper part of the array, at each latitude at and above the zonal velocity maximum observed at 75 m, the cospectrum of uv is positive and highly coherent particularly at the equatorial and northern mooring sites, implying a northward flux of eddy eastward momentum. In the depth range of interest here, 20 to 100 m, the meridional divergence of uv is positive, indicating a net depletion of eastward momentum at the equator. Hence, the net depth-integrated effect of this term in the zonal momentum balance acts as an equivalent westward stress. Integrating vertically over this depth range, using a simple trapezoidal scheme of integration, where the depth intervals associated with the estimates at 20, 50, 75, and 100 m are 35, 27.5, 25, and 12.5 m respectively, gives an effective westward stress of $-0.31 \text{ dynes cm}^{-2}$. This estimate is comparatively large with respect to the typical annual average wind stress of about $-0.5 \text{ dynes cm}^{-2}$ at this longitude, and is slightly larger than the amplitude of annual cycle of wind stress (Meyers, 1979). The effective stress is largest over the upper 35 m at $0.14 \text{ dynes cm}^{-2}$, decreasing monotonically to near zero ($-0.03 \text{ dynes cm}^{-2}$) at 100 m. The calculation is not carried out deeper in the water column for the reason that at levels below 100 m, either the estimate is non-significant as at 200 m at the southern location or missing entirely as is the case at 150 m. An exception occurs at 250 m where the Reynolds stress divergence yields an eastward and significant though negligible estimate for this equivalent stress of $0.01 \text{ dynes cm}^{-2}$. In fact, at the deeper levels, there is a general indication that there is a reversal in sign of the Reynolds stress, uv at the northern mooring, suggesting a reversal in sign of the divergence of uv , as occurs at 250 m. Though too small to compensate the depth-integrated effect of the large westward effective stress imparted by the eddies in the upper levels, there is a tendency for a reduction of the overall effect in the deeper levels. This reversal at depth is better observed using longer records and a wider frequency band (Bryden and Brady, 1989).

TABLE 3.4 COSPECTRUM OF U AND V, uv ($\text{cm}^2 \text{s}^{-2}$)

	N		E		S	
depth(m)	uv	Coh	uv	coh	uv	coh
20	<u>846</u>	.93	<u>684</u>	.91	<u>422</u>	.76
50	<u>601</u>	.85	<u>369</u>	.85	<u>160</u>	.59
75	<u>186</u>	.76			-29	.24
100	<u>-10</u>	.83	<u>-94</u>	.84	<u>-41</u>	.60
150	<u>-49</u>	.83	-14	.14		
200	<u>-14</u>	.71			16	.34
250	<u>-24</u>	.79	43	.54	<u>35</u>	.72

Table 3.4: Cospectrum and coherence of east and north velocity components in the 36.8 to 14.2 day band. Values that are significantly different from zero at the 95% confidence level are underlined.

Vertical Stress Divergence:

The vertical Reynolds stress divergence term must be indirectly estimated by making use of a presumed eddy temperature balance:

$$-i(\omega - U k)T + uT_x + vT_y + wT_z = -q_z.$$

Multiplying by u , isolating the real part and solving for the cospectrum of uw gives:

$$uw = -(\omega - U k)\frac{Q(uT)}{T_z} - u^2\frac{T_x}{T_z} - uv\frac{T_y}{T_z} - \frac{uq_z}{T_z},$$

where $Q(uT)$ is the quadrature component of the zonal eddy heat flux. The first and third terms on the right hand side are directly estimated from the array. The second term can be estimated as well, if a reasonable estimation of the zonal isotherm slope T_x/T_z is used. The last term can not be estimated but is small provided that this phenomena is not driven by atmospheric heating.

TABLE 3.5 QUADSPECTRUM OF U AND T, $Q(uT)$

	N		E		S	
depth(m)	$Q(uT)$	Coh	$Q(uT)$	coh	$Q(uT)$	coh
20	<u>2.0</u>	.82	<u>0.6</u>	.71		
50	<u>-17.6</u>	.67	-7.8	.53		
75	<u>-24.4</u>	.72			1.4	.24
100			<u>-1.8</u>	.93	-0.8	.23
150	<u>-1.7</u>	.82	.06	.56		
200	<u>-.55</u>	.81			<u>-.32</u>	.73
250	<u>-.55</u>	.79	.04	.52	.02	.41

Table 3.5: Quadrature spectrum and coherence of u and T for the 36.8 to 14.2 day band. Estimates of the quadrature spectrum that are significantly different from zero at the 95% confidence level are underlined.

Table 3.6 lists the individual terms used to estimate uw . Estimates of the terms involving wave fluxes, in the 36.8 to 14.2 day band, that are significant at the 95% confidence level are shown with an asterisk. The estimate of $Q(uT)$ at the equatorial location, is used in the calculation of the first term in the table, except at 75 m where no estimate exists. Instead at 75 m, an average between the north and south estimates is used. The equatorial

estimate of $Q(uT)$ at 50 m, with a coherence of 0.53, would be significantly different from zero at the 93% confidence level. Because the 50 m equatorial value of $Q(uT)$ is about the mean of the north and south value, taking the mean north and south value at 75 m is reasonably justifiable for this estimate. The term $Q(uT)$ is then multiplied by the intrinsic frequency, $\omega - Uk$ with k as determined in Chapter 2, and with U as estimated at the equator. The next term, u^2T_x/T_z , is derived from the equatorial estimate of the autospectrum of u in the 36.8 to 14.2 day band multiplied by T_x/T_z , which is taken to be -1.8×10^{-5} from Bryden and Brady (1985) as determined from mean CTD sections for the same region. Overall this term appears to be negligible. The last term is derived from the cospectrum of uv multiplied by T_y/T_z as determined by finite differences within the array. Except at 20 m, where both the cospectrum of uv and T_y are large, this term is negligible also. Again at 75 m, averages of the north and south values were used in the estimation of these two terms.

To obtain an estimate of the vertical divergence of uw , at the same nominal levels in order to compare with the meridional divergence terms, the uw estimates are linearly interpolated to the mean depths between levels and then first order finite differences are taken. These are shown in figure 3.3 along with the meridional Reynolds stress divergence estimates for comparison.

The estimate for uw may be highly sensitive because potentially it may be a small residual among the many large terms possible in the balance—terms which themselves may be subject to large uncertainty. Fortunately however, except at 20 m and 100 m, the term involving $Q(uT)$ is much larger than the other two terms suggesting a dominant balance between the $Q(uT)$ term and uw . This balance implies that the zonal velocity is in phase with the vertical velocity due to the local displacement of the isotherms. This is expected for linear waves where the dT/dt and wT_z terms are in balance. At 20 m, the term proportional to uv , is much larger than the other two terms suggesting that a balance is struck between it and uw . This is the case if wT_z and vT_y are balanced in the wave temperature equation and the zonal momentum flux is therefore along constant temperature surfaces. At 100 m, all three terms are equal in relative importance but small and of the same sign, such that uw is not a residual in the balance. At the levels below 100 m,

the estimates for all terms are very small. Estimates of terms that yielded values smaller than .002 are not entered in the table.

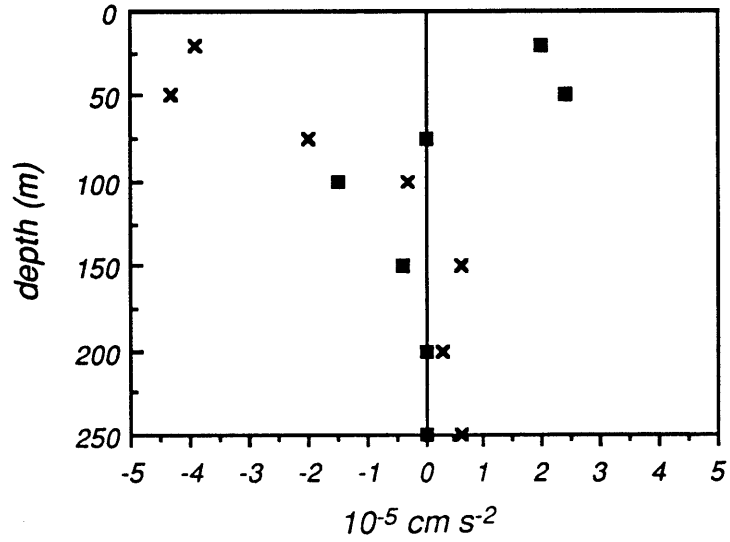
TABLE 3.6 VERTICAL EDDY REYNOLDS STRESS, uw (dynes cm⁻²)

depth (m)	$-\omega_o Q(uT)/T_z$	$-u^2 T_x / T_z$	$-uvT_y / T_z$	uw
20	-.003*	.01	-.03*	-.02
50	.044	.004	-.007*	.04
75	.10*	.004	.01*	.11
100	.024*	.01	.01*	.04
150	-.002	.001	-.002	-.003
200	0	.002	0	.002
250	-.001	.001	.004	.004

Table 3.6: Estimates of vertical Reynolds stress using the quadrature of the zonal velocity and temperature in the 36.8 to 14.2 day band. Estimates using statistically significant wave fluxes at the 95% confidence level are denoted with asterisks. The frequency ω_o , is the intrinsic frequency, equal to $\omega - U k$, where k is the zonal wavenumber determined in Chapter 2 and U is the mean zonal velocity at the equator.

The vertical eddy Reynolds stress uw (Table 3.6), is everywhere positive in the region of the core implying an upwards transport of eastward momentum. The vertical distribution of uw , with the maximum found at the depth of the core of the Undercurrent, suggests a possible relationship with the profile of zonal velocity, figure 3.1. Above the velocity maximum, where the shear is negative and constant, the vertical divergence of uw is also negative and nearly constant at $-2.0 \times 10^{-5} \text{ cm s}^{-2}$ at 20 m and $-2.4 \times 10^{-5} \text{ cm s}^{-2}$ at 50 m, indicating a net convergence of eastward momentum. Below the core,

A



B

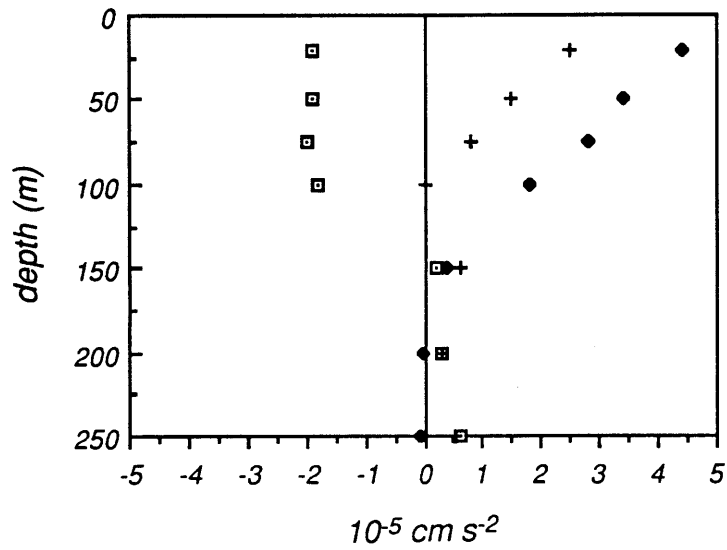


Figure 3.2: A: Vertical profiles of eddy stress divergence terms: $-(uw)_z$ (solid boxes) and $-(uv)_y$ (x's). B: Profiles with depth of the sum of the eddy Reynolds stress divergence (boxes) compared to the eastward pressure gradient force (diamonds) derived from dynamic height differences from 110°W to 150°W, and their sum (+).

where the shear is positive, the stress divergence is also positive, at 1.5×10^{-5} cm s^{-2} at 100 m indicating a net divergence of eastward momentum. Thus, over the depth range of the core at 75 m, no net divergence of vertical Reynolds stress is obtained by differencing the values at 50 and 100 m. This relationship to the zonal velocity profile suggests a means by which the effect of the vertical eddy Reynolds stress divergence may be parameterized through an entrainment velocity-like parameterization rather than the usual eddy viscosity coefficient. This will be discussed in more detail later. Nonetheless a structure that appears as an equivalent eastward stress divergence above the velocity core and an equally strong westward stress divergence below the core, acting alone over a length of time, would drive the velocity core to shoal without an acceleration of the eastward current in an integrated sense, because the net divergence from 50 to 100 m is negligible. An overall, depth-integral of stress divergence, equal to an eastward equivalent stress of $0.08 \text{ dynes cm}^{-2}$ is obtained for the vertical Reynolds stress divergence, (Table 3.7). This serves only to partially compensate for the large westward equivalent stress due to the meridional divergence of uv , reducing the net effect over the upper 100 m to $-0.22 \text{ dynes cm}^{-2}$.

TABLE 3.7 REYNOLDS STRESS DIVERGENCE:

depth (m)	$-(uv)_y$	$-(uw)_z$	Sum (dynes cm ⁻²)
20	-.14	.07	-.07
50	-.11	.07	-.04
75	-.05	0	-.05
100	-.01	-.05	-.06

Table 3.7: Estimates of eddy Reynolds stress divergence from the cospectrum in the 36.8 to 14.2 day eddy band containing the tropical instability waves as measured in the EPOCS array at 110°W. Values listed in the table are multiplied the depth difference over which an integral would be taken.

Discussion

Turbulence measurements on the equator have shown that turbulent dissipation and hence downward turbulent stress divergence is too small at the levels of the core to balance the eastward pressure gradient force (Dillon et al., 1989). Thus, it may be possible to balance the residual pressure gradient with the eddy stress divergences, $-(uv)_y - (uw)_z$. In a bulk sense a zonal momentum budget can be attempted for the core region using for the pressure gradient, the estimated dynamic height difference between 110°W and 150°W from Bryden and Brady (1985). This assumes that the pressure gradient at 130°W is applicable to a comparison at 110°W. Figure 3.3 shows the profiles of pressure gradient force, $-P_x$ with the profile of the sum of the Reynolds stress divergence terms. The pressure gradient force is eastward over the range examined here and decreases from the surface to negligible values by 150 m. The sum of the Reynolds stress divergence terms at about $-2.0 \times 10^{-5} \text{ cm s}^{-2}$ is nearly constant in the upper part of the array down to 100 m, and rapidly decreases to small values below. Remarkably, near the core, in the region from 75 m and below, the Reynolds stress divergence terms appear to balance the pressure gradient force. Above the core, the pressure gradient is much larger and is only partially balanced by the Reynolds stress divergence. Referring back to figure 3.2, it is observed that the

term mainly responsible for balancing the pressure gradient in the region below the core is $-(uw)_z$. Whereas at the core and above, $-(uv)_y$ is primarily responsible for balancing the pressure gradient force which is eastward. The resulting profile of the sum of the pressure gradient force and the Reynolds stress divergence terms decreases linearly from 20 m to 75 m and is negligible below. This profile must be balanced by the turbulent stress divergence which as mentioned before drops to negligible values at the core. Integrated to 125 m as before, the pressure gradient force integrates to $.38 \text{ cm}^2 \text{ s}^{-2}$, and the Reynolds stress terms integrate to $-.23 \text{ cm}^2 \text{ s}^{-2}$, yielding a residual of $0.15 \text{ cm}^2 \text{ s}^{-2}$. The breakdown into regions above and below the core is shown below in table 3.8.

TABLE 3.8 INTEGRATED ZONAL MOMENTUM BALANCE

	$-P_x dz$	$-(uw)_z dz$	$-(uv)_y dz$	$\approx -d\tau$
0 to 75 m	.28	.17	-.27	.18
75 m to 125 m	.10	-.09	-.03	-.02
0 to 125 m	.38	.08	-.30	.16

Table 3.8: A breakdown of the terms in the integrated zonal momentum balance for three regions of the Undercurrent core, 0 to 75 m, above the core, 75 to 125 m, below the core and over the entire depth range, 0 to 125 m.

Table 3.8 illustrates the bulk effect of the stress divergence terms in relationship to the core of the Undercurrent. It appears that above the core in the region 0 to 75 m, the vertical Reynolds stress divergence nearly cancels the decelerative effect of the meridional Reynolds stress divergence leaving a large eastward pressure gradient force that must be balanced by the wind-generated turbulent stress divergence. Below the core, the vertical Reynolds stress divergence is decelerative and provides a means by which to balance

the eastward pressure gradient force at those depths since there the meridional Reynolds stress divergence and turbulent stress divergence are small.

INERTIAL ACCELERATION

An Estimate for WU_z

For the mean vertical advection of eastward momentum, WU_z , an estimate of the mean vertical velocity is necessary. It has been shown by Brady and Bryden (1987) that at the depth of the velocity core at the lateral axis of the Undercurrent, shown in the previous section to be near 75 m, vertical velocity can be reasonably approximated using the following balance in the mean temperature equation:

$$W = -U (T_x/T_z).$$

This balance asserts that fluid flows upward and eastward nearly along isotherms at the core of the Undercurrent (Bryden and Brady, 1985). An upward "cross-isotherm flux" is necessary to balance the downward diffusion of heat from positive net air-sea heat exchange at the surface but is assumed to be small at the depth of the velocity core. Above the core, at the depth of the mixed layer the cross-isotherm flux is comparable to the vertical mass flux W . The Undercurrent system as observed here, is not symmetric at the equator. Not only is the cross-equatorial mass flux V not exactly zero, but the lateral velocity maximum appears to be located south of the equator, as is the axis of the Cold Tongue, suggested by the southward meridional temperature gradient evident at 20 m. Thus, the terms in the temperature equation that are otherwise neglected,

$$- V (T_y/T_z) - (vT)_y/T_z,$$

may be large enough to disrupt the balance asserted above at the level of the core. Also these terms may be considerably important above the core, as may be the mean diabatic heat divergence which is not estimated here. Hence, from 20 to 100 m, W is estimated here as a residual of the following terms derived from the mean temperature balance:

$$W = -U(T_x/T_z) - V(T_y/T_z) - (vT)_y/T_z.$$

Estimates of each term as a function of depth are given in Table 3.9.

The estimate of WU_z depends on the estimates of the mean vertical velocity W , are shown in Table 3.9. The two largest terms in the equation for W are $-(vT)_y/T_z$ and $-U T_x/T_z$, and are both positive, such that W is not a small residual of two large terms. At 50 m all three terms are nearly the same magnitude. The resulting profile of W , even without adjusting the estimate at 20 m by adding an upward velocity to balance the mean diabatic heating term q_z/T_z , compares well to the mean profile obtained by Bryden and Brady (1985), listed in column 6 of Table 3.9 for comparison.

TABLE 3.9 MEAN VERTICAL VELOCITY: ($\times 10^{-3} \text{ cm s}^{-1}$)

depth (m)	$-U(E) \frac{T_x}{T_z}$	$-V_{ave} \frac{T_y}{T_z}$	$\frac{-(vT)_y}{T_z}$	W	W^*	W_c^{**}
20	-0.4	0.031	1.3	1.0	1.0	---
50	0.9	0.6	0.8	2.3	2.5	1.0
75	1.2 (2.0)	-0.6	1.2	1.8 (2.6)	2.6	0.7
100	1.6	-0.5	0.8	1.9	2.0	0.1

Table 3.9: Mean vertical velocity as indirectly estimated by the sum of the terms listed in the table. The mean vertical velocity, denoted with an asterisk and mean cross-isotherm vertical velocity, denoted with a double asterisk, from the three-dimensional diagnostic model of Bryden and Brady (1985), are listed for comparison.

The cross-isotherm component is defined as the portion of W that is not due to the term $-U T_x/T_z$. At 75 m and 100m, this cross-isotherm

velocity is only about 20 percent of W . Thus, the approximate streamline slope, W/U , is only about 20 percent larger than the zonal isotherm slope (note that the presence of V skews the actual stream line with respect to the equator).

Overall, this array yields a reasonable estimate for the vertical velocity field. At least, the estimates for W obtained for this data set agree with an established long-term average profile for the same location (Bryden and Brady, 1985).

The inertial acceleration term $-WU_z$ is estimated by multiplying the estimate of W from table 3.9 by the vertical shear in the zonal velocity at the equator, estimated by centered finite differences and linearly interpolated the appropriate depth as listed in table 3.10. The resulting profile shows a tendency for eastward acceleration above the core and deceleration below which is due to the change in sign of the vertical shear at the core of the Undercurrent.

TABLE 3.10 ESTIMATION OF WU_z

depth (m)	W ($10^{-3} \text{ cm s}^{-1}$)	U_z (s^{-1})	WU_z ($10^{-5} \text{ cm s}^{-2}$)	$-WU_z dz$ ($\text{cm}^2 \text{ s}^{-2}$)
20	1.0	-.023	-2.3	.08
50	2.3	-.023	-5.3	.14
75	2.6	0	0	0
100	1.9	.008	1.5	-.06

Table 3.10: Estimates of the inertial acceleration term WU_z . The values for W are taken from Table 3.9. Values of U_z are derived from finite differences of the zonal velocities in Table 3.1.

An Estimate for $U U_x$

The remaining mean advection term to be indirectly estimated, $-UU_x$, can be inferred by requiring three-dimensional mass conservation, such that

$$-U U_x = U (V_y + W_z),$$

given that W_z is reliably determined.

TABLE 3.11 MASS DIVERGENCE:

depth (m)	W ($\times 10^{-3} \text{ cm s}^{-1}$)	W_z	V_y ($\times 10^{-7} \text{ s}^{-1}$)	$-U_x$	$-U(E)U_x$ ($10^{-5} \text{ cm s}^{-2}$)
20	1.0	-4.7	13.8	9.1	-1.9
50	2.3	-2.9	4.7	1.8	0.9
75	2.6	0.8	1.3	2.1	1.4 (2.3)
100	1.9	2.4	-2.9	-1.0	-0.8

Table 3.11: Estimate of the inertial acceleration term $U U_x$. Estimates of the vertical velocity W , mean vertical, meridional and zonal divergences, W_z , V_y , and U_x , for the EPOCS array. For the estimate of UU_x , the mean zonal velocity on the equator is used where available at 20, 50 and 100 m. At 75 m, two estimates result from using either the vertical average, 89 cm s^{-1} , or the vertically extrapolated value, 108 cm s^{-1} , at 75 m. The estimate derived from the extrapolated velocity is shown in parentheses.

Under the assumption that a reasonable estimate is made for the profile of W , the UU_x term is estimated in a straightforward way (Table 3.11). To obtain W_z , first the values for W are first linearly interpolated to the intermediate levels, 35, 62.5, 87.5, and 125 m. Then, with a surface value of

zero, vertical differences are taken. To obtain V_y , differences between the Northern and Southern values are used. Thus U_x is estimated as the negative of the sum of these two terms by the divergence equation. For UU_x , the equatorial zonal velocity U , measured in the array is multiplied by the estimate of U_x . At 75 m, two estimates for this term are presented using two different values of U at the equator since no value is measured there. The first estimate uses the vertical average between the 50 m and 100 m values at the equator, and the second estimate, in parentheses, uses the extrapolated value, 108 cm s^{-1} as explained earlier in the chapter. It is hoped that these two estimates bound the estimate if the actual zonal velocity had been measured at 75 m depth, since these two estimates for U probably under- and over-estimate the zonal velocity at 75 m. The resulting profile shows eastward acceleration at the level of the core and deceleration both above and below.

Comparison of the estimate made with this data set, of the term UU_x with the estimate of Bryden and Brady (1985) at the same depths shows that these terms may be grossly overestimated due to the large error associated with the estimate of the vertical velocity and the measurement and sampling errors associated with the meridional velocity field. These errors will be discussed later.

TABLE 3.12 COMPARISON OF INERTIAL ACCELERATION ESTIMATES

depth (m)	- $U(E)U_x$ ($10^{-5} \text{ cm s}^{-2}$)	- UU_x (Bryden, Brady, 1985)	- WU_z ($10^{-5} \text{ cm s}^{-2}$)	- WU_z (Bryden, Brady, 1985)
20	-1.9	-0.4	2.3	2.0
50	0.9	-0.4	5.3	2.2
75	1.4(2.3)	0.4	0	0.3
100	-0.8	1.2	-1.5	-0.9

Table 3.12: A comparison between the inertial acceleration terms estimated from the time-averaged velocity field measured from the array, and the estimates from the three-dimensional diagnostic geostrophic model of Bryden and Brady (1985).

An Estimate for VU_y

The term, $-VU_y$, is the only directly estimated inertial acceleration term. This term is estimated by multiplying the mean northward velocity V by the meridional derivative of U as estimated by the difference of the measurements of U between the north and south mooring sites. The estimate for V is determined in two ways: first from the equatorial mean meridional velocity and from the average V from over the array, obtained by weighting V at the north and south moorings half the weight of V measured at the equatorial mooring. As shown in Table 3.13 both these estimates give similar results. The acceleration term $-VU_y$ is everywhere negative over the upper 100 m, due to both a southward meridional velocity field and negative meridional shear of U . This term is integrated over the upper 125 m, using the estimates at the 20, 50, 75, and 100m location as representative of the regions between 0-35, 35-62.5, 62.5-87.5 and 87.5-125 m respectively, where 125 m is the average depth between the 100 m instrument and the next instrument at 150 m. This integral amounts to an equivalent westward stress acting on this region of $-0.26 \text{ dynes cm}^{-2}$, using $V(E)$, or -0.23 using V_{ave} . This effective stress is rather large considering that this term would be zero if the array were measuring a mean symmetric Undercurrent. Note that if not for the presence of the depth averaged southward flow of -5.7 cm s^{-1} discussed in an earlier section, this term would be much smaller.

TABLE 3.13 ESTIMATION OF VU_y

depth (m)	dz (m)	U_y (10^{-6}s^{-1})	$V(E)$ (cm s^{-1})	V_{ave} (cm s^{-1})	VU_y (10^{-5}cm s^{-2})	$VU_y dz$ dynes cm^{-2}
20	35	-2.2	-1.3	-0.6	0.3 (0.2)	.01 (.006)
50	27.5	-3.4	-9.1	-7.4	3.1 (2.5)	.08 (.07)
75	25	-3.9		-8.0	3.1	.08
100	37.5	-2.6	-9.6	-7.7	2.5 (2.0)	.09 (.07)

Table 3.13 Estimates of the term VU_y . For comparison, both the estimates for V using the equatorial velocity, $V(E)$, and the average across the array at a given depth, V_{ave} , are presented. For the estimates of VU_y and $VU_y dz$, the values within parentheses are estimated with V_{ave} while the values without parentheses use $V(E)$.

The Combined Interpretation

As observed in Table 3.14, the combined effect of the inertial acceleration is to accelerate the Undercurrent above the core and decelerate below the core. The term, $-VU_y$, is a decelerative effect over the entire region of the core due to the large net southward flow observed. Integrated to 125 m, a westward equivalent stress of $-.23 \text{ dynes cm}^{-2}$ is obtained. The term $-WU_z$, accelerates above the core and decelerates below the core such that the net effect over the region from 0 to 125 m, is a net eastward equivalent stress on the core of about $0.16 \text{ dynes cm}^{-2}$. The term $-UU_x$, is negative both above and below the core, at 20 and 100 m but is positive in the core region at 50 and 75 m. Overall this terms contributes little to the net effect, since an integral from 0 to 125 m yields only $-.02 \text{ dynes cm}^{-2}$. Thus it is suggested by these estimates that the two terms $-VU_y$ and $-WU_z$, nearly cancel to yield a very small combined effect. This implies that the net effect of the inertial acceleration terms on the Undercurrent is to redistribute momentum within

the core region without any net acceleration of the entire flow. The distribution of the combined terms with depth indicates that the effect is to accelerate above the core and decelerate below thereby causing the core to shoal with only a small net deceleration overall. These advective effects by the mean flow, which lead to a shoaling of the Undercurrent core, should not be surprising since the Undercurrent does rise to the east as it crosses the Pacific.

TABLE 3.14 INERTIAL ACCELERATION

Depth (m)	- $V U_y dz$	- $W U_z dz$	- $U U_x dz$	TOTAL
	(dynes cm ⁻²)			
20	-.006	.08	-.07	.004
50	-.07	.14	.02	.09
75	-.08	.00	.04 (.06)	-.04 (-.02)
100	-.07	-.06	-.03	-.16

Table 3.14: Estimates of the inertial acceleration terms, multiplied by the appropriate depth over which trapezoidal integration is performed. The units, dynes cm⁻², are units of effective stress.

DISCUSSION

The vertical profile of uw (figure 3.2), estimated indirectly using the wave temperature equation, corresponds in shape to the profile of $U(z)$, (figure 3.1), with a maximum at the depth of the Undercurrent core and linear shear both above and below the velocity core. The horizontal Reynolds stress divergence term decreases in magnitude downward remaining consistently negative down to 100 m. In fact, all of the estimates which significantly contribute to the net overall deceleration determined here, seem reasonably determined with respect to the vertical distribution displayed. Thus, it is of interest to examine the balance of the combined terms as a function of depth, in order to focus specifically on the effects on the Undercurrent core itself.

The combined effects are presented in Table 3.15 adjacent to the corresponding depth range for each term. The mean inertial acceleration terms are displayed separately from the eddy Reynolds stress divergence effects. Integrated in depth, the total effect of the inertial acceleration is small at -0.09 dynes cm^{-2} . The depth-integrated effect of the Reynolds stress divergence is large at -0.21 dynes cm^{-2} acting as an overall equivalent westward stress. As mentioned before, together an overall westward stress of -0.3 dynes cm^{-2} is obtained.

In examining the two effects as a function of depth, a noteworthy picture for the Undercurrent core is revealed. The profile of the sum of the inertial acceleration terms exhibits an eastward stress of about 0.1 dynes cm^{-2} at a level of 50 m, due mainly to the effect of mean vertical advection, with a nearly compensating westward stress observed below this level. Since the depth-integrated effect of the inertial acceleration is small, this term serves merely to redistribute zonal momentum in the vertical, without acting to decelerate the depth averaged zonal momentum.

TABLE 3.15 OVERALL MOMENTUM BALANCE

Depth (m)	IA	RSD (dynes cm ⁻²)	IA + RSD
20	.004	-.07	-.07
50	.09	-.04	.05
75	-.04 (-.02)	-.05	-.09 (-.07)
100	-.16	-.05	-.21

Table 3.15 Final estimates of the inertial acceleration and the Reynolds stress divergence terms are presented to examine the overall contribution to the zonal momentum balance.

The profile of the total Reynolds stress divergence shows generally westward stress at all levels with a slight minimum found at 50 m. Such a stress profile, accelerates the flow at the surface, where the zonal velocity is westward, while decelerating the flow in the region around the core. Together with the inertial acceleration, the combined stress profile exhibits a large westward stress both above and below the 35 to 62.5 m depth interval, where an eastward stress is shown. If allowed to act continuously over time or in the downstream direction, such a vertical stress profile would cause the velocity maximum to ascend or shoal. Furthermore, the profile would sharpen, becoming more westward at the surface, more eastward above the depth of the core observed here, and less eastward at and below this depth.

3.4 THE ELIASSEN – PALM FLUX DIVERGENCE

Traditionally in meteorological studies of the interaction of zonal mean flows with wave disturbances, it has been useful to formulate the temporal evolution of the mean flow due to the presence of the waves in terms of the divergence of the Eliassen - Palm (EP) flux (Eliassen and Palm, 1961). Within such a context it can be shown that under certain ideal conditions, such as lack of wave transience, dissipation, and critical layers (Holton, 1974; Boyd, 1976; Dunkerton, 1980), the EP flux is zero. Hence, the waves have no effect on the evolution of the mean temperature and zonal velocity fields. This is known as the non-interaction theorem. Instead, the wave fluxes drive a mean circulation which cancels terms in the momentum and heat equations that would give rise to local acceleration of the slowly varying state U , and T . Although there are no critical layers for the waves in the 21 day band discussed here, since the phase speed is much more westward than zonal velocity observed, the 21-day waves are not small amplitude since they have a velocity amplitude of about 30 cm s^{-1} compared with the mean Undercurrent velocity maximum of about 100 cm s^{-1} , and dissipation is most certainly present in the real ocean. It is useful however, to examine the EP flux divergence as a diagnostic of wave-mean flow interaction because it represents the total eddy forcing of the mean zonal flow and thus can be used as an important observational tool (Edmon, et al., 1980) in studying the eddy-driven motions. Even if there is no cancellation of the mean and eddy-driven flows, and the EP flux is non-divergent, the calculation of the EP flux divergence can give insight into the role of the waves in the dynamics of the mean flow. The theory presented below follows more rigorous formulations elsewhere (Holton, 1974; Andrews and McIntyre, 1976; Boyd, 1976; and Pedlosky, 1987a).

Theory

The slow evolution in time τ of a spatially varying flow zonal U and temperature field T can be written at order ϵ^2 , where ϵ is a small parameter equal to the ratio of the wave scale $|u|$ to the mean zonal flow scale $|U|$, as derived in the Appendix:

$$U_\tau + UU_X - V(f - U_y) + W U_z + P_X = -\langle (uv)_y + (uw)_z \rangle + M^X$$

$$T_\tau + UT_X + VT_y + WT_z = -\langle (vT)_y + (wT)_z \rangle + Q$$

where the subscripts τ and X denote differentiation of the slowly varying fields in time and in the zonal direction, and M^X and Q are mechanical and thermodynamic forcing.

Define an wave-induced circulation (V_e, W_e) such that,

$$\partial(V_e)/\partial y + \partial(W_e)/\partial z = 0$$

for continuity, with W_e given by

$$W_e = -\langle (vT/T_z)_y \rangle,$$

which implies,

$$V_e = \langle (vT/T_z)_z \rangle.$$

Hence the wave flux term vT/T_z defines a streamfunction for the eddy-driven mean circulation. With substitution, the mean temperature equation (derived in Appendix) becomes,

$$T_\tau + (W - W_e)T_z + V T_y = -\langle (wT)_z \rangle + Q.$$

Assuming the following balance in the wave temperature equation (derived in Appendix):

$$-i(\omega - Uk)T + v T_y + w T_z = q,$$

where q is the diabatic heating, an expression for wT can be written in terms of V_e , by operating on the complex conjugate of the wave temperature equation by T and then taking the real part to yield:

$$wT = -vT T_y/T_z + qT/T_z.$$

Substituting into the mean temperature equation yields the following expression for the temporal evolution of the slowly-varying temperature field:

$$T_\tau + (V - V_e)T_y + (W - W_e)T_z = -(qT/T_z)_z.$$

Similarly, substitution in the mean momentum equation (derived in Appendix), yields:

$$U_\tau - (f - U_y)(V - V_e) + (W - W_e)U_z + P_\chi = \nabla \cdot \mathbf{E} + M^x$$

where \mathbf{E} is the Eliassen-Palm flux vector (E_y, E_z), with

$$E_y = -\left\{ uv - U_z \frac{vT}{T_z} \right\},$$

$$E_z = -\left\{ uw - (f - U_y) \frac{vT}{T_z} \right\}.$$

In the above evolution equations, the advection of the mean flow is accomplished by a *residual* meridional-vertical circulation given by $V-V_e$ and $W-W_e$.

This formulation specifically relies upon the assumption that terms like VT_y and WT_z which are the meridional and vertical advection of temperature anomalies by the large-scale slow field, and $(uT)_x$, are small compared with the terms $u \cdot \nabla T$ and $\nabla \cdot uT$ in the wave temperature equation. These terms are formally of higher order in the disturbance amplitude for small amplitude waves as described in the Appendix. However, as noted above, these waves are not strictly small compared with the mean flow scale. Fortunately, the observations supply justification for neglecting these terms. For the observations under consideration, the term VT_y is estimated to be in the range of 0.04 to $0.25 \times 10^{-6} \text{ }^\circ\text{C s}^{-1}$ using a mean meridional velocity of 1 to 5 cm s^{-1} and a meridional difference of the wave amplitude of T of about 0.5°C over the 110 km meridional separation of the array. Compared with an estimate of $(vT)_y$ of about $1.1 \times 10^{-6} \text{ }^\circ\text{C s}^{-1}$ at a depth of 20 m , this term is negligible. Likewise, the term vT_y , with an estimate for the magnitude of v of about 30 cm s^{-1} and an estimate of T_y of about 4.6×10^{-8} at 20 m , is much larger at $1.4 \times 10^{-6} \text{ }^\circ\text{C s}^{-1}$. Thus, the slow advection of the temperature anomaly appears to be much smaller than the advection of the slowly-varying large-scale temperature gradient by the wave velocity field and the assumptions are justified.

Results

The cospectrum of v and T for the 21-day band, presented in Table 3.16, provides an estimate of the meridional heat flux convergence. The cospectrum of vT shows a southward flux of heat due to the 21-day waves, which is coherent and larger at the northern site leading to a net convergent transport of heat. This net heat convergence obtained from differences over the northern and southern values except at 50 m where the northern and equatorial values are used, when integrated to 87.5 m, using trapezoidal integration over the 20, 50, and 75 depth levels, yields a net heating of about 360 W m^{-2} . Since, no rise in heat content is observed over the time span of the array, this enormous amount of heating must be balanced by another component of the system.

The streamfunction for the eddy-induced mean flow, given by vT/T_z with vT calculated from the cospectrum of the 21-day band (table 3.16), is shown and contoured in figure 3.4. The vertical gradient of the mean temperature T varied by an order of magnitude throughout the water column ranging from $0.9 \times 10^{-3} \text{ }^{\circ}\text{C cm}^{-1}$ in the upper portion of the array to $0.1 \times 10^{-3} \text{ }^{\circ}\text{C cm}^{-1}$, at 150 m depth, and this gradient contributes substantially to the estimates of V_e . Values of vT significant at the 95% confidence level are indicated by asterisk in table 3.16. No estimates significant at the 95% level are observed at the southern location. At the equatorial and northern mooring sites however, significant fluxes to 100 m and 200 m respectively are found. For this reason, in the calculation of W_e , which requires meridional differences of vT , the results are shown for various differencing schemes in table 3.17. Values in parentheses denote that the estimate was obtained using a vertically interpolated value at the northern or southern site.

TABLE 3.16 COSPECTRUM OF V AND T, C(vT)

	N		E		S	
depth(m)	C(vT)	Coh	C(vT)	coh	C(vT)	coh
20	<u>-15.9</u>	.75	<u>-12.0</u>	.60	-3.9	.31
50	<u>-12.4</u>	.74	<u>-7.4</u>	.75		
75	<u>-11.2</u>	.76			0.3	.40
100			<u>-3.5</u>	.73	-.44	.23
150	<u>-1.4</u>	.66	.02	.17		
200	<u>-0.9</u>	.64			0.3	.22
250	-0.9	.48	0.20	.14	.08	.30

Table 3.16: Cospectrum and coherence of v and T for the 36.8 to 14.2 day band. Estimates of the cospectrum that are significantly different from zero at the 95% confidence level are underlined.

For the wave-driven meridional and vertical momentum fluxes of zonal momentum to cancel the meridional and vertical fluxes of zonal momentum such that there is a tendency for non-interaction, the wave-driven velocity field (V_e , W_e) must be nearly equal to the mean meridional and vertical velocity field (V , W) and the EP flux divergence must also cancel.

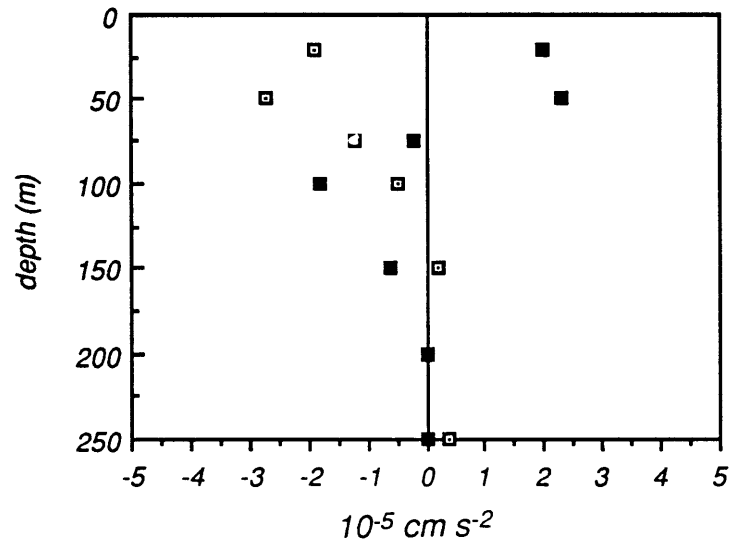
TABLE 3.17 EDDY-INDUCED CIRCULATION, W_e AND V_e

W_e 10^{-3}cm s^{-1}				V_e cm s^{-1}			
	N	E	S		N	E	S
20	0.8	1.2	1.6	35.5	-1.3	-1.9	-0.7
50	1.0	(1.1)		62.5	-0.5	-0.5	-0.7
75		1.1		87.5	-0.8	-0.5	-0.4
100		(0.9)	1.2	125	-0.7	-1.0	-0.2
150	1.1	(0.8)		175	-0.8	-0.3	-0.2
200		0.5		225	0	-0.3	-0.4
250	0.9	0.4	-0.2				

Table 3.17: Estimates of the eddy-induced circulation (V_e , W_e) as calculated from the streamfunction $(vT)/T_z$. Values in parentheses indicate that the estimate was obtained using an interpolated value at the northern or southern mooring.

Table 3.17 presents estimates of the eddy-driven circulation W_e and V_e . The contours of vT/T_z , that is the streamlines of the eddy-induced circulation, appear to slope upward from the northern location to the southern location as shown in figure 3.3. This pattern suggests a wave-driven flow that is both southward and upward which is similar in pattern to the observed mean meridional - vertical velocity field. However, as Table 3.17 indicates, the actual magnitude of V_e is smaller than the observed mean field shown in Table 3.2. Thus, in this case, the advection by the eddy-induced meridional velocity field is very small and negligible compared to other terms in the momentum balance. In addition, the eddy-induced vertical velocity is about half as large as the mean vertical velocity field inferred as described earlier, and thus would only cancel half of the mean vertical

A



B

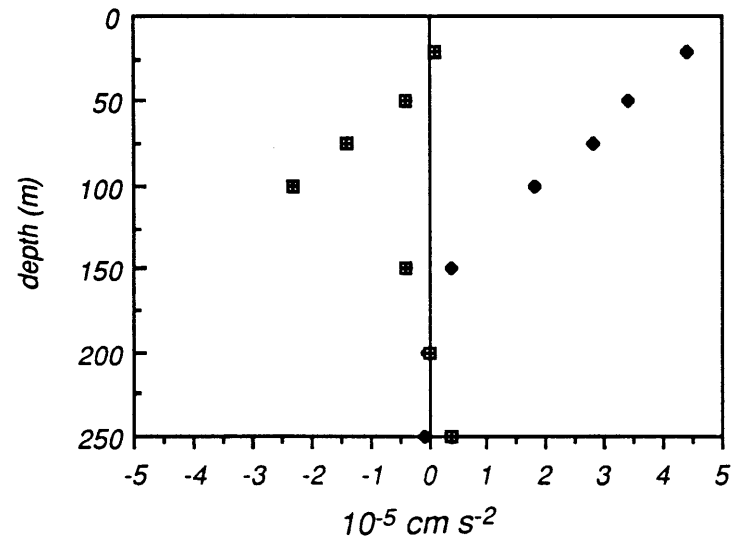


Figure 3.4: Profiles of (A) individual terms in the EP flux divergence, E_y (open boxes) and E_z (solid boxes), as listed in Table 3.17; and (B) the total EP flux divergence (boxes) and the zonal pressure gradient force (diamonds).

inertial acceleration term. The effect of $V_e U_y$ compared with that of $V U_y$ is very small, considering that V_e is almost an order of magnitude smaller than V .

TABLE 3.18 ELIASSEN - PALM FLUX DIVERGENCE

	$U_z vT/T_z$ $\text{cm}^2 \text{s}^{-1}$			$U_y vT/T_z$	E_y^y	E_z^z	div E
	N	E	S	E	10^{-5}cm s^{-1}		
20	313	306	95	.029	-1.9	2.0	0.1
50	207	189	38	.028	-2.7	2.3	-0.4
75	91	0	1.6	.027	-1.2	-0.2	-1.4
100	-18	-46	6.5	.015	-0.5	-1.8	-2.3
150	-28	-6	11.6	.002	0.2	-0.6	-.4
200	-12	2.5	15	-.003	0.0	0	0
250	-12	10	5	.001	0.4	0	.4

Table 3.18: Estimates of the Eliassen-Palm fluxes E^y and E^z , and the flux divergence. Linear interpolation is used to obtain values at depths where no estimate of vT is obtained.

Since, the eddy-induced mean flow field is in the same direction as the mean meridional-vertical velocity vector, its sense of direction is such that it has a *tendency* to cancel out the acceleration of the mean zonal velocity by the mean inertial acceleration terms $V U_y + W U_z$, though because the eddy-induced velocities are small, the cancellation is not complete. However, with the mean zonal momentum equation as written here, this tendency for cancellation is balanced by part of the E-P flux divergence shown in Table 3.18.

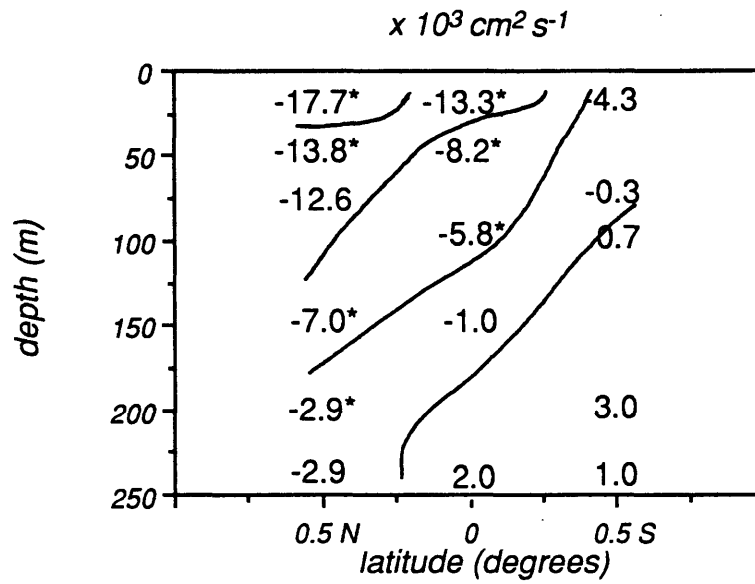


Figure 3.3: Contoured section across the array of the eddy-driven streamfunction, $(vT)/T_z$ due to the fluctuations in the 14.2 to 36.8 day band.

This new formulation offers an interpretation of the complete role of the eddies in the zonal momentum balance because now all the eddy forcing of the mean zonal flow appears explicitly in the form of the EP flux divergence. The part of the mean flow acceleration by the mean flow (W, V), that is eddy-induced, $W_e U_z + V_e U_y$, is combined with the Reynolds stress divergence terms to form a divergence of a new flux called the EP flux. The eddy-induced terms appear only because of the baroclinicity of the flow. Table 3.18 presents the final estimates of the role of the 21 day motions in the zonal momentum balance of the Undercurrent through an estimate of the EP flux divergence terms.

Figure 3.4 (A) presents the profiles of the individual terms in the EP flux divergence and their sum with the zonal pressure gradient force, figure 3.4 (B). The meridional divergence of the EP flux is negative in the upper part of the array, decreasing to zero below about 100 m. The vertical divergence of the EP flux, is positive down to 62.5 m, increasing to negative values which reach a maximum at 100 m then drop to negligible values below 150 m. In the upper part of the array above the core, the EP flux divergence is nearly zero. At the levels of the core and below the EP flux divergence is negative implying a decelerative effect. Together, these profiles are shown in figure 3.4 (A). The interpretation is clear: *The eddies work directly through the Reynolds stress divergence and indirectly through eddy-driven mean inertial accelerations to balance the pressure gradient force at the depth of the core where the turbulent stress divergence is small. Above the core where the turbulent stress divergence can act to balance the pressure gradient, there is very little net effect of the eddies.*

As discussed earlier these waves do not satisfy the requirements for the noninteraction or nonacceleration theorem. But it is observed in the upper part of the array that the EP flux divergence is negligible. This is consistent with the observation that the wave amplitudes do not grow appreciably during this time series. Cox (1980) attributes the lack of highly non-linear features, such as closed streamlines, after the growth of the instability waves to finite amplitude in his numerical model, as being due to the ability of the equatorial waves to transport energy away from the unstable near surface regions into the deeper layers. This mechanism may be at work here since these in Chapter 2 it is suggested that the waves propagate energy downwards.

If the waves do satisfy WKB scaling, then it can be shown (Edmon et al., 1980), that the EP flux E is proportional to the group velocity of the wave packet C_g by the wave activity A ,

$$E = C_g A.$$

The wave activity A is conserved when there is no dissipation and is positive definite when there is no change of sign of the large-scale mean potential vorticity. Thus, the sign of E gives a direction for the propagation of wave energy.

As estimated here, in Table 3.19, the vertical component of the EP flux is negative on the equator and largest at the core of the Undercurrent, implying downward group velocity. The meridional component is negative implying southward group velocity. Thus the energy from the mean flow instability which is fed into the waves for local growth, discussed in the next Chapter, is moved out of the region presumably at the rate necessary to keep the amplitude steady over time.

TABLE 3.19: ELIASSEN -PALM FLUX VECTOR

depth (m)	E^y	E^z
20	-380	-.01
50	-180	-.07
75	-30	-.14
100	50	-.06

Table 3.19: The components of the EP flux vector (E^y , E^z) which determine the direction of group velocity. The fluxes are estimated at the equator by $\{-(uv - U_z \frac{vT}{T_z}), -(uw + U_y \frac{vT}{T_z})\}$, where the terms proportional to vT are found in Table 3.18.

3.5 PARAMETERIZING THE VERTICAL EDDY MOMENTUM FLUX

It is essential to understand the dynamical behavior of smaller scale motions in terms of their feedback on the large scale flows as well as to be able to predictively model their behavior. One typical approach in the "closure problem" has been to model numerically or analytically this wave-mean flow interaction wholly in terms of the larger resolved flow scale. Many different parameterization schemes have been suggested and implemented for this purpose. While it is perhaps better to develop and study models that resolve the smaller scales, it is useful to define under what conditions parameterization of the wave-mean flow interaction is sensible or even possible.

The effects of the eddy Reynolds stresses on the momentum balance of the Equatorial Undercurrent observed here suggest a model for wave-mean flow interaction that can be utilized to reveal possible parameterizations. Bryden and Brady (1988) discuss the parameterization of the effects of the horizontal Reynolds stress divergence. It was found that the spatial distribution of the covariance of the northward and eastward eddy velocity $u'v'$, for time-series ranging in duration of 208 to 701 days, from mooring groups located at 152°W and 110°W (inclusive of the deployments discussed here), showed a meridional divergence above the location of the core of the Equatorial Undercurrent, and a convergence below the core as reported here for the 21 d spectral band. Dividing the divergence estimated at each depth by the observed meridional curvature of zonal velocity yielded positive horizontal eddy viscosities above the core with negative values below, all with magnitudes in the range of 0.5 to $5 \times 10^7 \text{ cm}^2 \text{ s}^{-1}$.

The profile of uw estimated here allows the vertical eddy Reynolds stress to be compared directly to the Undercurrent velocity profile in order to investigate whether there is a relationship and hence whether a simple parameterization scheme can be developed.

The standard method of parameterizing the effect of the eddy Reynolds stress divergence on a mean flow is through the use of an eddy viscosity coefficient A , such that the divergence of the Reynolds stress is modelled as a divergence of a shear stress:

$$-(uw)_z = (A U_z)_z.$$

Usually, the first premise in the argument for such a scheme is that the Reynolds stress is modelled as a shear stress such that

$$-uw = A U_z.$$

However here, it appears that the profile of uw goes through a maximum in the vertical at the same location where U_z is zero. Whereas the first expression is valid in this case, the second is not. This is seen as follows: It appears that the profile of uw is approximately proportional to the profile of U . Starting with the first expression, and expanding the right hand side, gives

$$-(uw)_z = A_z U_z + A U_{zz},$$

assuming that A is a function of depth. The estimated vertical momentum flux is maximum at the Undercurrent velocity core, indicating that AU_{zz} must be zero at the core, where U_z and $(uw)_z$ are separately zero. This implies that since U_{zz} is not zero at the core, A must be zero there. Above and below the core depth, the velocity shear is nearly constant with depth. Referring to section 3.2, U_z was actually in practice assumed to be constant in order to extrapolate for the velocity core. Thus in these regions, U_{zz} is small. Above and below the core then the stress divergence can be modeled as,

$$-(uw)_z \approx A_z U_z.$$

Using the above expression, estimates for A_z are obtained by dividing the estimated vertical momentum flux divergence shown in figure 3.3, by the observed zonal velocity shear of -.023 between 20 and 75 m and 0.008 between 75 and 100 m as listed in Table 3.10. The results are shown in Table 3.20. Then assuming A is zero according to this model at 75 m, where the velocity maximum is located, A is estimated by integrating the Table 3.20 values of A_z to the mean locations 47.5 and 87.5 m.

TABLE 3.20 VERTICAL EDDY VISCOSITY, A ($\text{cm}^2 \text{s}^{-1}$)

depth(m)	A_z (cm s^{-1})	depth (m)	A ($\text{cm}^2 \text{s}^{-1}$)
20, 75	-1.0×10^{-3}	47.5	-3
75, 100	-3.5×10^{-3}	87.5	4

Table 3.20: Estimates of the vertical eddy viscosity coefficient A , associated with the effects of the vertical Reynolds stress estimated for the 21 day wave band.

Results

Thus for A , Table 3.20, yields a negative value of $-3 \text{ cm}^2 \text{s}^{-1}$ above the core and a positive value of $4 \text{ cm}^2 \text{s}^{-1}$ below. The size of these values is consistent with other estimates. Wyrski and Bennett (1969) obtained a value of $3 \text{ cm}^2 \text{s}^{-1}$ with another heuristic method. It is of interest, however, to note that the viscosity is negative above the core which has not been observed or estimated before. This negative viscosity coefficient implies an eastward acceleration by *eddy mixing*, or through a redistribution of momentum.

Some of the earlier points need to be rediscussed. In the region above the core, the vertical Reynolds stress divergence acts as an accelerative force, while below the core, it acts as a decelerative force. This is reflected in the sign of the eddy viscosity coefficient which is negative above the core—opposite to what is expected from turbulence. A typical eddy viscosity coefficient for the dissipative turbulent scales is observed to range from around $10\text{--}15 \text{ cm}^2 \text{s}^{-1}$ near the surface to less than $1 \text{ cm}^2 \text{s}^{-1}$ near the core (Dillon et al., 1989). It would appear that the vertical stress divergence of the 21-day waves is opposite to the effect of the dissipative scales in this depth range. However, when the effect of the horizontal Reynolds stress divergence is considered, the overall divergence of the Reynolds stress produces a decelerative effect both above and below the core. The vertical Reynolds

stress divergence above the core compensates partially the horizontal Reynolds stress divergence.

In order to assess the usefulness of such a scheme in parameterizing the eddy effects in numerical models, it would appear that more investigation is needed because the effect is comparable to the wind forcing. The results presented here are meant to be applicable in a more heuristic sense since these estimates depend entirely on the validity of the assumptions that $A = 0$ at the velocity maximum and that the maximum is at 75 m. The extent to which other bands of eddy activity, such as the 4-5 day inertial-gravity waves observed by Wunsch and Gill (1982), contribute to the momentum redistribution in the equatorial ocean might be explored using the technique used here for obtaining the vertical Reynolds stress from the quadrature of zonal velocity and temperature.

CHAPTER 4:

Energy Conversion

4.1 INTRODUCTION AND OBJECTIVE

The question of why a particular wave mode is observed is fundamentally connected to the concept of energy transfer between scales of motion. Evolving disturbances that are forced at a boundary for example, are supplied at least initially with the energy necessary for continued growth from the forcing itself. However, the survival in time of any of the various wave modes generated by an unstable flow, may depend not only upon a fast initial rate of growth, but also on how effectively the unstable flow can continue to transfer energy to the growing disturbance after reaching a finite amplitude where non-linear interactions will provide the stage for competition among the spectrum of different wave modes and harmonics generated. Also, at some stage in the development of the disturbance, dissipation will become important such that wave energy is fed to smaller scales of motion. Or the wave may find a critical level along its path of propagation, where wave energy is fed back to the mean flow. Or as seems to be the case here, the wave may radiate energy away from the region of forcing.

This set of observations is well suited for exploring the nature of the energy transfer process that may exist between the basic state flow, here defined as the time-mean current over the length of the record used, and the fluctuations about that mean state, that have already been shown in a previous section to propagate along the equatorial wave guide much like a mixed Rossby-gravity mode. This is because, as is shown in the auto spectra of the 312 d long record of the zonal velocity record at the 20 m level on the equatorial mooring, figure 4.1, two frequency bands of variance dominate: the low frequency seasonal band and the higher frequency narrow band centered around the 21 d period. Thus, the measurements themselves provide the

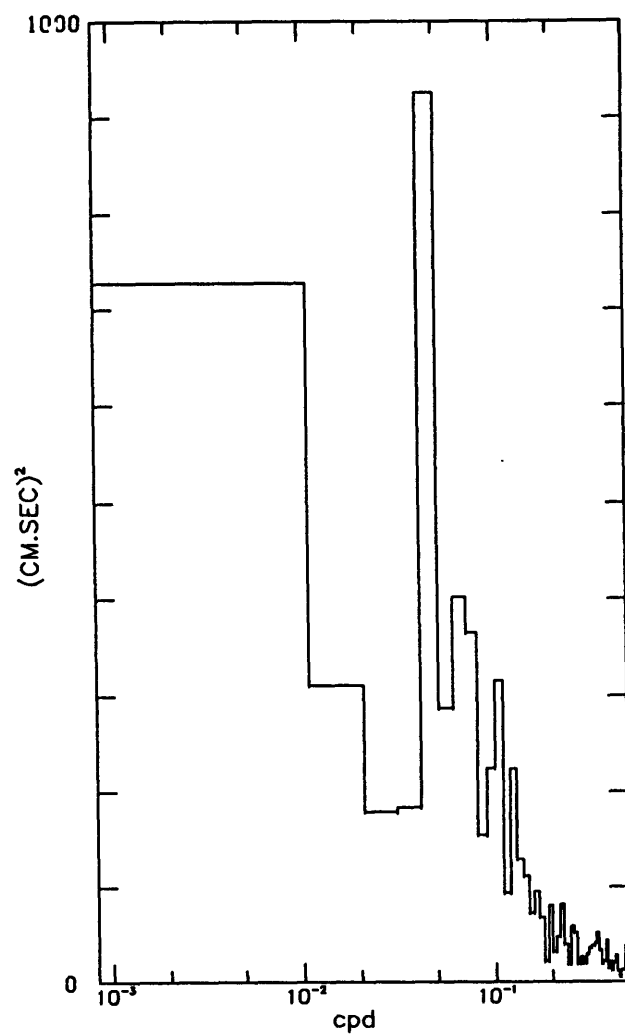


Figure 4.1 Auto spectrum of east velocity for the 20 m, 312 day long record on the equatorial mooring.

motivation for the use of the multiple time-scale formulation to the wave-mean flow interaction problem as developed in the Appendix.

In Chapter 3 the mean state for the 184 d long record was shown to consist of a geostrophically balanced jet-like zonal flow and a meridional circulation which, in the upper level, exhibits a strong divergence. It will be seen that the presence of the divergence of the meridional surface flow at the equator is important in the energy transfer process in locally limiting the growth of the eddy kinetic energy. Thus, in deriving the evolution equations for eddy kinetic and potential energy (EKE and EPE) and mean kinetic energy, (MKE) the field variables are partitioned into a mean field, $U(X,y,z,\tau)$, $V(X,y,z,\tau)$, and $T(X,y,z,\tau)$, which varies slowly on a time scale τ and zonal scale X , and an eddy field, $u(x,y,z,t)$, $v(x,y,z,t)$, and $T(x,y,z,t)$, which fluctuates on a fast time scale ω^{-1} and zonal scale k^{-1} . Other discussions of the equations are found in Bryden (1982) and Hall (1986). The evolution equations for these fields are derived in the Appendix.

Eddy Kinetic Energy

The equation for the rate of change of eddy kinetic energy, obtained by multiplying the wave momentum equations for u and v (derived in the Appendix) by u and v respectively and adding together, is written:

$$\frac{d}{dt} \frac{(u^2 + v^2)}{2} = -uvU_y - v^2V_y - uwU_z - (up)_x - (vp)_y - (wp)_z + g\alpha wT - \text{dissipation.}$$

where $\frac{d}{dt} = \frac{\partial}{\partial t} + U \frac{d}{dx}$. The eddy kinetic energy grows as a result of a conversion from the mean kinetic energy through the shear production terms,

$$-uvU_y - v^2V_y - uwU_z$$

through a divergence of eddy pressure work,

$$-(up)_x - (vp)_y - (wp)_z$$

and through conversion from eddy potential energy,

$$g\alpha wT.$$

Only the shear production terms are estimated here with estimates of the fluxes of momentum from the 21 day band. The first of the shear production terms represents a conversion of MKE to EKE through barotropic instability. The last of the shear production terms, representing a conversion through a vertical shear instability process, sometimes called Kelvin-Helmholtz instability, can only be indirectly estimated, with uw inferred in Chapter 3 using an assumed eddy heat balance. The second shear production term, proportional to the mean meridional divergence, is higher order than the other shear production terms, according to the scaling presented in the Appendix, however, due to the large meridional divergence observed, it is kept here. It is impossible to estimate the divergence of the eddy pressure work, due to lack of information about eddy pressure. In general, the pressure work is extraordinarily difficult to estimate because it represents the divergence of pressure fluxes due to the ageostrophic component of flow. However, integrated over a closed region, the eddy pressure work vanishes.

The equation for the growth of eddy potential energy, obtained by multiplying the eddy temperature equation (in the Appendix) by T , is written,

$$\frac{d}{dt} \frac{g\alpha T^2}{2T_z} = -g\alpha vT \frac{T_y}{T_z} - g\alpha wT.$$

This equation states that the eddy potential energy grows as a result of a conversion of mean available potential energy to eddy potential energy through work against the mean sloping temperature gradients,

$$-g\alpha vT (T_y/T_z),$$

or as a result of an exchange between EKE and EPE,

$$-g\alpha wT.$$

An estimate for the 36.8 to 14.2 day band is obtained for the conversion of mean available potential energy to eddy potential energy through baroclinic instability. The exchange of EPE and EKE, $g\alpha wT$, cannot be reliably estimated, however, by assuming it does not upset the balance in the EPE evolution equation due to growth of the waves by conversion from MAPE, its relative size may be inferred. When compared to the other terms in the EKE

equation, it is inferred to be much smaller, suggesting that baroclinic instability is not important to the growth of the waves.

The equation for the growth of kinetic energy of the mean state, obtained by multiplying the the horizontal mean flow momentum equations by U and V respectively, and adding, is written:

$$\frac{d}{d\tau} \frac{(U^2 + V^2)}{2} = - U(uv)_y - V(v^2)_y - U(uw)_z - \nabla \cdot (UP) - \text{dissipation},$$

where $\frac{d}{d\tau} = \frac{d}{dt} + U \frac{d}{dX}$. The conversion from the eddy kinetic energy to mean flow kinetic energy will be estimated in order to investigate whether the system, defined by the waves and the mean Undercurrent, locally conserves energy.

The system will locally conserve energy through interaction of the mean and eddy components if the local conversion of eddy kinetic energy to mean kinetic energy and the mean kinetic energy to eddy kinetic energy sums to zero. Locally these conversion terms sum to the divergence,

$$-(uvU + v^2V)_y - (uwU)_z.$$

This flux divergence is not necessarily zero in any particular region of the open ocean, but because the fluxes are zero at the ocean boundaries, when integrated over the entire ocean the flux divergence is zero. Thus, a non-zero divergence of this flux at a particular location requires that there must be a net export or import of energy balanced by the circulation elsewhere in the ocean basin outside of the region of interest. It is important to consider the possibility of such fluxes in open ocean regions such as the one of interest here.

The objective of this chapter is to assess the importance of each of the conversion terms to ascertain whether or not the source of eddy energy is the local Undercurrent. If so, an instability mechanism is fundamental to the existence of the 21-day waves.

4.2 METHOD

The sparse configuration of the mooring array creates some difficulty in the calculation of the energy conversion terms. The first assumption made to alleviate some of the difficulty, is that a finite difference between the northern and equatorial value of a particular variable (or between the equatorial and southern value) will be considered here as solely a meridional difference. This is probably a reasonable assumption given that the zonal scale of variation in a quantity along the equator is usually assumed to be much larger than the meridional scale of variation (the long-wave approximation) and the east-west separation of the moorings is only about 100 km.

The other difficulty arises due to the jet-like structure of the Undercurrent, the divergent mean meridional circulation, and the meridional structure of the second order eddy properties. Since both the eddy and mean fields display at some depths, a minimum or a maximum at the equatorial location, it becomes tricky to make a representative estimate for the entire array of the energy conversion terms which are calculated from the product of one of the above fields (mean or eddy) and the meridional gradient of the other (eddy or mean). The method used to estimate, for example, $-uvU_y$ and $-(uv)_y U$ is as follows:

$$-uvU_y = -\frac{1}{2\Delta y} \left\{ \frac{[uv(N)+uv(E)]}{2} [U(N)-U(E)] + \frac{[uv(E)+uv(S)]}{2} [U(E)-U(S)] \right\}$$

$$-(uv)_y U = -\frac{1}{2\Delta y} \left\{ \frac{[U(N)+U(E)]}{2} [uv(N)-uv(E)] + \frac{[U(E)+U(S)]}{2} [uv(E)-uv(S)] \right\}$$

such that the sum,

$$-uvU_y - (uv)_y U = -\frac{1}{2\Delta y} \{ U(N)uv(N) - U(S)uv(S) \} = -(uvU)_y.$$

The other terms involving horizontal estimates are calculated in the same way, with $2\Delta y$ being the meridional distance between the northern and

southern moorings. The resulting estimates (Tables 4.1, 4.2 and 4.4) are discussed in the following sections.

TABLE 4.1: MEAN TO EDDY KINETIC ENERGY CONVERSION

depth (m)	$-uv \partial U / \partial y$	$-v^2 \partial V / \partial y$	$-uw \partial U / \partial z$	total
	$(10^{-3} \text{ cm}^2 \text{ s}^{-1})$			
20	1.5	-1.8	-0.5	-0.8
50	1.5	-0.4	0.9	2.0
75	0.8	0.0	0.0	0.8
100	-0.1	0.0	-0.3	-0.4
ave.	1.1	-0.7	0.0	0.4

Table 4.1: Estimates of the conversion of mean to eddy kinetic energy in units of $\text{cm}^2 \text{ s}^{-3}$ for the 21-day band estimates. The row labeled “ave.” is the depth-integrated average from 0 to 100 m.

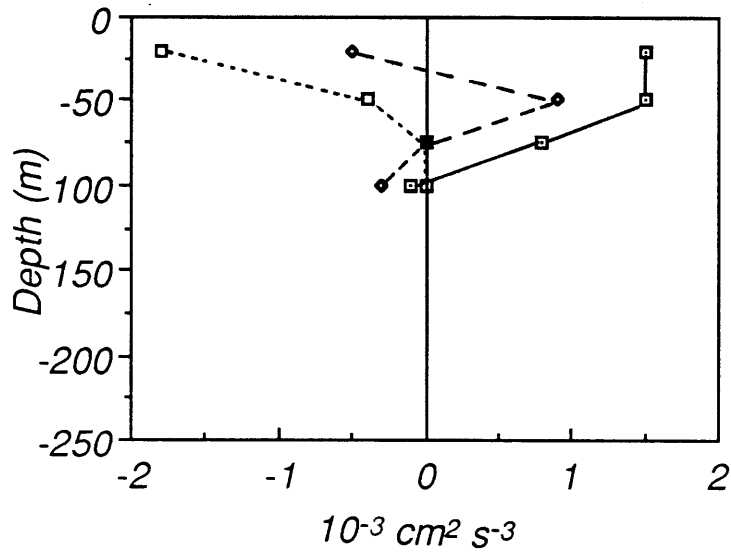
4.3 LOCAL KINETIC ENERGY CONVERSION

There are a number of different approaches to discussing the kinetic energy conversion estimates (Table 4.1, Figure 4.2). Overall, by obtaining the contribution to the depth average to 100 m for each separate term and integrating, it is found that EKE is gained through local exchange of MKE at a rate of $0.4 \times 10^{-3} \text{ cm}^2 \text{ s}^{-3}$. Correspondingly, MKE is lost through local interaction with the eddies at a rate of $-0.6 \times 10^{-3} \text{ cm}^2 \text{ s}^{-3}$ (Table 4.2, Figure 4.2). With a depth-integrated average to 100 m of EKE of $580 \text{ cm}^2 \text{ s}^{-2}$, an e-folding time scale ϵ for the growth of EKE can be estimated as follows:

$$\text{EKE} / \epsilon = d(\text{EKE}) / dt,$$

yielding about 17 days for the estimate of ϵ . This e-folding scale compares reasonably well to the faster end of Philander's theoretically predicted time scale range of 2 to 3 weeks (Philander, 1976). The approximate balance of these two growth and decay rate estimates strongly suggests that the eddies

A



B

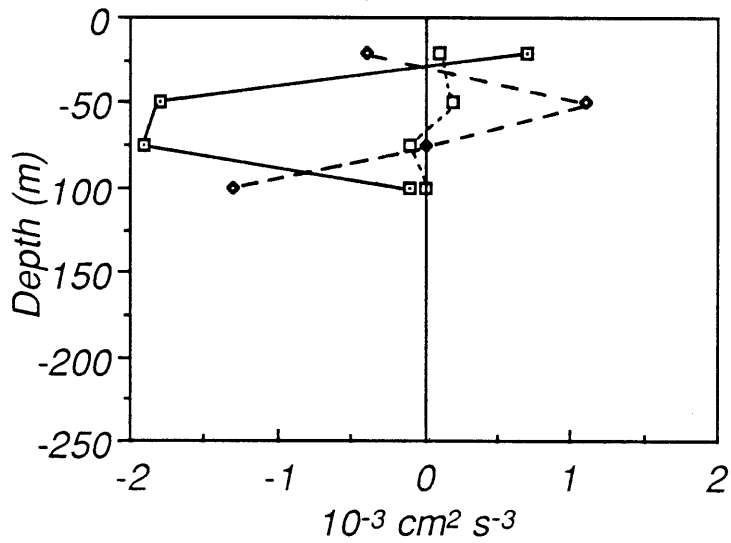


Figure 4.2: Profile of the conversion of Mean Kinetic Energy to Eddy Kinetic Energy through shear production (A). Profile of the conversion of Eddy Kinetic Energy to Mean Kinetic Energy through shear instability (B). Solid lines connect estimates of $-uvU_y$ in (A) and $-U(uv)_y$ in (B); Long dashed line connects estimates of $-uwU_z$ in (A) and $-U(uw)_z$ in (B); and short dashed line connects estimates of $-v^2V_y$ in (A) and $-V(v^2)_y$ in (B).

obtain the necessary energy for maintenance locally through the conversion of MKE by shear production. But the depth-averaged estimate for the growth of EKE of $0.4 \times 10^{-3} \text{ cm}^2 \text{ s}^{-3}$ is small compared with estimates at individual depths.

From closer inspection of the individual depth averaged estimates calculated over the upper 100 m, it appears that the overall growth rate obtained for EKE, (the sum of the three shear production terms) is smaller than the individual growth rate estimated for the term traditionally associated with the conversion of MKE to EKE through barotropic instability of a meridionally sheared eastward flow, $-uvU_y$. The depth-weighted average for this process alone is estimated as $1.1 \times 10^{-3} \text{ cm}^2 \text{ s}^{-3}$, with larger values of $1.5 \times 10^{-3} \text{ cm}^2 \text{ s}^{-3}$ observed at the upper depths of 20 and 50 m.

TABLE 4.2: EDDY TO MEAN KINETIC ENERGY CONVERSION

depth(m)	$-(uv)_y U$	$-(v^2)_y V$	$-(uw)_z U$	total
	$(10^{-3} \text{ cm}^2 \text{ s}^{-3})$			
20	0.7	0.1	-0.4	0.4
50	-1.8	0.2	1.1	-0.5
75	-1.9	-0.1	0.0	-2.0
100	-0.1	0.0	-1.3	-1.4
average	-0.7	0.1	0	-0.6

Table 4.2: Estimates of the conversion of eddy kinetic energy to mean kinetic energy using estimates for the 21 day band. The row labeled “average” is the depth-integrated average to 100 m.

What partially compensates for this large local gain observed in the upper depths is a large loss observed at 20 m through the term, $-v^2 V_y$,

associated with the mean meridional mass divergence in the surface layer, presumably produced by poleward Ekman drift due to the westward wind stress. The entire depth averaged estimate for this process which acts as a poleward drain of EKE, is $-0.7 \times 10^{-3} \text{ cm}^2 \text{ s}^{-3}$. These two processes combine to yield the small residual growth of $0.4 \times 10^{-3} \text{ cm}^2 \text{ s}^{-3}$.

The shear production term, $-uwU_z$, contributes nothing to the overall growth rate of eddy kinetic energy though it is shown to be relatively large in magnitude above the core of the Undercurrent. At 20 and 50 m it appears that there is a source of eddy kinetic energy through this term. In addition the complementary term in the equation for the growth of mean kinetic energy due to the eddies, $-(uw)_z U$, is also small integrated to 100 m, but shows a relatively large growth of mean kinetic energy above the core and a relatively large decay below the core of about equal magnitude.

TABLE 4.3: LOCAL KINETIC ENERGY EXCHANGE

depth(m)	$d(\text{EKE})/dt$ ($10^{-3} \text{ cm}^2 \text{ s}^{-3}$)	$d(\text{MKE})/dt$ ($10^{-3} \text{ cm}^2 \text{ s}^{-3}$)	total local system ($10^{-3} \text{ cm}^2 \text{ s}^{-3}$)
20	-0.8	0.4	-0.4
50	2.0	-0.5	1.5
75	0.8	-2.0	-1.2
100	-0.4	-1.5	-1.9
average	0.4	-0.6	-0.2

Table 4.3: Estimates of the rate of change of kinetic energy of the local system from the sum of the local kinetic energy exchange between the mean flow ($d(\text{MKE})/dt$) and eddies ($d(\text{EKE})/dt$). The row labeled average is the depth-integrated average to 100 m.

4.4 LOCAL POTENTIAL ENERGY CONVERSION

TABLE 4.4 EDDY POTENTIAL ENERGY CONVERSION

depth (m)	$-g\alpha(vT/T_z)T_y$ ($10^{-3} \text{ cm}^2 \text{ s}^{-3}$)
20	0.18
50	0.08
75	-0.11
100	0.004
average	0.05

Table 4.4: Eddy potential energy conversion for the array for the 21-day band. The row labeled “average” is the depth-integrated average from 0 to 100 m.

The estimates at each depth for the growth of eddy potential energy (EPE) by conversion from the mean available potential energy (MAPE) associated with work against a sloping thermocline, $-g\alpha vT (T_y/T_z)$, are shown in figure 4.3 (Table 4.4).

There is a positive conversion of MAPE to EPE near the surface due to the generally southward eddy heat flux directed against the downward sloping thermocline to the north, suggesting a possible source for eddy growth. With the depth-averaged growth rate of $0.05 \times 10^{-3} \text{ cm}^2 \text{ s}^{-3}$ and a depth-averaged EPE of $70 \text{ cm}^2 \text{ s}^{-2}$, an e-folding time scale for growth of 20 days is inferred. This suggests a similar growth through the mean to eddy potential energy exchange compared to the time scale of 2 to 3 weeks obtained from the mean to eddy kinetic conversion process. The eddy potential energy growth rate of $0.05 \times 10^{-3} \text{ cm}^2 \text{ s}^{-3}$, however, is an order of magnitude smaller than the average EKE growth rate of $0.4 \times 10^{-3} \text{ cm}^2 \text{ s}^{-3}$.

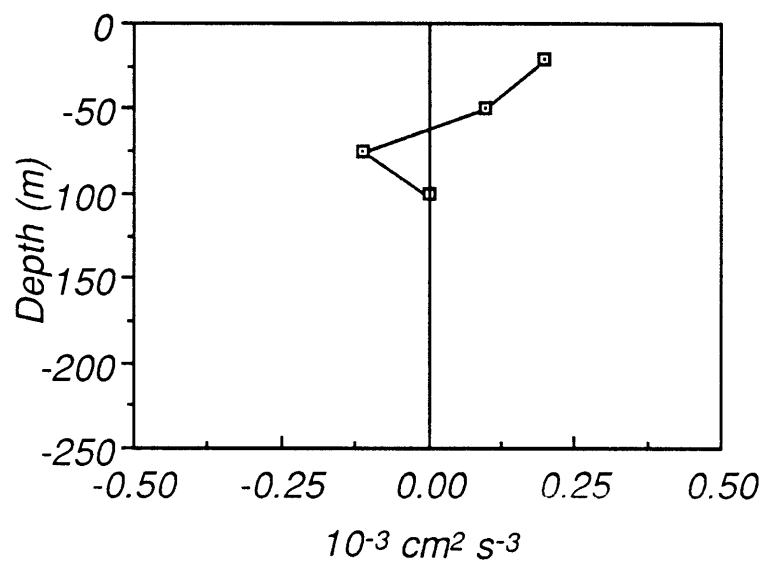


Figure 4.3 Profile of the conversion of Mean Available Potential Energy to Eddy Potential Energy.

The relatively small size of the EPE growth rate compared with the EKE growth rate implies that the evolution equations for EKE and EPE are uncoupled. The time scale of EPE growth is comparable to that obtained for EKE growth. Thus it would seem that the buoyancy flux term, the term that couples the two equations, is probably no larger than the conversion from MAPE to EPE, or the resulting time scale would be vastly different.

4.5 SUMMARY

In the depth range, 0 to 100 m, a local balance is observed to hold between the rate of conversion of MKE to EKE through lateral shear production ($0.4 \times 10^{-3} \text{ cm}^2 \text{ s}^{-3}$) and decay of MKE through eddy interaction ($0.6 \times 10^{-3} \text{ cm}^2 \text{ s}^{-3}$). An e-folding time scale of about 17 days is suggested for the growth of EKE through the shear production conversion mechanism. The overall rate of conversion of MKE to EKE attributed to the term $-uwU_z$, is negligible when depth averaged to 100 m but generally suggests a growth of EKE in the upper two depth levels.

In the surface layer, the large positive rate of conversion due to shear production due to barotropic instability of $1.5 \times 10^{-3} \text{ cm}^2 \text{ s}^{-3}$ nearly compensates the leakage poleward of EKE of $-1.8 \times 10^{-3} \text{ cm}^2 \text{ s}^{-3}$, accomplished by the conversion term involving the mean meridional mass divergence due to poleward Ekman drift.

The 21 day waves are mostly eddy kinetic energy since the depth-averaged EKE is an order of magnitude larger than the depth-averaged EPE. Compared with the substantial conversion of MKE to EKE, there is a small conversion in a depth average sense of MAPE to EPE of $0.05 \times 10^{-3} \text{ cm}^2 \text{ s}^{-3}$ to 100 m, which, with the depth-averaged estimate of EPE of $70 \text{ cm}^2 \text{ s}^{-2}$, yields a growth time scale on the order of 20 days, which is comparable to that obtained from KE conversion. The comparison of the two rates of conversion suggests that the growth of EKE accomplished through the buoyancy flux term is negligible in the EKE equation.

4.6 CONCLUSION

These results suggest that energy from lateral shear instability is fed into the waves in the 21 day band (36.8 to 14.2 d). However, as was discussed in Chapter 3, the wave amplitudes are not growing appreciably over the duration of the record examined here. The wave-mean flow interaction system does not satisfy the noninteraction theorem yet it appears that above the core of the Undercurrent, the divergence of the EP flux is negligible and here we find that the depth averaged energy conversion from mean to eddy, though positive, is smaller than the individual terms estimated at the depth levels. There seems to be considerable redistribution of energy in depth as there was for momentum discussed in Chapter 3. The waves lose energy at the surface level and possibly deeper, but gain energy in the region of the core. The mean flow loses energy at and below the core and gains energy above. It is difficult to determine how the energy is redistributed from the measurements here. The sum of the two terms represents the export out of the local region. Depth integrated, the system appears to be locally in balance with waves gaining energy and the mean flow losing a nearly equal amount, but the individual terms, appearing in table 4.3, indicate that at the various depth levels this is not the case. Energy must be redistributed—the profile suggests downwards energy flux below 50 m. But the system is by no means closed. Energy can be transported into the region from elsewhere, and exported out of the region through vertical propagation for example. A likely source region is to the north at about 5°N, where a band of eddy activity exists associated with the upwelling front, (Perigaud, 1989). In Chapter 2, evidence for a downward radiation of energy is presented from the vertical upward phase propagation of the disturbance; and again in Chapter 3, a downward and southward group velocity for the disturbance is suggested by the direction of the EP vector. The energy conversion results presented here seem to reinforce the downward energy flux observed in the previous chapters.

CHAPTER 5:

An Isentropic Analysis of the Pacific Equatorial Undercurrent

5.1 INTRODUCTION

The Equatorial Undercurrent (EUC), a strong eastward flowing sub-surface jet observed along the equator, is forced indirectly by the prevailing easterly component of the Trade winds, which sets up the eastward pressure gradient force. The westward surface flow, the South Equatorial Current (SEC), is forced directly by the drag of the westward wind stress on the surface of the ocean on the equator and by the wind stress curl off the equator. Because equatorial flows cannot adjust to steady equilibrium with the pressure field by flowing along isobars geostrophically, and because the mean pressure gradient force is eastward along the entire equatorial Pacific in the upper thermocline, except perhaps east of the Galapagos (Lukas, 1984; Wacongne, 1988), substantial turbulent dissipation is usually hypothesized in order to bring about a steady equilibrium and the downstream deceleration observed in the eastern Pacific. This hypothesis explained the early microstructure dissipation measurements which showed both a peak in the meridional distribution located at the equator and deep penetration of turbulent dissipation into the depths of the EUC (Crawford and Osborn, 1981), figure 5.1.

Recent microstructure observations made during the Tropic Heat Experiment in 1984 and again in 1987, revealed the existence of a strong diurnal cycle in both the amount of dissipation and the depth of its penetration (Gregg et al., 1985; Moum et al., 1986). The dissipation rate varies over 2 orders of magnitude on the diurnal cycle. The peak observed in the earlier measurements may be an artifact of aliasing the diurnal cycle according to Moum, et al. (1986), who found no significant increase in the equatorial dissipation rates integrated to the core depth of the EUC, over dissipation integrals observed off the equator. Contrary to what was found by

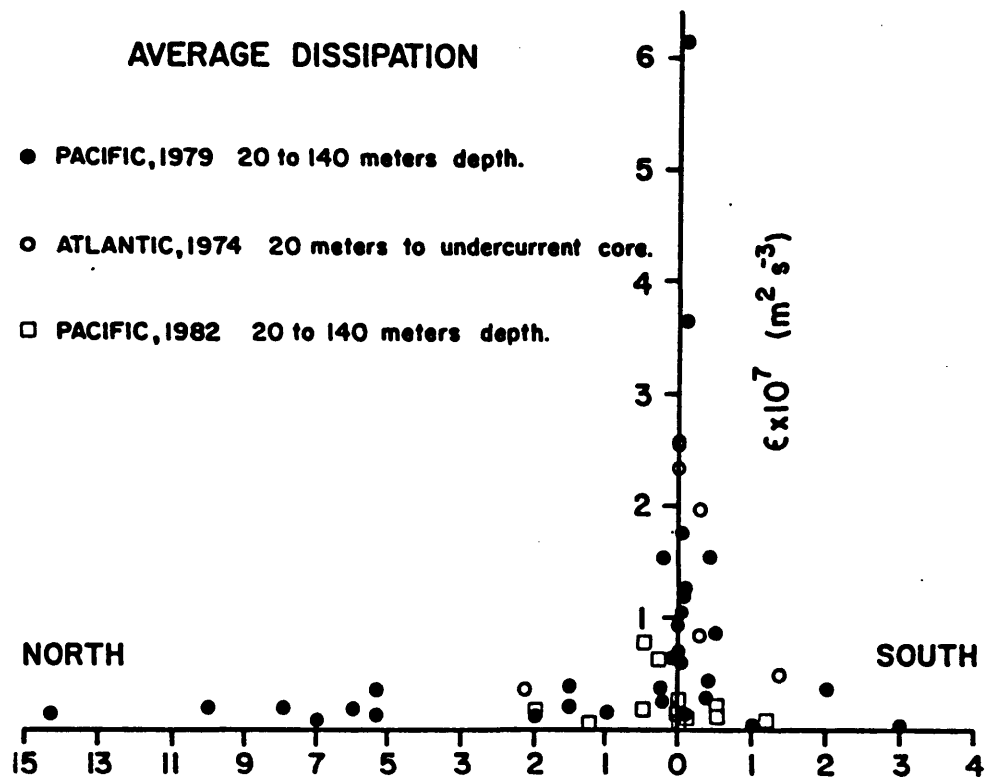


Figure 5.1: This figure, originally from Crawford (1982), shows averaged dissipation measured during three separate years in the Pacific and Atlantic oceans. The 1982 Pacific data was added by Moum et al., (1986). (Taken from Moum et al., 1986).

Moum et al. (1986), Peters et al. (1989) integrated independently observed dissipation rate profiles from the bottom of the mixed layer to the core depth of the Undercurrent, and found that the ensemble average dissipation integrals above the Undercurrent core were 2-3 times higher than average dissipation integrals away from the Undercurrent. The difference between the two studies was attributed to the fact that the Moum et al. (1986) integrals included the mixed layer dissipation rates. Since the mixed layer is deeper off the equator, the inclusion of the mixed layer dissipation rates led to otherwise larger depth integrals of dissipation. These new observations attempt to settle the question of whether the EUC is a location of higher dissipation above the core of the EUC where the Richardson numbers are quite low. But the question of what process is responsible for maintaining the steady state eastward flow of the Undercurrent at and beneath the core in the eastern Pacific remains unanswered.

The zonal pressure gradient has a much deeper decay scale of 150 - 200 m, than the observed turbulent stress divergence with a decay scale of 30 - 50 m as determined by the Tropic Heat dissipation studies (Dillon et al., 1989). The eastward pressure gradient force, when vertically integrated to depths below the Undercurrent where it is negligibly small, (figure 5.2), has been shown to nearly balance the westward wind stress (Arthur, 1960; Mangum and Hayes, 1982; Bryden and Brady, 1985). What balances the zonal pressure gradient as a function of depth within the thermocline at the core of the Undercurrent below the depth of penetration of the turbulent stress divergence? The other terms in the zonal momentum balance, the wave flux divergence and the mean inertial acceleration, may redistribute the westward wind stress applied to the upper boundary layer downward into the thermocline to balance the pressure gradient force. The purpose of this analysis is to determine whether the local imbalance between the zonal pressure gradient and the turbulent stress divergence at and below the core of the Undercurrent can be accounted for by the redistribution of momentum by the 20-30 day waves.

The vertical shear of the Undercurrent may help set the scale for the decay of turbulent dissipation and hence the downward penetration of stress exerted by the surface winds. The dissipation profile appears to be related to the Richardson number profile which depends more critically on the velocity

shear than the density shear below the mixed layer, (figure 5.3, from Toole et al., 1987). Near the surface where the zonal velocity shear is high, Richardson numbers near and below 0.25 are observed where largest dissipation is observed. Conversely, within the velocity core where the shear is negligible, high Richardson numbers and lower dissipation rates are observed. The velocity maximum of the EUC may control the penetration of turbulent dissipation, at least the dissipation which results from turbulence generated by shear instability. A recent equatorial one-dimensional 'bulk' mixed layer model predicts this result (Schudlich and Price, 1990). The mixed layer model incorporates the effect of entrainment mixing at the base of the mixed layer using a threshold condition of the bulk Richardson number, and uses a threshold condition on the gradient Richardson number to include the effect of shear instability. Below the the base of the 'bulk' mixed layer, there is a transition region where downward mixing of momentum penetrates deeper at night due to low values of the gradient Richardson number. Thus this model predicts the observed diurnal cycle of shallow daytime dissipation and deep nighttime dissipation. The turbulent dissipation penetrates no deeper than the EUC core in the model. The advection of zonal momentum by the mean flow is much smaller and in the wrong sense to balance the pressure gradient force, as pointed out by Bryden and Brady in the region of 150°W to 110°W (1985; hereafter referred to as BB1). The remaining terms to consider are the flux divergences of eddy zonal momentum.

To determine from the observations what processes control the dynamical balance of the Undercurrent, an appropriate downstream reference frame is needed. At the depth of the core and below, the Undercurrent nearly conserves potential density and temperature (BB1). From geostrophic zonal velocity profiles determined using mean CTD data, BB1 showed that the Undercurrent flows eastward and upward nearly along the potential temperature surfaces of the upward sloping thermocline from 150°W to 110°W, figure 5.4. In addition, surveys by both Tropic Heat microstructure groups (Chereskin, et al., 1986; Toole, et al., 1987), revealed that the velocity maximum of the Undercurrent at 140°W measured by a ship-mounted ADCP closely tracks a constant potential density surface on time scales of hours to days, figure 5.5. These observations suggest that an appropriate *downstream* coordinate is potential density. Moreover, this reference frame is useful since

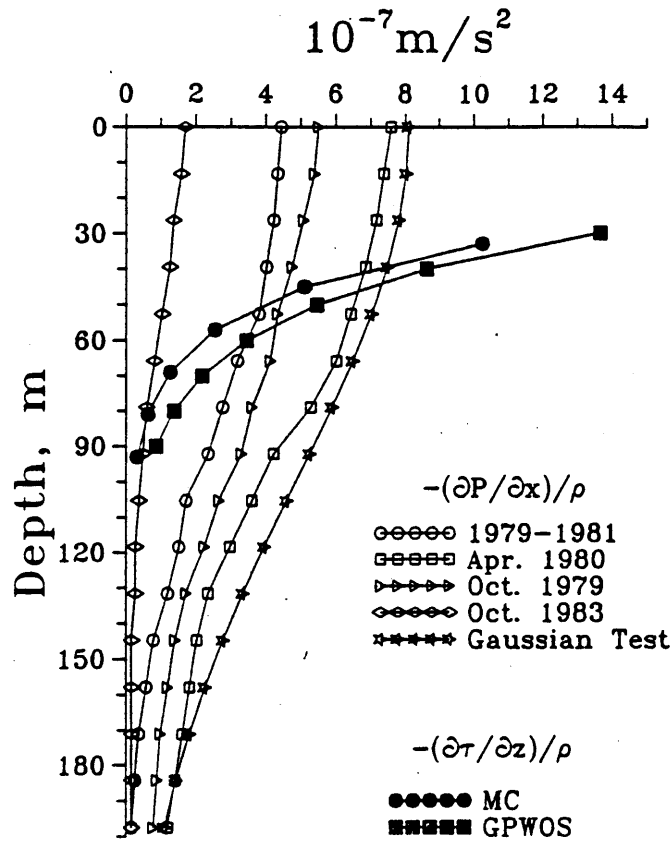


Figure 5.2: This figure shows a comparison of various estimates of the zonal pressure gradient from hydrographic data with two estimates of turbulent dissipation, from Moum and Caldwell, 1985 (MC) and Gregg et al., 1985 (GPWOS). (Figure taken from Dillon et al., 1989)

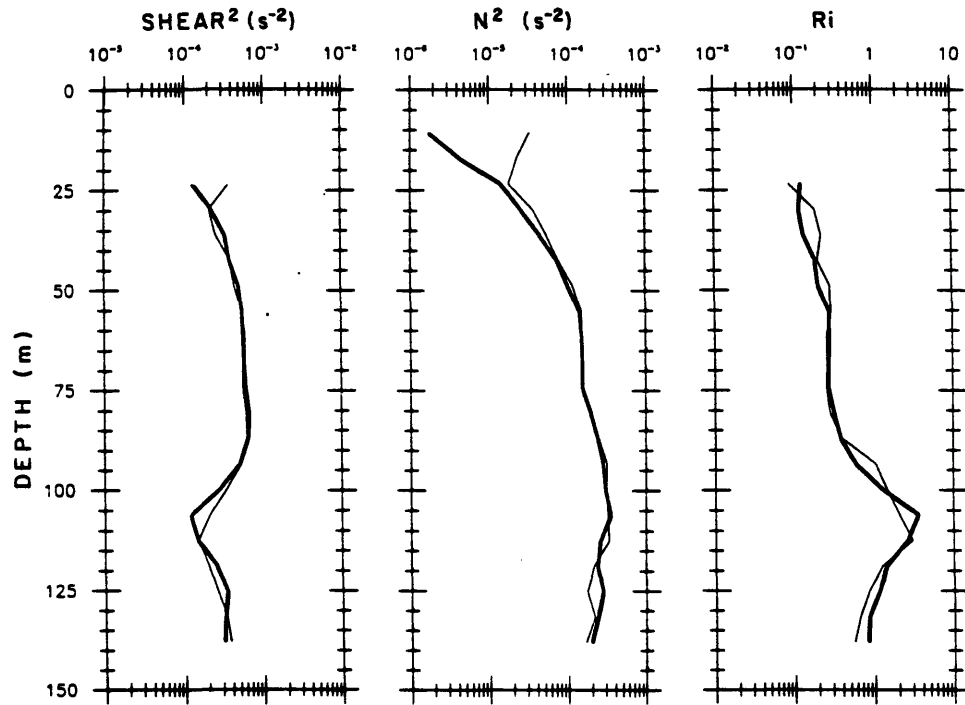


Figure 5.3: Vertical ensemble averaged profiles of total shear squared, Brunt-Vaisala frequency squared and the Richardson number. Measurements were taken aboard the Thomas G. Thompson in November 1984 over 4 and one-half days on the equator at 140°W during Tropic Heat. Shear was measured by ADCP and density data was obtained by AMP (Advanced Microstructure Profiler). (Taken from Toole et al., 1987).

diapycnal transports of heat and momentum can be directly related to mechanisms of forcing and dissipation.

The vertical velocity field associated with the EUC and its relationship to the thermocline, is centrally important to this discussion. Vertical velocity on the equator is large, estimated at $1\text{--}3\text{ m day}^{-1}$, and upward over the domain of the EUC, (figure 5.4 b). Unlike the situation at midlatitudes for basin-scale low-frequency flow, the profile of vertical velocity is well estimated both directly from current meter arrays (Halpern and Freitag, 1987; Bryden and Brady, 1989), and indirectly inferred from drifting buoy statistics (Hansen and Paul, 1987) and diagnostic models (Wyrski, 1981; BB1). Cromwell (1953) first discussed how the wind-driven circulation in the meridional plane gives rise to an upward vertical velocity, which he inferred from the surface distributions of cold water and high productivity observed in a narrow band along the equator. A poleward Ekman transport near the equator in the upper surface layers arises from the prevailing westward winds and the change of sign of the Coriolis parameter. This poleward transport in the surface layers is replenished from below with an upward transport of water derived about equally from a zonal convergence in the upper layers of the EUC and an equatorward convergence due to geostrophic flow from the eastward pressure gradient force (BB1; Brady and Bryden, 1987). Cromwell did not yet know of the existence of the Equatorial Undercurrent. The circulation in the zonal plane due to the Undercurrent is important to this picture because otherwise it appears that the vertical transport is all diapycnal, requiring excessively large buoyancy fluxes to compensate for the upward transport of dense water. By examining the equatorial zonal transport in potential temperature classes and comparing the zonal slope of the potential temperature surfaces to the slope of the zonal-vertical streamlines on the equator, it was found in BB1 that the eastward and upward flow of the EUC was approximately isothermal. The cross-isothermal velocity was less than 20% of the total vertical velocity in the core of the EUC. When integrated in potential temperature, the net transport across isotherms, though small, was shown to be of the appropriate sign and magnitude to balance the net surface heat flux due to exchange with the atmosphere (Brady and Bryden, 1987).

Because the vertical velocity is so large, the dynamical interpretation is complicated. The EUC accomplishes the large upward transport of water

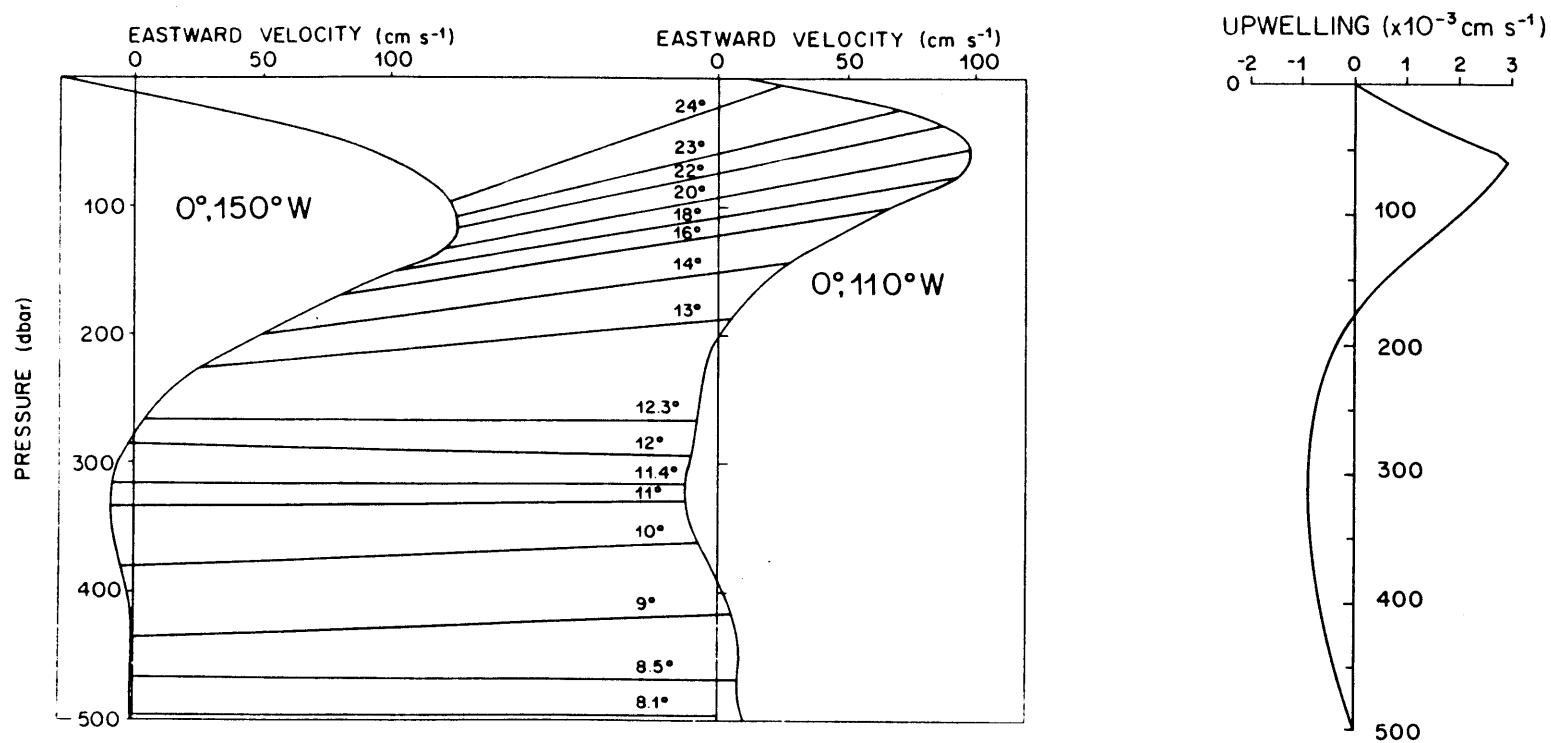


Figure 5.4: Zonal velocity profiles at 150°W and 110°W, and vertical velocity profile from three-dimensional diagnostic model of BB1. Shown on depth axis is the depth at which the given isotherms are found. (Taken from Bryden and Brady, 1985).

necessary for mass conservation as dictated by the divergent Ekman flow, but this upward transport is not associated with a large water mass conversion because most of the upward transport is isothermal. To subtract the kinematic effect of the shoaling EUC, the momentum balance will be examined on potential density surfaces which are approximately the natural downstream coordinates of the EUC. Since parcels exchange properties more readily along potential density surfaces, this is a more appropriate coordinate system to evaluate the relative contributions of lateral and diapycnal mixing processes.

In the downstream isopycnal coordinate system chosen for this analysis, the downstream changes in the Bernoulli Function are examined. In theory, steady large scale mid-latitude flows conserve Bernoulli function along streamlines in the absence of heating or dissipation. *These observations assess the extent to which the conservation of Bernoulli function is dynamically important for equatorial currents.*

The conservation of Bernoulli function, density, and potential vorticity, has been used to model the steady thermocline dynamics of the EUC using a reduced gravity layer model, (Pedlosky, 1987b, 1988; Pedlosky and Samelson, 1989). By connecting the inertial Undercurrent to the extra-equatorial thermocline model of Luyten, et al. (1983), an eastward flow on the equator results with width, depth and velocity scales consistent with observations of the Undercurrent (Pedlosky, 1987b). Furthermore, the original model produces some of the basic features of the equatorial circulation such as shoaling of the thermocline from west to east, and the vertical spreading of the density layers in the meridional plane at the equator. Additions to the original model incorporate the process of diapycnal entrainment into the mixed layer, with a specified entrainment flux (Pedlosky, 1988), and an entrainment flux related to the structure of an imposed wind stress (Pedlosky and Samelson, 1989). These additions address the subjects of the termination at the eastern boundary, and how the Undercurrent is coupled to the directly wind-driven surface layer. In each of the successive improvements to the original model, the Bernoulli function along the equator is no longer constant as it is in the original inviscid model, but instead decreases in proportion to the zonal integral of the entrainment flux.

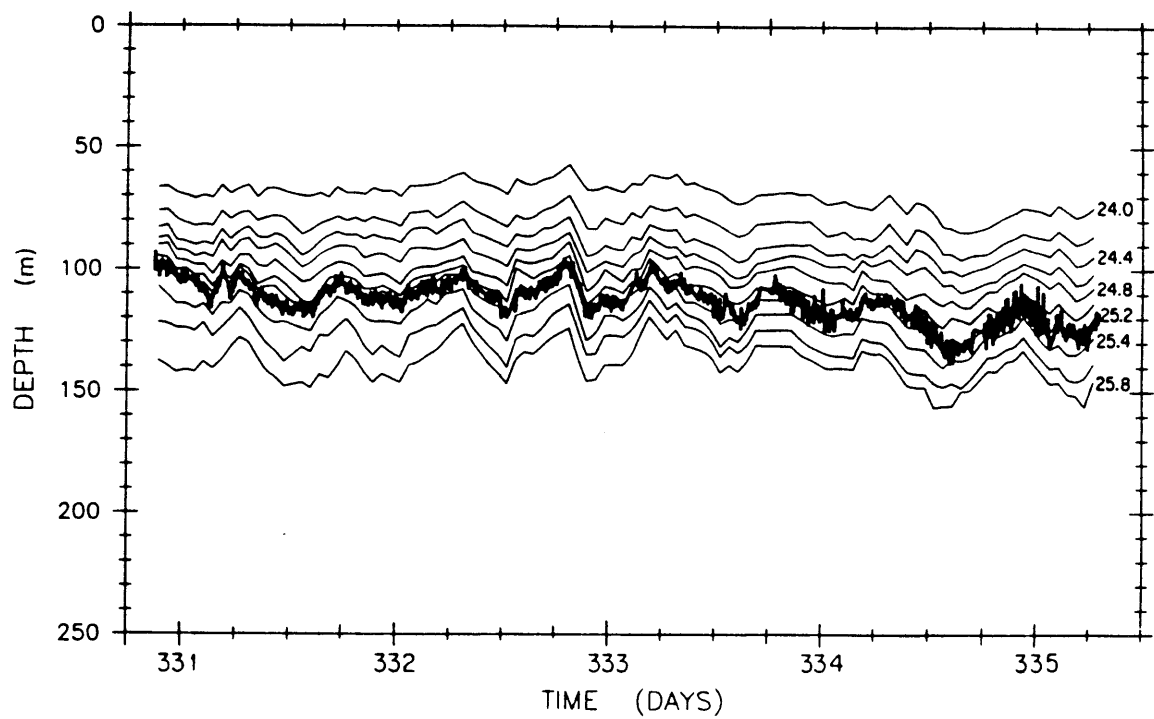


Figure 5.5: Time series of depth of isopycnals, determined from AMP drops, and undercurrent velocity maximum, estimated from ADCP shear data (thick line). (Taken from Toole et al., 1987)

5.2 ISENTROPIC ANALYSIS

Analyzing the patterns of properties along potential density surfaces, called isentropic analysis (Montgomery, 1937). Historically, isentropic analysis has been a very useful descriptive tool in studying the movement of water masses. The origins of water masses are easily interpreted on these surfaces, because water masses with differing properties can meet in juxtaposition adiabatically without mixing (Tsuchiya, 1968). The introduction of the identifying property of a particular water mass can be traced to the intersection of the isentropic surface with the sea surface in the hypothetical absence of cross-isentropic mixing. In 1937 and 1938, Montgomery pioneered a technique of computing the geostrophic potential along these surfaces, (Montgomery, 1937), and showed how this technique can be applied with an investigation of features of the large scale geostrophic flow in the Atlantic Ocean (Montgomery, 1938). In meteorology, the study of flow patterns along isentropic surfaces (in this case potential temperature surfaces) was widely practiced, being especially useful in the preparation and interpretation of synoptic weather charts (see Eliassen, 1986, for historical review).

Isentropes are surfaces of constant entropy. For a parcel undergoing an adiabatic displacement, entropy is conserved. Formally, potential density surfaces are not exact isentropes because seawater is a multi-component system, and because the density of sea water is a nonlinear function of salinity as well as potential temperature and pressure. When two parcels with the same potential density mix, the final potential density is lower because of the nonlinearity of the equation of state. However, if the potential density is more strongly a function of potential temperature, and if no large along-stream gradients of salinity exist, as is the case here in the near surface waters of the equatorial ocean, and for relatively small changes in pressure (less than 500 dbars associated with the Undercurrent) then these surfaces can be used as isentropes to a very good approximation (Montgomery, 1938). In the atmosphere, the moisture content (specific humidity) of the air is the analogue to salinity in the ocean, with potential temperature surfaces acting as isentropes only when the exchange of specific humidity between parcels of air is negligible and unimportant to the application.

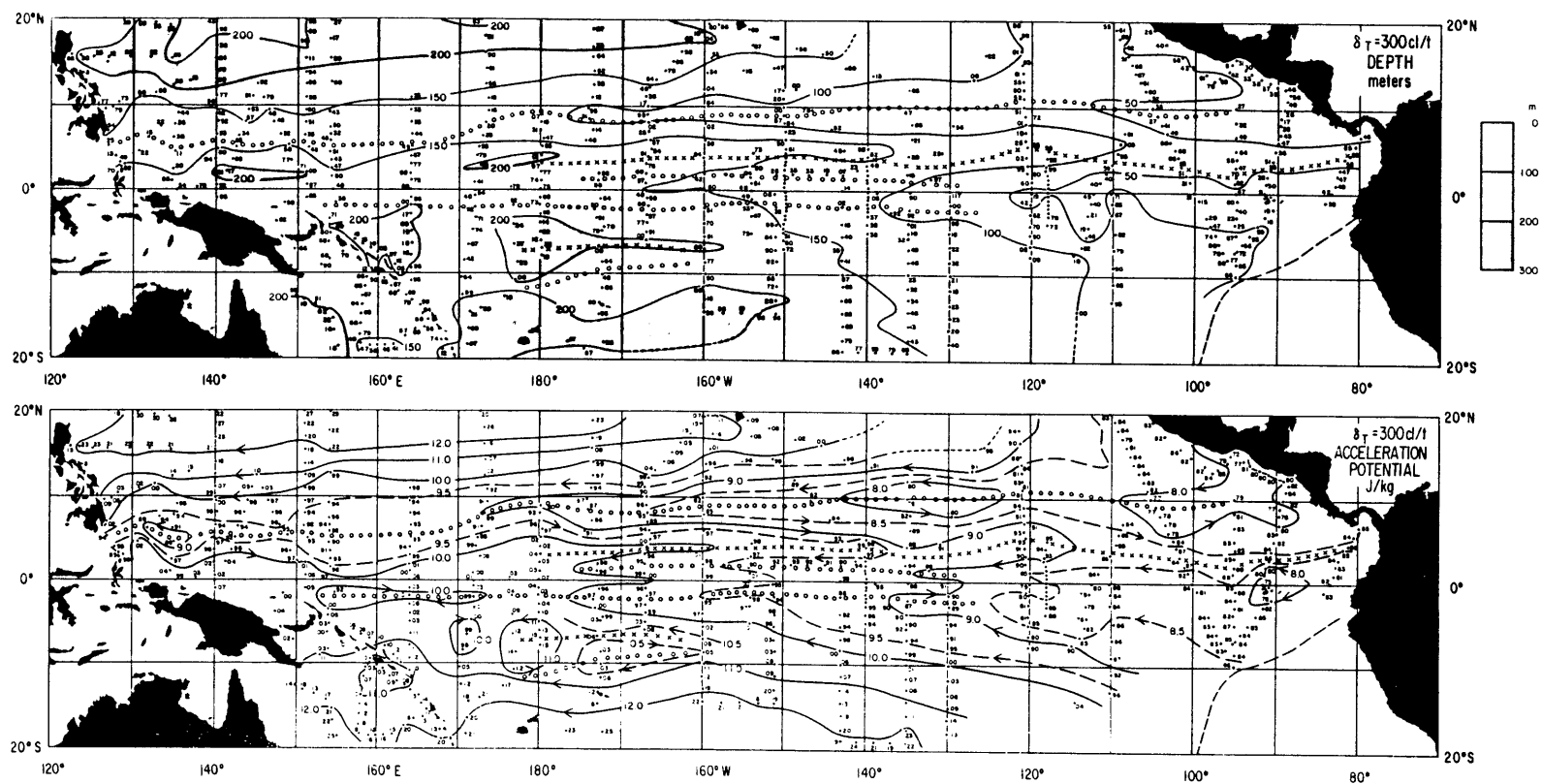
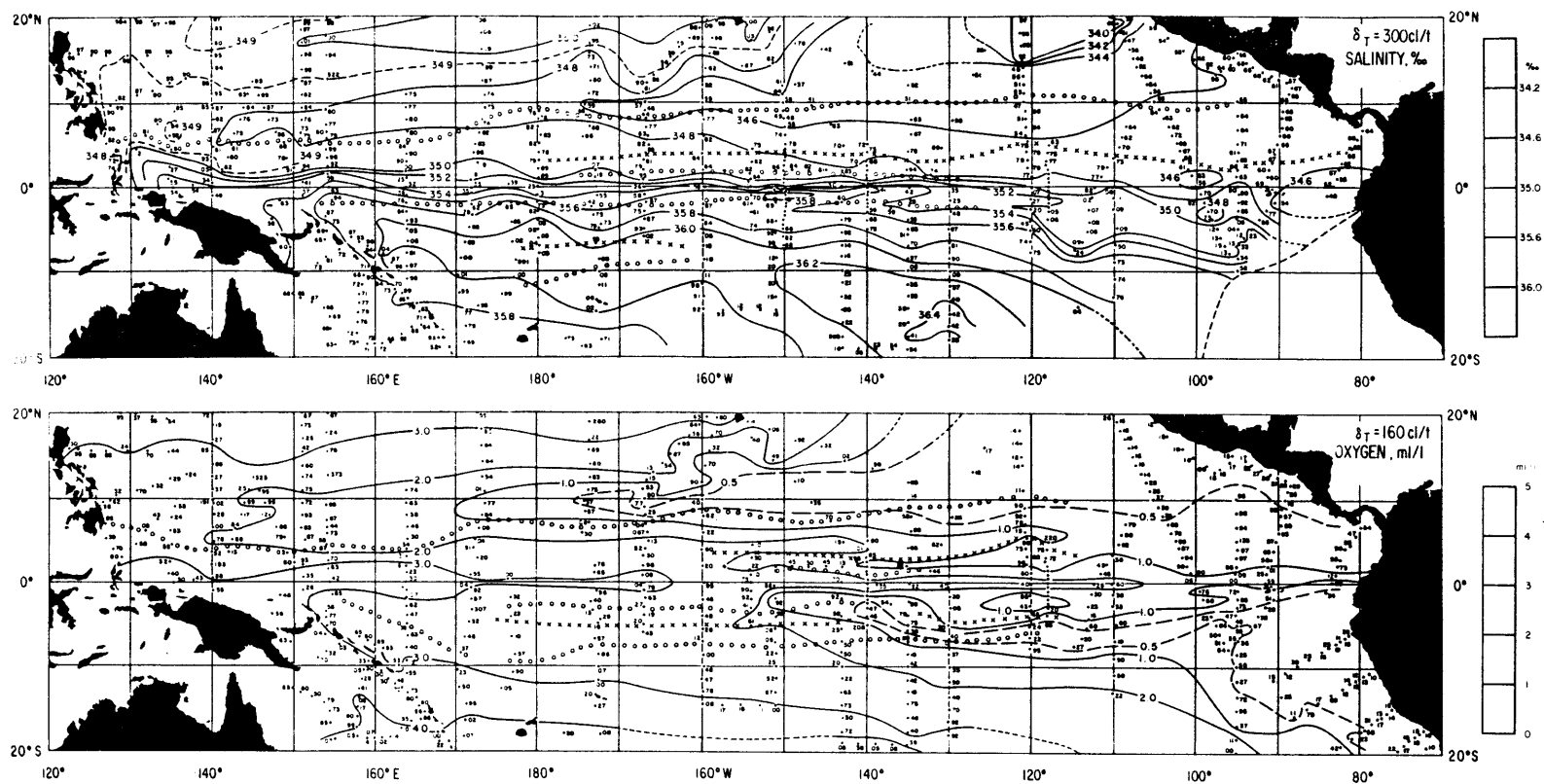


Figure 5.6: Maps of depth of the 300 cl/t surface (a), and Acceleration Potential on the 300 cl/t surface relative to 500dbars (b), Salinity on the 300 cl/t surface and (d) oxygen on the 160 cl/t surface, over the tropical Pacific ocean from 20°N to 20°S. (Taken from Tsuchiya, 1968).



Casting the dynamics into isentropic coordinates, greatly enhances interpretation. For instance, Ertel's potential vorticity in pressure coordinates,

$$Q = g \left\{ (f + \zeta_p) \left(-\frac{\partial \theta}{\partial p} \right) + \frac{\partial v}{\partial p} \left(\frac{\partial \theta}{\partial x} \right)_p - \frac{\partial u}{\partial p} \left(\frac{\partial \theta}{\partial y} \right)_p \right\},$$

is more simply written in isentropic coordinates (x, y, θ) ,

$$Q = g \left\{ (f + \zeta_\theta) / \left(-\frac{\partial p}{\partial \theta} \right) \right\},$$

where ζ is the relative vorticity, $(\partial v / \partial x - \partial u / \partial y)$, and the subscripts p or θ denote that the horizontal gradients are taken either holding pressure or potential temperature constant (Eliassen, 1986).

In this chapter, the balance of terms in the downstream momentum balance of the EUC is examined, where the downstream coordinate is potential density. The mean zonal momentum balance in isentropic coordinates at the equator is written,

$$\begin{aligned} w_c \frac{\partial U}{\partial z} + \frac{\partial u'v'}{\partial y} + \frac{\partial u'w_c'}{\partial z} &= -\frac{\partial B}{\partial x} + \frac{\partial \tau}{\partial z} \\ \text{MVF} + \text{HEF} + \text{VEF} &= \text{BG} + \text{TSD} \end{aligned}$$

where MVF is the diapycnal vertical flux of mean zonal momentum, HEF and VEF are the horizontal and vertical eddy flux divergences of eastward momentum, BG is the downstream gradient in the Bernoulli function, and TSD is the turbulent stress divergence. The horizontal mean velocities, U , and V are in the x and y (east and north) direction with horizontal derivatives taken along a constant potential density surface, W_c is the diapycnal mean vertical velocity in the direction z , the direction of maximum gradient of the potential density, the primed velocity components are eddy velocities, τ is the turbulent stress and B is the Bernoulli function. Neglected in this balance are both the mean meridional advection of zonal momentum because both the meridional velocity and the meridional gradient of zonal momentum are small in the core of the EUC on the equator, and the Coriolis torque, $fV - hW$, since f , the Coriolis parameter $2\Omega \sin \theta$, is zero on the equator,

and hW , equal to $2\Omega\cos\theta W$, is two orders of magnitude smaller than the other terms in the balance even though W is large.

The Bernoulli function is written as follows,

$$B = \Psi_M + \frac{1}{2}U^2$$

where Ψ_M is the Montgomery Stream Function or Acceleration Potential for flow along isentropes, and U is the mean zonal velocity. The acceleration potential is the mean field which tells the direction and magnitude of the acceleration a parcel would feel along isentropic surfaces, as the dynamic height field does along isobars. It is calculated on isentropes, as follows,

$$\Psi_M = D + \delta P,$$

where, D is the dynamic height anomaly (dynamic height relative to the dynamic height at a reference level), δ the specific volume anomaly (specific volume relative to a specific volume reference) and P the pressure of the isentropic surface, (Montgomery, 1937).

Examining the momentum balance on isentropes, has proved useful as an application to other problems, such as in determining the depth from which the Mediterranean outflow originates, (Stommel et al., 1973) and is the foundation of hydraulic theory. Because of the jet-like structure of the Undercurrent, it is appropriate to use the foundations of hydraulic theory which is the theory most often applied to jet problems. In equatorial applications, the water mass properties of the equatorial waters have been studied qualitatively on isentropes (isanosteres or constant δ surfaces), with the Acceleration Potential mapped for comparison to property distributions, (Tsuchiya, 1968). These maps (figure 5.6), using all available hydrographic data at that time, indicate the presence of the EUC as a narrow eastward jet in the Acceleration Potential, salinity and oxygen distributions near the equator.

In theory, for large scale mid-latitude flows, far from regions of forcing or dissipation, the Bernoulli function is conserved following streamlines. The observations that the turbulent stress divergence is negligible at the core of the Undercurrent (Dillon et al. 1989), that the mean Undercurrent flows mainly along constant potential temperature surfaces of the equatorial thermocline (BB1), and that the mean zonal velocity is geostrophic (Lukas and Firing, 1984; Hayes, 1982), motivates the approach that the Undercurrent

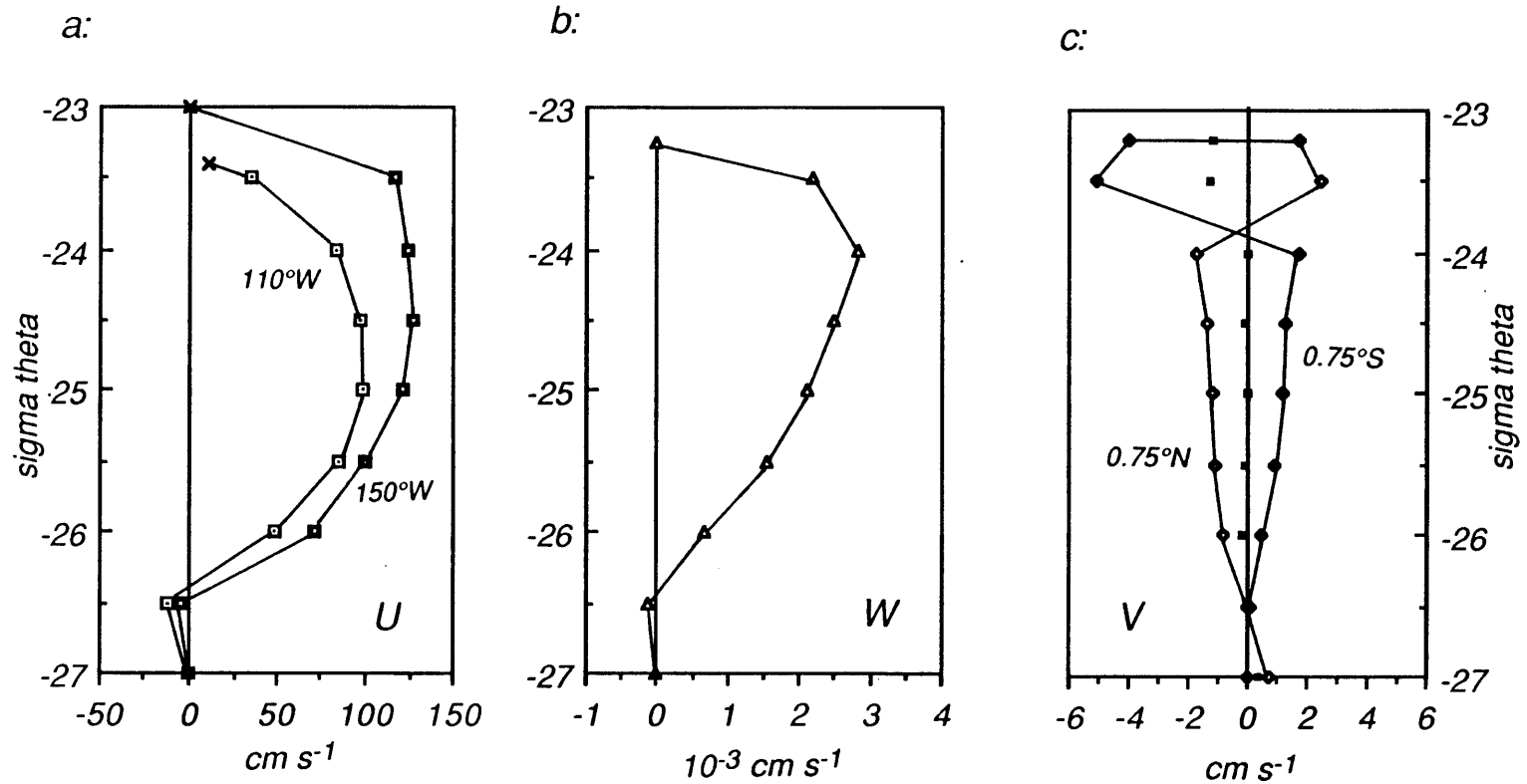


Figure 5.7: Velocity profiles from mean diagnostic model of Bryden and Brady (1985) interpolated to potential density surfaces; (a) Zonal equatorial velocity at 110°W and 150°W , (b) Vertical velocity over entire upwelling zone, (c) Meridional velocity at poleward edges of upwelling zone, $\pm 0.75^\circ$ latitude.

might be modeled as a conservative large scale flow. Theoretical models starting with any or all of the assumptions of conservation of potential density, potential vorticity and Bernoulli Function, have been useful in gaining insight into the dynamics of the Equatorial Undercurrent, (Pedlosky, 1987b; Fofonoff and Montgomery, 1955) and seem to provide an encouraging picture at least qualitatively. Conservation theorems are fundamental precepts for large-scale circulation theory, but as with geostrophy, which is also a first order requirement for such flows, theories based too strictly on such concepts are self-limited. To get at the crux of the dynamics, the next order must be investigated.

5.3 DATA AND METHOD:

Two sets of data are used to investigate the time-averaged downstream momentum balance of the Equatorial Undercurrent. Mean CTD data from the NORPAX Hawaii - to - Tahiti Shuttle Experiment sections at 150°W and the EPOCS sections at 110°W are used to estimate the Bernoulli Function; and velocity and temperature time series measurements from moored EPOCS arrays at 110°W are used to estimate the role of the eddy momentum flux divergences.

The Mean CTD data:

The time mean CTD profiles are derived from casts obtained during the years 1979 - 1981 with the annual cycle removed as described in BB1. The profiles consist of temperature and salinity values every 5 dbars from the surface to 500 dbars, at the equator and every half degree latitude poleward to ±5°latitude, at 110°W and 150°W. The mean profiles of equatorial zonal velocity U, shown in figure 5.7a as a function of potential density, are determined from these CTD data using equatorial geostrophy,

$$\beta U = - \frac{\partial^2 D}{\partial^2 y},$$

with the second derivative approximated using finite differences of dynamic height D, taken over ±1°latitude and the equator. The velocity field was

initially referenced to 500 dbars, the deepest common pressure attained by the CTD. Small barotropic adjustments were made to balance mass over the entire domain, and an ageostrophic velocity component was added to the upper 50 dbars to include the direct effect of the zonal wind stress over the upper mixed layer. A vertical profile of vertical velocity W at the equator, shown in figure 5.7b as a function of potential density, was determined by constraining the flow field to be three-dimensionally conservative within an upwelling zone defined from 0 to 500 dbars, $\pm 0.75^\circ$ latitude, and 150°W to 110°W . Details are found in BB1.

The Montgomery streamfunction or acceleration potential, Ψ_M , is calculated on each isentrope, actually the potential density surface common to both 110°W and 150°W , at each longitude using the method described in Montgomery(1938), given the specific volume anomaly δ , equal to $\alpha - \alpha_0$, where α is the specific volume and α_0 is the reference specific volume equal to $\alpha(T=0^\circ\text{C}, S=35 \text{ psu}, P)$, and P , the pressure in dbars. The dynamic height D , is referenced initially to the dynamic height at 500 dbars, corrected as done in BB1, for the small barotropic adjustments (0.9 dyn cm at 150°W and -0.02 dyn cm at 110°W). The unit chosen for D , B , and Ψ_M is dynamic cm, which is equal to 0.1 J kg^{-1} which appears in some figures; the unit chosen for δ is cl/t (or $10^{-5} \text{ cm}^3 \text{ gm}^{-1}$). All values of U , W , D , δ and P are interpolated linearly in the vertical to the depth of the particular potential density surface. Because the change in δ along a potential density surface from 110 to 150°W is negligible (Table 5.1), and since the calculation of Ψ_M is done with δ held constant along the isentrope, the average δ between 110 and 150°W is used. The error introduced by considering constant potential density surfaces as isentropes is less than one percent, since δ changes by less than 1 percent along all potential density surfaces considered. The Bernoulli function B , is then calculated by adding to Ψ_M , the zonal kinetic energy, $\frac{1}{2} U^2$, calculated from the zonal velocity profile at each longitude. Results are presented in Table 5.1 and discussed in the next section.

The Time Series of Velocity and Temperature at 110°W

The velocity and temperature time series used in this analysis are from a triangular current meter mooring array deployed at 110°W as part of EPOCS

(Freitag et al., 1987; Halpern, 1982). Two moorings are situated 0.5° latitude north and south of the equator, and about 0.5° longitude west of the third, located on the equator. The moorings were instrumented with VACMs and thermistors set at the nominal depths of 20, 50, 75, 100, 150, 200, and 250 meters. The particular records used in the analysis here were chosen because they were the group of longest records that gave the best spatial coverage, in addition to providing observations over the duration of time when Tropical Instability waves are fully developed and most energetic. The records, about 171 days in duration, begin on August 15, 1980 and go to about February 1, 1981. The original hourly sampled records were first low-passed with a one day half-width gaussian filter. Details of the method of analysis are described later.

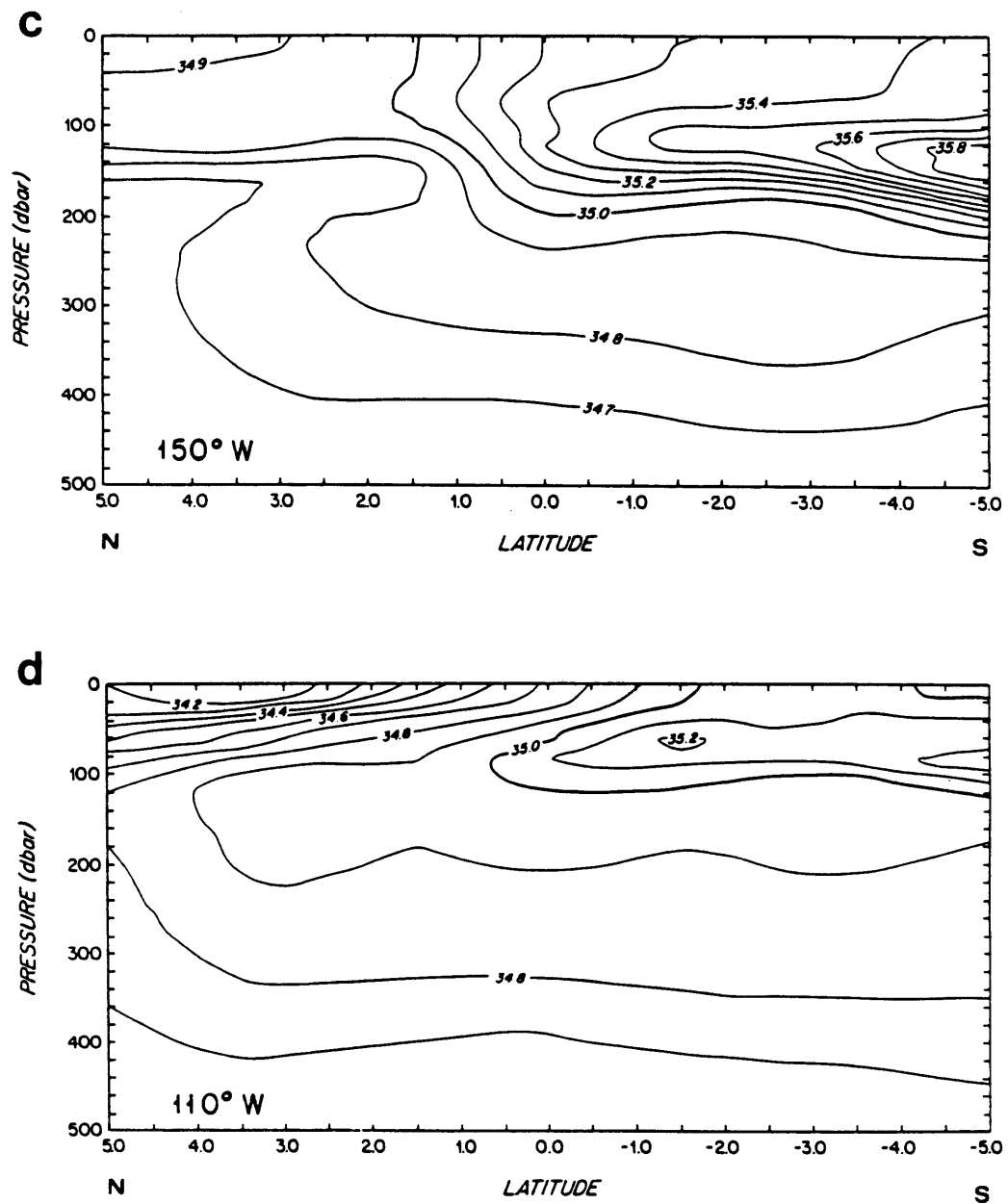


Figure 5.8: Time averaged Salinity sections at 110°W and 150°W from BB1.

Table 5.1: Bernoulli Function Analysis

σ_θ	θ ($^{\circ}\text{C}$)	S (psu)	δ (cl/t)	P (dbars)	D (dyn cm)	Ψ_M (dyn cm)	$\frac{1}{2}U^2$ ($10^3\text{cm}^2\text{s}^2$)	B (dyn cm)	$-\partial B/\partial x$ $10^{-5}\text{cm}^2\text{s}^{-2}$
23.5									
110W	23.80	34.74	437.8	9.2	92.8	96.9	0.6	97.5	
150W	25.23	35.29	441.5	81.9	79.1	115.1	6.8	121.9	5.49
24.0									
110W	22.37	34.85	391.4	32.3	83.2	95.8	3.4	99.3	
150W	23.48	35.27	394.5	102.6	70.4	110.7	7.8	118.5	4.33
24.5									
110W	20.87	34.96	344.3	47.5	77.5	94.0	4.6	98.6	
150W	21.79	35.29	347.3	118.7	64.4	105.4	8.1	113.5	3.36
25.0									
110W	19.09	35.00	297.1	61.5	72.0	90.3	4.9	95.2	
150W	19.75	35.22	300.0	134.3	59.2	99.5	7.5	107.0	2.65
25.5									
110W	17.4	35.10	250.3	85.0	65.6	86.9	3.5	90.4	
150W	17.6	35.19	246.8	152.8	53.6	91.3	4.7	96.0	1.26
26.0									
110W	14.9	34.99	203.4	118.2	59.2	83.2	1.2	84.4	
150W	15.1	35.06	204.8	179.9	48.0	84.9	2.5	87.4	0.68
26.5									
110W	11.86	34.85	160.2	300.8	27.3	75.5	0.1	75.6	
150W	11.85	34.85	160.0	291.8	28.4	75.1	0	75.1	-0.11
27.0									
110W	8.06	34.64	116.3	500.	0.9	59.0	0	59.0	
150W	8.05	34.63	116.5	500.	-0.02	58.2	0	58.2	-0.20

Table 5.1: Bernoulli Function and list of properties needed to calculate Bernoulli Function on potential density from mean CTD data at 150°W and 110°W.

5.4 RESULTS

Water Mass Properties of the EUC core

The particular potential density surfaces, sigma-theta equal to 25.0, 25.5, and 26.0, isolated for this core analysis best correspond to the region of the Undercurrent velocity core (figure 5.4), where it is shown in BB1 that potential temperature is most nearly conserved, in the 20°C to 15°C range. The sigma-theta 25.25 surface was shown by both Tropic Heat microstructure groups, (Chereskin et al., 1986; and Toole et al., 1987), to correspond with the EUC velocity maximum (or core) over the time scale of hours for several days at 140°W in November 1984. In November 1987 at 140°W, the EUC followed the shallower 23.9 sigma theta surface in Tropic Heat II (Hebert et al., 1990).

The salinity maximum also appears to be a good tracer of the EUC core. During Tropic Heat I, the EUC core was observed to track the salinity maximum at the equator reasonably well (Chereskin et al., 1986). This is also characteristic of the EUC in the Atlantic, where the core as defined by the velocity and salinity maxima, was shown to meander about the equator with a period of about 16 days during GATE, (Duing et al., 1976). As Table 5.1 shows for 110°W, the local vertical salinity maximum of 35.10 psu is observed on the 25.5 surface; at 150°W double salinity maxima of 35.30 psu are found at the shallower potential densities of 24.7 and 23.4. The zonally averaged salinity along the 25.5 surface between 110 and 150°W of 35.14 psu is larger than the averages obtained for either the 25.0 or 26.0 surface. The zonally averaged zonal velocity is also greatest on this surface. The salinity maximum is a result of the penetration equatorward of the South Pacific Subtropical Subsurface Water formed in the central waters of the subtropical gyre of the South Pacific, (Tsuchiya, 1968). The equatorward penetrating saline tongue is observed in both salinity sections at 150°W and 110°W, figure 5.8.

In the downstream direction from 150 to 110°W, the potential temperature on the 25.5 and 26.0 surfaces decreases by about 0.2 °C, and the salinity decreases by only 0.1 psu. A larger decrease of 0.7°C in potential temperature is observed along the 25.0 surface.

Table 5.2: The Undercurrent core properties

(a)

σ_θ	location	Z(m)	U(cm s ⁻¹)	$\theta(^{\circ}\text{C})$	W(cm s ⁻¹)
25.0	110W	61.5	98.5	19.1	
	150W	134.3	121.0	19.8	
	average	97.9	109.7	19.4	2.12×10^{-3}
25.5	110W	85.0	84.1	17.4	
	150W	152.8	99.7	17.6	
	average	118.9	91.9	17.5	1.53×10^{-3}
26.0	110W	118.2	48.2	14.9	
	150W	179.9	70.9	15.1	
	average	149.0	59.5	15.0	0.67×10^{-3}

(b)

σ_θ	slope(σ_θ) ($\times 10^{-5}$)	W/U ($\times 10^{-5}$)	W_a (10^{-3}cm s^{-1})	W_c (10^{-3}cm s^{-1})
25.0	1.64	1.93	1.80	0.32
25.5	1.52	1.66	1.40	0.13
26.0	1.39	1.13	0.83	-0.16

Table 5.2: Properties of the Undercurrent core (a); and (b) a comparison of the slope of potential density surfaces to the slope of streamlines of flow on the equator, listed with the isopycnal and diapycnal vertical velocities of each potential density surface within the Undercurrent core.

Conservation of Potential Density within the Core

The conservative nature of the Undercurrent core is investigated using two complementary approaches. First, the local balance in the conservation equation for potential density can be diagnosed by comparing the relative slopes of streamlines to the potential density surface slopes. Flow which conserves a quantity will flow parallel to constant surfaces of that quantity. Second, a volume transport budget can be examined over the layers defined by the surfaces of potential density. These two approaches are somewhat independent at the equator. Because the meridional velocity is zero at the equator and the local meridional slope of isopycnals is very small, the local balance at the equator only involves the balance in the vertical-zonal plane. However considering a volume spanning the equator and extending meridionally, the meridional convergence must be taken into account.

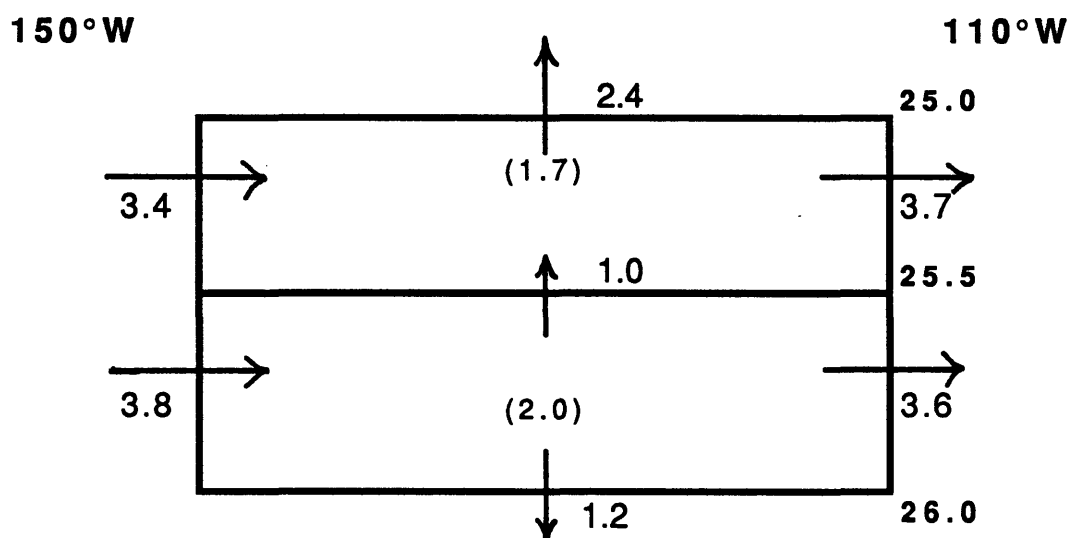
The local balance in the equation of the conservation of potential density is considered in Tables 5.2a and b. Table 5.2a lists the depth, zonal geostrophic velocity, potential temperature, and salinity of each potential density surface, found by linear interpolation at each location, with the averages between locations along the same potential density surface. The vertical velocity listed is relative to the Cartesian frame, as calculated in BB1, and interpolated to the average depth of each surface. For each potential temperature, Table 5.2b compares the zonal slope of the surface, calculated from the difference in the depth over the upstream and downstream location, with the slope of the streamline in the zonal-vertical plane calculated from the ratio of the vertical to zonal velocity. The error estimated for the slope of the streamline is $\pm 0.2 \times 10^{-5}$, arising from error primarily in the estimate of W , which is assumed to be 15%. Error in the slope of potential density surfaces is estimated to be $\pm 0.1 \times 10^{-5}$. The slope error of a property is mainly associated with error in the vertical interpolation of the data. It is assumed that the error in the estimate of the vertical difference in the locations of the potential density surfaces between each longitude is at most 3.5m ($\sqrt{2} \times 2.5$ m) considering that the fields so heavily averaged in time are very smooth in the vertical. As was shown in BB1 with potential temperature, it appears that within this core region of the Undercurrent potential density is nearly conserved since given the estimated errors, streamlines are parallel to potential density surfaces.

In the second approach, consider the transport budget within a volume bounded above and below by the particular potential density surfaces chosen above, and laterally at $\pm 0.75^\circ$ latitude and 110°W to 150°W . This approach best illustrates some features of the quasi-conservative nature of the upwelling Undercurrent flow. This budget uses velocities determined in BB1 from the constraint that the flow, integrated over every volume incremented in depth by 5 dbars with the same lateral boundaries, is three-dimensionally non-divergent. This constraint must hold regardless of what volume is chosen subsequently as long as the new volume lies within the original volume. Thus in what follows, the meridional transport is both inferred as a residual of the directly calculated downstream and cross-isopycnal divergences, and calculated directly from the meridional velocity field at the north and south edges integrated over the thickness of the density layers averaged between each longitude.

The volume transport budget within the sigma-theta 25.0 to 25.5 and 25.5 to 26.0 layers is shown schematically in figure 5.9. In both layers, the downstream along-isopycnal transport is nearly non-divergent along the equator; about as much water of this density enters zonally at 150°W as leaves at 110°W . A net zonal export of $0.3 \times 10^6 \text{ m}^3 \text{ s}^{-1}$ is observed at 110°W in the 25.0 to 25.5 range which is an order of magnitude smaller than the total average transport within this range of about $3.5 \times 10^6 \text{ m}^3 \text{ s}^{-1}$. In the sigma-theta 25.5 to 26 range, there is a net import of only $0.2 \times 10^6 \text{ m}^3 \text{ s}^{-1}$ which is also small compared to the average along-isopycnal transport of $3.7 \times 10^6 \text{ m}^3 \text{ s}^{-1}$ in this layer. Thus, even though the zonal or along-isopycnal velocity in the core of the Undercurrent decreases downstream, the along-isopycnal transport is nearly constant because the thickness of the isopycnal layers increases in the downstream direction. In the 25.0 - 25.5 volume the thickness increases downstream from 18.5 m at 150°W to 23.5 at 110°W , and likewise in the 25.5 to 26.0 range from 27.1 m to 33.2 m.

Although the vertical diapycnal velocities are 15 to 20% the size of the vertical velocity within this density range, the associated diapycnal transport divergence is nevertheless quite large compared to the along-isopycnal downstream divergence because the small velocities are integrated over such a large area. Errors in Cartesian vertical velocity of 10 to 15%, heavily influence the following results for diapycnal transport estimates because the

a: The Zonal-Vertical Plane



b: The Vertical-Meridional Plane

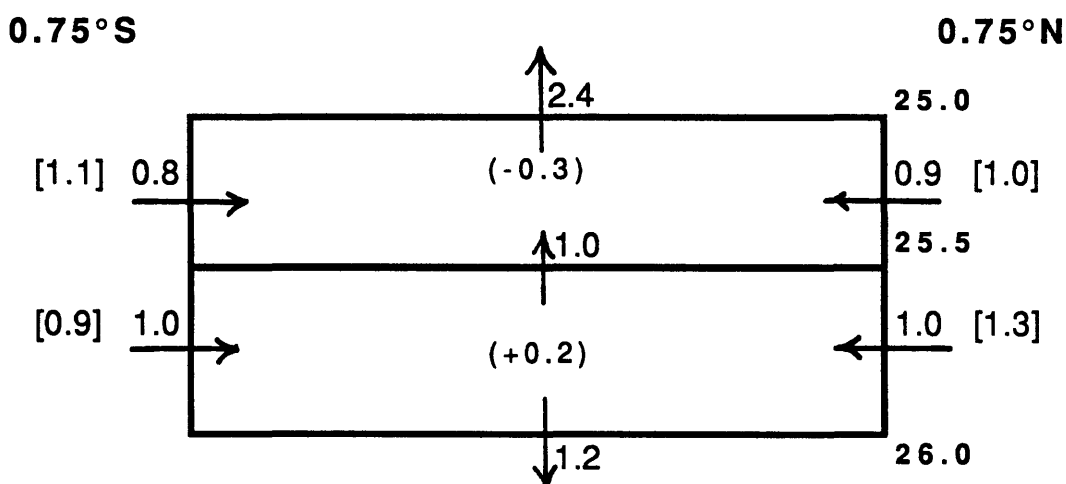
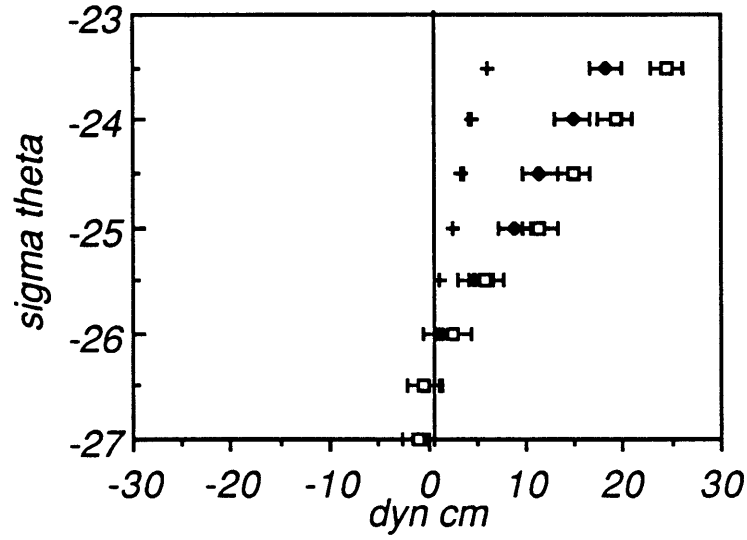


Figure 5.9 A schematic of the transport budget of the Undercurrent core layers. The transport budget in (a) the zonal-vertical plane, where the horizontal arrows denote the zonal transports along potential density layers, the vertical arrows denote the vertical transport across the potential density layers, and the numbers in parentheses are the residual needed from the meridional edges to balance the volume transport; and (b) the meridional-vertical plane, where the horizontal arrows denote the meridional transport at the poleward edges of the layers with the numbers in brackets from the integration of the meridional velocity profile over the mean layer depth, and the unbracketed numbers from the residual of the zonal and vertical transport divergence; the vertical arrow denote the vertical transport with the figures in parentheses denoting the zonal convergence in the layers.

diapycnal velocities are of the same order as the errors in W . This produces an error in diapycnal transport of nearly $1 \times 10^6 \text{ m}^3 \text{ s}^{-1}$. Across the 25.0 sigma-theta surface, there is an upward diapycnal transport of $2.4(\pm 1) \times 10^6 \text{ m}^3 \text{ s}^{-1}$ and upward across the 25.5 surface, $1.0 (\pm 1) \times 10^6 \text{ m}^3 \text{ s}^{-1}$, making a net vertical divergence of $1.4 (\pm 1.4) \times 10^6 \text{ m}^3 \text{ s}^{-1}$. Similarly a net vertical divergence of $2.2 (\pm 1.4) \times 10^6 \text{ m}^3 \text{ s}^{-1}$ is obtained for the 25.5 to 26 range, with a downward transport across the 26.0 surface of $1.2 (\pm 1) \times 10^6 \text{ m}^3 \text{ s}^{-1}$. For this entire core region, the total divergence is $3.6 (\pm 1.4) \times 10^6 \text{ m}^3 \text{ s}^{-1}$. Closing the volume transport budget is easily accomplished with a net convergence by small ($\sim 0.01 \text{ m s}^{-1}$) equatorward flows at the northern and southern edges of the upwelling zone. The depth-averaged meridional velocities from the diagnostic model, presented in figure 5.7c, are small, and of the order of 0.01 m s^{-1} satisfying the volume transport closure. In the 25 to 25.5 layer, equatorward transports of about $1 \times 10^6 \text{ m}^3 \text{ s}^{-1}$ result from integrating the meridional velocity field at $\pm 0.75^\circ$ latitude. A net meridional convergence of $2 \times 10^6 \text{ m}^3 \text{ s}^{-1}$ obtains. In the 25.5 to 26.0 layer, equatorward transports of 1.3 and $0.9 \times 10^6 \text{ m}^3 \text{ s}^{-1}$ are obtained for the north and south edges respectively yielding a net meridional convergence of $2.2 \times 10^6 \text{ m}^3 \text{ s}^{-1}$. These directly estimated meridional transport convergences compare well to those required to close the budget and compensate for the net zonal-vertical divergence of $1.7 \times 10^6 \text{ m}^3 \text{ s}^{-1}$ for the 25.0 to 25.5 layer and $2.0 \times 10^6 \text{ m}^3 \text{ s}^{-1}$ for the 25.5 to 26.0 layer. Since these two ways of closing the transport budget agree so well, within $0.3 \times 10^6 \text{ m}^3 \text{ s}^{-1}$, it suggests that the errors associated with the diapycnal vertical velocity may be overestimated. The diapycnal transports may be known to better than $1 \times 10^6 \text{ m}^3 \text{ s}^{-1}$. The implications for the water mass conversions implied by these diapycnal velocities are discussed later.

These two approaches seem to build a picture of the EUC as a jet which flows upward and eastward along potential density surfaces, that also possesses a secondary circulation, nevertheless important to its dynamics and thermodynamics. This secondary circulation is similar to the traditional meridional-vertical circulation cells at the equator with meridional convergence producing upwelling above the core of the EUC and downwelling below.

(a)



(b)

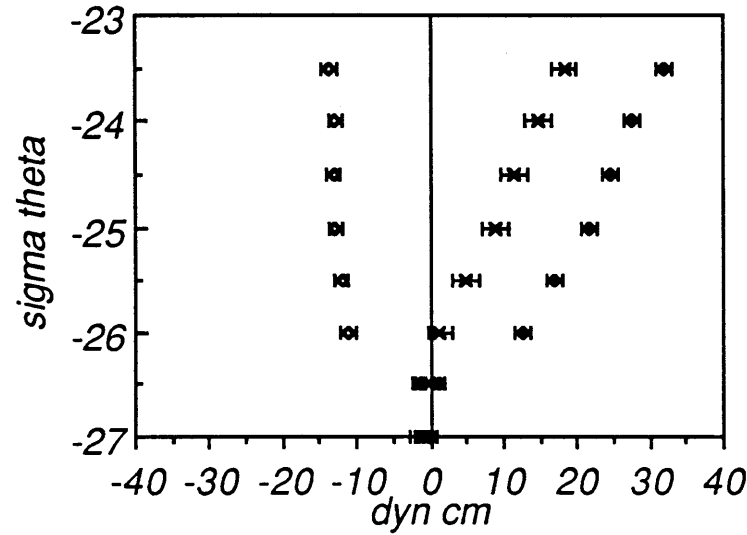


Figure 5.10: Breakdown of (a) the downstream change in the Bernoulli "head", denoted by the open squares, where the head needed to balance the kinetic energy decrease is denoted by the crosses, and the change in the Acceleration Potential is denoted by the solid diamonds; and (b) the Acceleration Potential, denoted by the x's, which is the sum of the downstream decrease in dynamic height, the open diamonds, and the downstream increase in δP , the solid diamonds. Size of the errors is indicated by the bars on the points.

The Downstream Change in Bernoulli Function

A similar approach is taken to investigate the momentum balance of the core of the Undercurrent. The last column of Table 5.1 lists the downstream gradient of the Bernoulli function along isopycnals. The vertical profile obtained (figure 5.11) has a similar shape and magnitude compared with the zonal pressure gradient force profile with depth (figure 5.2). It appears to decay linearly with potential density from a near surface value of $5.5 \times 10^{-5} \text{ cm}^2 \text{ s}^{-2}$, to half that value or less in the core layers defined above. Within the core, these values provide a significant accelerative force due to the Bernoulli gradient. Broken into components, as shown in figures 5.10a and b, the change in Bernoulli function represents the enhancing effects of the accelerative downstream changes due to the increasing Acceleration Potential Ψ_M , and loss of Zonal Kinetic Energy, which by comparison is much smaller though larger than the estimated errors shown by the bars in the figures. Errors associated in Dynamic Height are taken to be 1 dyn cm, which is the estimated rms error in surface dynamic height relative to 500 dbars corresponding to high-frequency internal waves Hayes (1982). Using an error in the estimate of the downstream change of the pressure of the potential density surface of 3.5 m, yields an error in Acceleration Potential of about 1.4 dyn cm. Together these estimates, listed in table 5.3, yield an error in the downstream change of the Bernoulli head of about 1.7 dyn cm, which gives an error in the corresponding downstream gradient of B of $0.3 \times 10^{-5} \text{ cm}^2 \text{ s}^{-2}$. Thus even on the potential density surfaces defining the core, the downstream gradient of B is significantly eastward.

The effect of the upward diapycnal advection of zonal momentum, $W_c \frac{\partial U}{\partial z}$, appears to make a small contribution to the momentum balance, as figure 5.10 indicates, especially in the core layers where W_c is small and uncertainly known. Assuming that the error of uncertainty in W_c is $\pm 0.15 \times 10^{-3} \text{ cm s}^{-1}$, yields an error in this term of about $0.15 \times 10^{-5} \text{ cm}^2 \text{ s}^{-2}$. Thus, in the upper potential density layers, this term, though still small compared with the downstream Bernoulli gradient, is significant and contributes to accelerate an eastward flow.

Table 5.4 compares the local slopes of the actual streamlines relative to the slopes of the potential density surfaces given by W_c/U at the equator, and

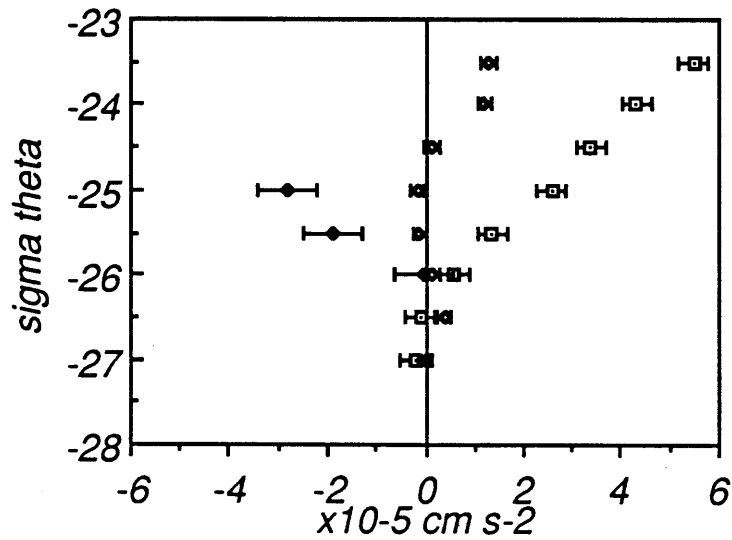


Figure 5.11: A profile versus potential density of the terms estimated in the zonal momentum balance. The open squares denote the estimate of the down-stream gradient of Bernoulli Function, the open diamonds represent the estimated transport of momentum by the diapycnal vertical velocity, and the solid diamonds are the estimated divergence of the northward flux of eastward momentum accomplished by the 20 day wave band. The estimated errors are indicated by the error bars.

the local slope of the Bernoulli function and Acceleration Potential as calculated by $-\frac{\partial B/\partial x}{\partial B/\partial z}$ and $-\frac{\partial \Psi_M/\partial x}{\partial \Psi_M/\partial z}$ locally relative to the potential density surfaces. After considering the errors in the estimate of each slope as listed in Table 5.3, it is clear that the slope of the streamline compares well with the local slope of the Bernoulli function and the Acceleration Potential in the defined core layers, better than with the slope of the potential density surfaces relative to which it is calculated. Surfaces of constant B rise more steeply across potential density surfaces than streamlines, within this region of the core.

The Effect of the Eddy Reynolds Stress Divergences

One purpose of examining the momentum balance on isentropic or potential density surfaces is to compare the effects of different terms estimated using a variety of data, at different locations. If an Undercurrent core -relative frame can be identified by using potential density surfaces, then comparison is made easier. For instance, closing the momentum budget ideally using the pressure gradient from 150 to 110°W, requires estimates of eddy Reynolds stress divergence terms at the mean longitude, 130°W. But if it is assumed that the momentum balance of the EUC core does not change drastically from 150°W to 110°W relative to potential density surfaces, the eddy Reynolds stress divergence terms estimated at 110°W, can be used if estimates can be determined relative to potential density surfaces.

The current meter array at 110°W does not measure potential density, but as an approximation, the fluxes are computed on surfaces of constant temperature. In the upper waters of the equator for depths shallower than 250 m, the difference between temperature and potential temperature is minor. It is shown in Table 5.1, that the potential temperature did not change by a large amount on the potential density surfaces defining the core layers. The largest downstream change observed was 0.7°C on the 25.0 sigma theta surface, at an average potential temperature of 19.4°C. This introduces an error in the analysis which can be estimated by comparing fluxes calculated on the 19 and 19.4°C surfaces. At the 25.5 and 26.0 sigma theta surfaces the downstream change in temperature was much smaller at about 0.2°C. The error in using the average potential temperature surface is probably well

Table 5.3: Errors

U	10 cm s ⁻¹
W _c	0.2 x 10 ⁻³ cm s ⁻¹
W	0.2 x 10 ⁻³ cm s ⁻¹
D	1 dyn cm
dz, dP	3.5m, 3.5 dbars
$\partial B/\partial x$	0.3 x 10 ⁻⁵ cm s ⁻²
$\partial u'v'/\partial y$	0.6 x 10 ⁻⁵ cm s ⁻²
zonal slopes: σ_θ	0.1 x 10 ⁻⁵
Ψ_M, B	0.2 x 10 ⁻⁵
W/U	0.2 x 10 ⁻⁵

Table 5.3: Estimates of the errors. Explanation of estimates are found in text.

Table 5.4: Comparison of Slopes Relative to σ_θ Surfaces

σ_θ	W _c /U	$-\frac{(\partial \Psi_M/\partial x)}{(\partial \Psi_M/\partial z)}$	$-\frac{(\partial B/\partial x)}{(\partial B/\partial z)}$	$\frac{\partial z}{\partial x} \sigma_\theta$
23.5	1.2	3.3	5.1	1.6
24.0	1.1	1.9	4.1	1.6
24.5	0.6	0.9	1.3	1.6
25.0	0.3	0.7	0.7	1.6
25.5	0.1	0.4	0.4	1.5
26.0	-0.3	0.3	0.4	1.4
26.5	-0.9	-0.2	-0.1	-0.2
27.0	0	0	0	0
	(x 10 ⁻⁵)	(x 10 ⁻⁵)	(x 10 ⁻⁵)	(x 10 ⁻⁵)

Table 5.4: A comparison of the slopes of the streamline, surfaces of constant Acceleration Potential, and Bernoulli Function, relative to potential density surfaces.

within other larger errors in the estimate. To compare the downstream gradient in Bernoulli function to the eddy Reynolds stress estimates at 110°W, the fluxes of momentum are estimated on the constant isotherms, 19.4, 17.5, and 15.0°C.

New time series are constructed of zonal and meridional velocity on isotherms, and depth of the isotherms, from the time series of velocity and temperature at fixed depths. The new time series generated from the series at the equatorial mooring of the array, is shown in figure 5.12. Most notable in the time series of meridional velocity and depth of isotherms, are the fluctuations at regular periods of about 20 to 30 days, which are most dramatic on the 19.4 and 17.5 °C isotherms. These are associated with the Tropical Instability Waves (Philander, et al., 1984). Fluctuations at shorter periods are more noticeable on the 15°C surface. These fluctuations are superimposed upon an intraseasonal variability noted by the slow general upward motion of the isotherms except for a single sharp drop in October. At the time of the drop, an anomalously large eastward pulse is noted on the 17.5°C surface. Perhaps this is a wind forced Kelvin wave passing the mooring location (Knox and Halpern, 1982). The 19.4 °C surface intersects the sea surface preceding the sharp drop, invalidating the assumption that this surface is quasi-conservative. A large pulse of westward flow is noted at this time at the surface most likely reflecting the presence of the South Equatorial Current. The new time series generated at the north and south moorings are similar in character to the equatorial series.

Spectral analysis was performed on a 168 day piece of the record to obtain a frequency band at central period of 21 days. To get adequate statistical confidence, 7 frequency bands were averaged together ranging in period from 33.6 to 15.3 days. This frequency band-averaging provided 14 degrees of freedom and a significant coherence at 95% confidence of 0.66.

Table 5.5 presents the estimates of the northward flux of eastward momentum for the 21 day band for the array listed with the coherence and phase. It is noted that the phase is close to 90 degrees for the records which are significant at 95% confidence. All but one of the records, the eddy flux on the 17.5°C isotherm south of the equator, are significant at this level. The fluxes north of the equator on the 17.5 and 19.4°C isotherms are northward and south of the equator are southward indicating a poleward net divergence

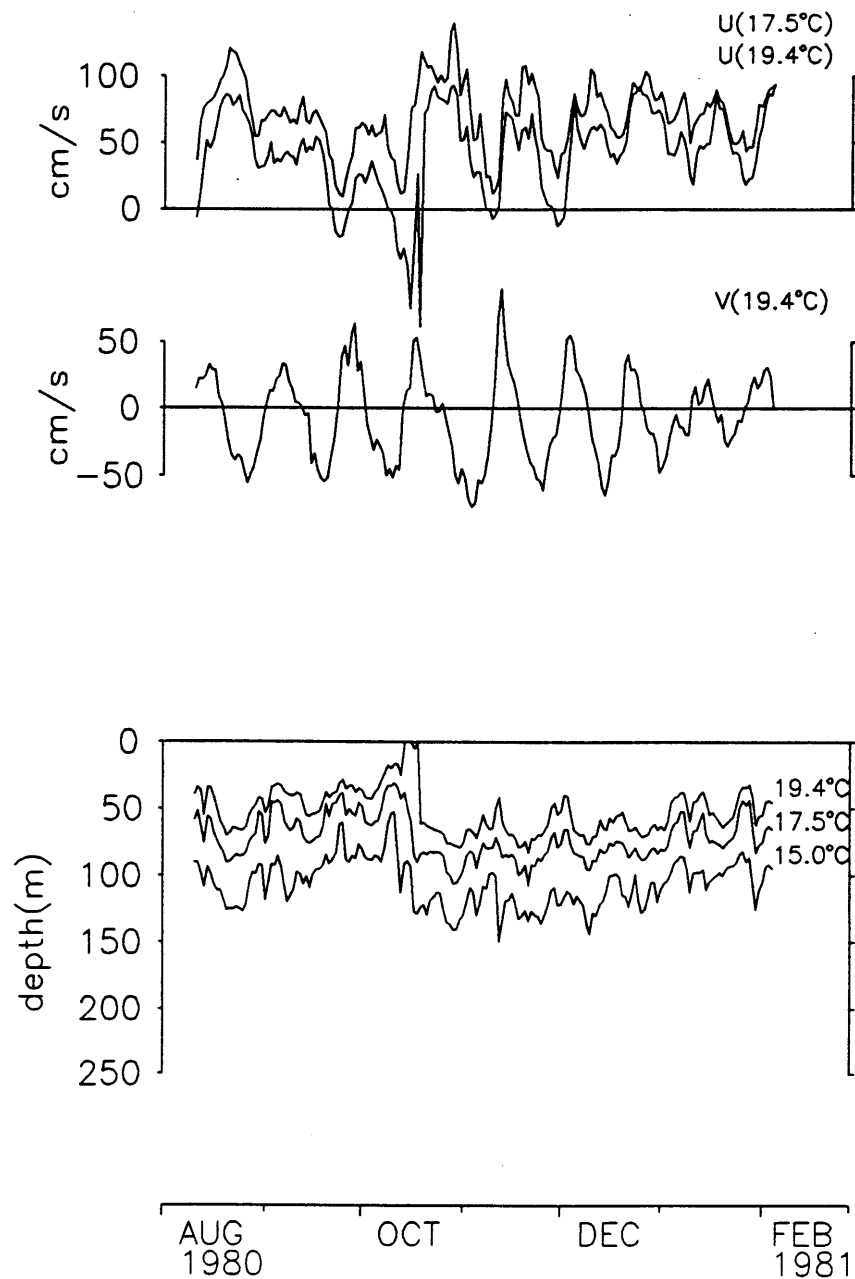


Figure 5.12: New timeseries of velocity on isotherms and depth of isotherms calculated from the equatorial mooring T8, where (a) show the zonal velocity on the 19.4 and 17.5 $^{\circ}\text{C}$ isotherms, (b) shows the meridional velocity on the 17.5 $^{\circ}\text{C}$ isotherm, and (c) shows the depth of the 19.4, 17.5 and 15.0 $^{\circ}\text{C}$ isotherms.

of eastward momentum at these isotherms. At 15°C, there is a small poleward divergence although the fluxes are all directed to the south. The flux divergence of this northward flux of eastward momentum is compared to the downstream change on the Bernoulli function, in figure 5.11.

An error at the 19.5°C isotherm is estimated by comparing the flux divergence estimated by interpolating to the 19°C instead. Using 19.5°C, a flux divergence of $2.8 \times 10^{-5} \text{ cm}^2\text{s}^{-1}$ is obtained whereas at 19°C, a flux divergence of $2.2 \times 10^{-5} \text{ cm}^2\text{s}^{-1}$ is obtained. This is only one type of error encountered in this type of estimate, but the difference, $0.6 \times 10^{-5} \text{ cm}^2\text{s}^{-1}$ is taken as an indication of the error throughout the calculation. While it is difficult to estimate the other errors, errors due to the assumption of conservation of temperature, especially for the warmer values, and errors in interpolating over such large instrument placements in the vertical (25 to 50 m) are probably the largest source. It is hoped that these errors are no larger than the estimate of the error above, thus, it is used as an estimate throughout the array.

As revealed in figure 5.11, the profiles of eddy Reynolds stress divergence and the downstream gradient of Bernoulli function compare well in magnitude and shape. A local balance is suggested given the errors of the estimates for the core region of the Undercurrent.

5.5 DISCUSSION

That the transport budget for this volume defined by sigma theta surfaces requires a meridional flow at the poleward edges to balance the diapycnal transport, may seem to question the assumption that the Undercurrent conserves potential density along the equatorial route without the added information that the vertical velocity due to the upward motion along isopycnals is much larger than the diapycnal velocity within the core. Consideration of the advective timescales, however, suggests that the water which exits across the potential density layers vertically is replaced by these meridionally converging flows. A parcel at 150°W in the core of the Undercurrent with a potential density of 25.5, will reach 110°W after 60 days, before it can leave the volume through diapycnal exchange which will take approximately 100 days. However, a parcel travelling toward the equator

Table 5.5: Northward Flux of Eastward Momentum on Isotherms

T (°C)	N	E	S
19.4	282 (0.89, 67)	77 (0.89, 82)	- 7 (0.59, 92)
17.5	126 (0.85, 70)	- 2 2 (0.87, 94)	- 6 8 (0.47, -166)
15.0	- 1 6 (0.92, 95)	- 4 9 (0.84, 122)	- 2 1 (0.78, -106)

Table 5.5: Cospectrum of zonal and meridional velocity in the 21 day band (33.6 to 15 days) at each isotherm 19.4, 17.5 and 15.0°C, listed with the coherence and phase. The significant coherence at 95% confidence is 0.63.

in the layer above (or below) the 25.5 surface from the poleward edges of the volume also reaches the equator after 100 days. Actually, this parcel will undergo a water mass conversion along the equatorward route, in effect being slowly upwelled (or downwelled) relative to the Undercurrent core, such that by the time it reaches the equator the conversion is completed and it is in a new density layer.

The resulting picture evokes the simple Undercurrent-upwelling model elucidated by Wyrski (1981) except that the vertical boundaries of the upwelling volume are isopycnals, the vertical motion is relative to the upwelling of the Undercurrent core, which now explicitly reveals the water mass conversion required in each cell.

The amount of water entering meridionally below the core that needs to be made more dense is nearly equal to the amount of water entering meridionally above the core that needs to be made less dense. The 2.4 Sv of 25.0 to 25.5 water must be converted to water less dense than 25.0; and likewise the 1.2 Sv of 25.5 to 26.0 must be converted to water that is more dense. However, to accomplish the net conversion little buoyancy flux divergence over the two layers is actually needed compared with the amount of buoyancy flux needed to accomplish each conversion separately. Either a downward diffusive buoyancy flux across the sigma-theta 25.5 surface and no fluxes across the 25 and 26 surfaces is required, or at both sigma-theta 25 and 26 surfaces, the fluxes can be upward and nearly equal, and zero at the 25.5 surface, in order to be consistent with having relatively little net buoyancy flux divergence over the combined two layers. The first possibility suggests that the core is more strongly diffusive than the regions above and below, since the vertical eddy flux of buoyancy required is large. This situation is rather unlikely because it requires an up-gradient buoyancy flux, with less dense water releasing buoyancy to the denser water making it more dense to allow it to sink. The second case requires no buoyancy exchange between layers at the core but large exchanges above and below the core. This case is more physically likely even though it means that the 25.5 to 26 water must be made denser (colder). The upper layer can easily be made less dense (warmer) by a turbulent downward diffusion of buoyancy (heat) from the surface boundary layer. At the equator, it is observed that the surface waters are heated by net air-sea interaction. It is more difficult to see how the lower

layer can be made more dense (colder) at the equator. The evidence to support the possibility of this water mass conversion comes from the existence of the 13°C thermostat.

The 13°C thermostat is found along the entire Pacific in the deep thermocline layers below the Undercurrent, (Stroup, 1960; Tsuchiya, 1975). It is a layer of well-mixed (minimum N^2) water of about 13°C, and salinity of about 34.9 psu, associated often with a westward deep flow and laterally by large equatorward gradients in temperature and salinity which support geostrophically what are known as the Subsurface Equatorial Countercurrents. The observed downstream change in its properties of the thermostat are consistent with exchange with the lower layers of the Undercurrent. Downstream (eastward) the thermostat becomes more well-mixed, warmer, saltier, and larger in cross-sectional area. Thus it seems possible that the lower layers of the Undercurrent exchange buoyancy and salinity with the thermostat perhaps through diffusive or diapycnal fluxes, subtly changing the properties downstream. North and south of the thermostat, the water is colder and fresher. These lateral gradients make it seem unlikely that the thermostat changes eastward by lateral mixing. Lateral mixing would accomplish a change in properties to the west with the thermostat becoming colder and fresher to the west if the source waters were in the east. The observation that it becomes more well-mixed to the east, implies that the exchange must be with the lower layers of the Undercurrent. Exchange with the lower layers of the EUC is also suggested by the high oxygen tongue extending across the Pacific from the western boundary along the 200 and 160 cl/t surfaces which approximately bound the thermostat (figure 5.6, as discussed by Tsuchiya, 1968). In any given meridional section the oxygen contours form troughs at the equator with higher values towards the EUC core. The troughs of oxygen contours are steeper than the troughs of isentropic surfaces resulting in an oxygen maximum on the isentropic surfaces. High oxygen is noted along the western boundary in the southern hemisphere, suggesting that the source waters for the thermostat have southern hemisphere origin. Modification can then occur along the equator within the EUC as the high oxygen waters are carried eastward within the lower layers of the EUC.

On Closing the Momentum Balance at the Core of the Undercurrent

Results presented here suggest that there exists a balance in the downstream momentum balance of the core of the Undercurrent between the downstream change in Bernoulli function and the lateral divergence of eddy Reynolds stress. The Reynolds stress acts as an equivalent westward stress divergence which counteracts the eastward force of the downstream Bernoulli gradient. On the other hand, it is shown that the actual streamlines within the eastward and upward flowing Undercurrent core are about as parallel to locally calculated Bernoulli surfaces as they are to local surfaces of potential density. It seems that an equivalent statement can be accepted about the core of the Undercurrent nearly conserving its Bernoulli Function as is accepted about it nearly conserving its potential density.

An estimate of the dissipation required for the flow within the Undercurrent to cross surfaces of Bernoulli Function illustrates this idea that the Undercurrent nearly conserves Bernoulli function. The conservation of Bernoulli function is actually a statement of energy conservation,

$$U \frac{\partial B}{\partial x} + W_c \frac{\partial B}{\partial z} = -\epsilon.$$

The dissipation rate ϵ is calculated as a residual between the mean advection terms. At the 25.5 sigma theta surface, a dissipation rate of $0.8 (\pm 0.7) \times 10^{-7} \text{m}^2 \text{s}^{-3}$, positive and just barely larger than the error, obtains. Similar dissipation rates are estimated at all potential density surfaces of the core region. The two terms tend to cancel and each is of the same order by comparison. That the dissipation required is small suggests that the Bernoulli function is also a quasi-conserved property of the Undercurrent. However, as in the difference between geostrophy and quasi-geostrophy, it is noted that the important clues to the dynamics are uncovered by considering the second order effects. Here it is found that the wave fluxes have an important role in the dynamical balance of the mean Undercurrent.

5.6 CONCLUSIONS

A classic approach to investigating the dynamics of the Equatorial Undercurrent has been re-examined. Wyrтки and Bennett (1963) analyzed the energy balance of the core of the Undercurrent on an isentropic surface ($\delta=280$ cl/ton) by balancing the observed downstream decrease in the Acceleration potential about equally in the eastern Pacific, with increases of mean kinetic energy and dissipation by vertical friction. Here, the momentum balance is better closed by new observations. It appears that vertical friction of the type that Wyrтки envisioned, that due to turbulence generated by the winds, has been shown both directly by microstructure observations and here indirectly, to be not very important at the depths of the core of the Undercurrent. Instead, significant momentum flux divergences of the large scale equatorial waves play a large role. Hence it appears that it is lateral rather than vertical friction that decelerates the EUC. The residual between the downstream decrease in the Bernoulli function and the wave flux divergence is small and of the same order as the error in the estimates.

Analysis of the volume transport budget within the core layers has given a refined view of the circulation within the Undercurrent core. It appears that there exists a secondary circulation where the meridional convergence is balanced by a diapycnal divergence within isopycnal layers while the zonal transport along isopycnals is conserved. Meridional geostrophic flows, which converge on the core of the Undercurrent, are slow enough that as they flow equatorward they are slowly converted to warmer water above the core and thermostad water below the core.

Recent observational studies by Tropic Heat investigators have provided new insights into the time dependent behavior of the Undercurrent. Hebert and colleagues have suggested from the analysis of along- and cross-equatorial transects of the velocity and density structure with the RSVP (Rapid Sampling Vertical Profiler) and ship-mounted Acoustic Doppler profiles that the Undercurrent velocity maximum closely follows a particular potential density surface as well as the local salinity maximum on timescales of hours to days at a particular location, but over longer times and with comparisons over longer distances, the maxima track different potential density surfaces (Hebert et al., 1990). The maximum velocity of the Undercurrent profile is expected at the location where the turbulent stress

divergence becomes negligible and the eddy stress divergence begins to balance the eastward pressure gradient. Thus, the depth of the EUC maximum appears to be dependent on the local vertical penetration of turbulent stress divergence which probably depends on local factors such as the local vertical shear of the Undercurrent, and the strength of the local winds and buoyancy fluxes. These factors may vary over time and longitude so that comparing the zonal and long term variations of the density of the velocity maximum may not be appropriate. What is more appropriate is comparing the acceleration potential on potential density surfaces as is done here.

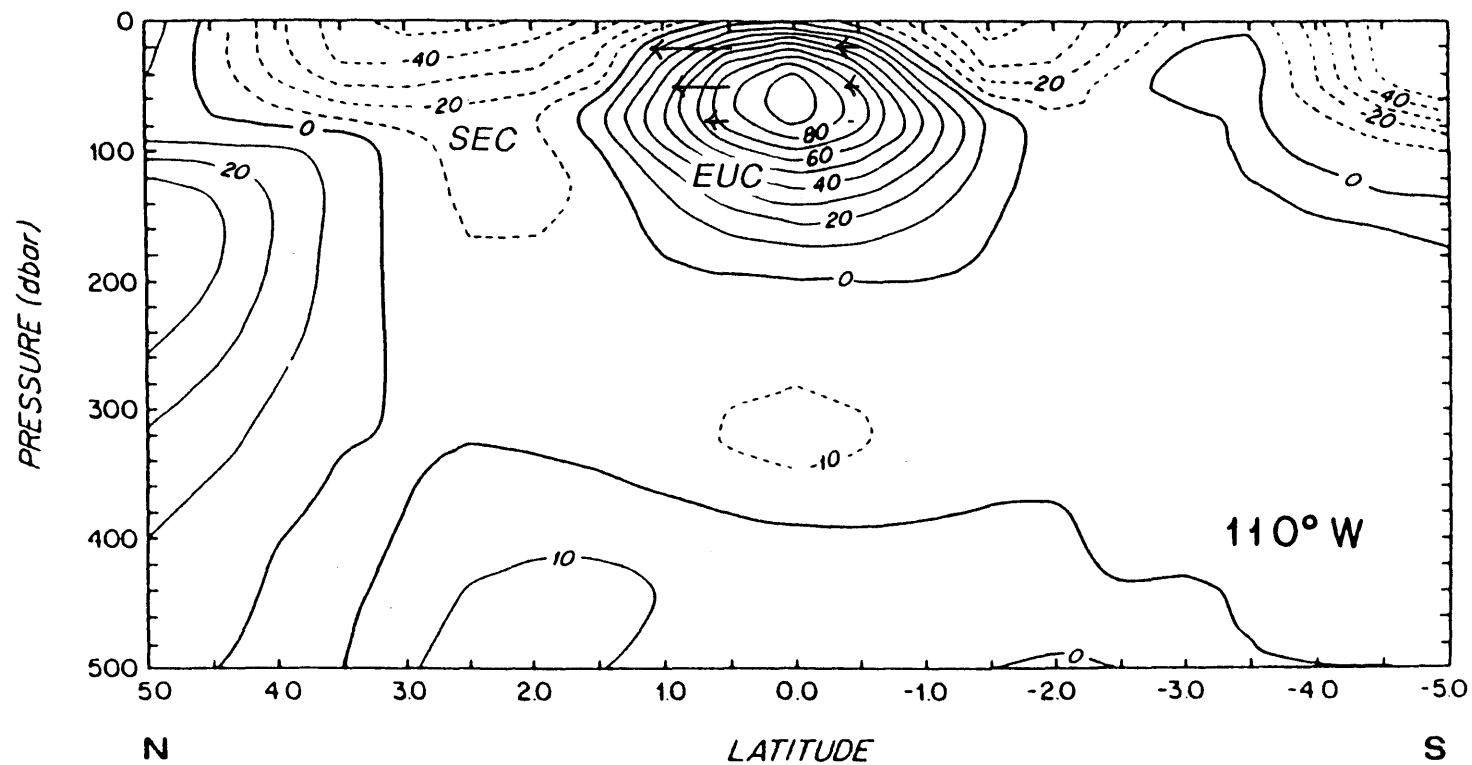


Figure 6.0: Meridional section of zonal geostrophic velocity across the equator at 110°W from Bryden and Brady, 1985. Arrows representing the northward flux of eastward momentum produced by the waves in the 14.2 to 36.8 day band are drawn at the depths of the current meter instruments at the northern and southern mooring.

CHAPTER 6:

Summary and Final Remarks

6.1 SUMMARY

The EPOCS array of velocity and temperature time-series at 110°W is analyzed to study the 14.2 to 36.8 day oscillations in the eastern Pacific Ocean and their effect on the dynamics of the mean Equatorial Undercurrent. These surface intensified waves propagate westward along the equatorial upwelling front as first observed in satellite images of SST. The variance of the meridional velocity is mainly contained in a narrow frequency band (24 to 17.3 days), with a central period of 21 days, as exhibited in spectra obtained using a 312 day long record at 20 m depth. Phase differences between horizontally separated meridional velocity time series, calculated for a wider band (periods from 36.8 to 14.2 days with a central period of 20.4 days) using a 184 day piece of the record during which the oscillations are most energetic, show westward phase propagation at a speed of $0.9 \pm 0.3 \text{ m s}^{-1}$, with a zonal wavelength of 1660 km. Negligible meridional phase propagation is indicated. In the vertical, deeper records lead shallower records for all record pairs except the 20 m record (which is located within the upper boundary layer) and the 50 m record. This upward phase propagation can be interpreted as downward energy propagation for equatorial waves. Fitting the observed vertical phase differences to the WKB approximation of the vertical structure equation, yields an estimate for the separation constant c of $1.2 \pm 0.3 \text{ m s}^{-1}$ (or an equivalent depth of 15 cm). For such a value of c , the observed wavenumber-frequency point lies on the dispersion curve for the mixed Rossby-gravity wave mode within the estimated errors. While the observed propagation characteristics suggest that linear equatorial wave theory may be applicable at least qualitatively, other aspects such as the ability of the waves to transport significant amounts of momentum and heat suggest that a fully

nonlinear theory capable of encompassing interactions with both other wave modes as well as complicated mean flow structures is necessary.

Large and coherent eddy fluxes of momentum and temperature are observed within the array at 110°W. The spatial distribution of the co- and quadrature-spectra of these fluxes in the 21 day band (36.8 to 14.2 days) is used to estimate the interaction terms in the mean zonal momentum and energy equations in Chapters 3, 4, and 5.

The mean zonal velocity field, U , is in thermal wind balance with the mean temperature field, T in the upper part of the array. It appears that the array adequately resolves the zonal velocity field of the Undercurrent, the maximum of which is observed at 75 m at the southern location. The mean meridional velocity field, V , is divergent over the depth range of 75 m and above, and convergent below. The mean vertical velocity at the equator is estimated using the mean heat balance yielding upward velocities at 100 m and above, and a maximum of $2.6 \times 10^{-3} \text{ cm s}^{-1}$ at 75 m, the depth of the Undercurrent core. The mean velocity field associated with the mean Undercurrent compares well with established estimates at the same location and over the same time period.

The distribution of the northward eddy flux of eastward momentum, $u'v'$ in the 21 day band, is divergent over the upper half of the array (at 100 m depth and above) with a much smaller and less coherent convergence below to 250 m. This is indicative of an eastward stress divergence above 100 m and an eastward stress convergence below. Integrating to 125 m, a westward equivalent stress of $-0.3 \text{ dynes cm}^{-2}$ is obtained. Thus over the entire depth range of the array, as well as to only 125 m, the eddy motions in this band act as an effective westward stress on the mean eastward flowing Undercurrent through the vertically integrated meridional Reynolds stress divergence (MRSD).

The other potentially important eddy momentum flux, uw , is estimated from an assumed eddy heat balance. The vertical flux of eastward momentum by the eddy wave band, is upward over the region of the core of the Undercurrent, reaching a maximum at the core. Through the vertical Reynolds stress divergence (VRSD) $-(uw)_z$, the 21 day waves are found to

have an important effect in the zonal momentum balance of the Undercurrent core. The resulting vertical profile of uw exhibits convergence above the core of the mean Undercurrent, located at 75 m, and divergence below the core with a similar magnitude. Such a profile suggests no net acceleration of the Undercurrent core but over time this distribution of stress divergence acting alone would produce an apparent upward displacement of the Undercurrent core. To 250 m, the vertical integral of the VRSD acts as a negligible eastward stress of $0.04 \text{ dynes cm}^{-2}$. Integrated to the core (75 m) however, the vertical integral of the VRSD yields an eastward stress of $0.15 \text{ dynes cm}^{-2}$. When compared to the westward stress of about $-0.3 \text{ dynes cm}^{-2}$ obtained from integrating the MRSD to the core, a tendency for partial compensation of the two RSD terms is inferred above the core.

Profiles of the combined effect of these two eddy stress divergences are compared with the eastward zonal pressure gradient force. Above the core, the RSD nearly cancel, leaving the eastward pressure gradient force largely unbalanced by this wave stress. It is hypothesized that the turbulent stress divergence must balance the pressure gradient above the core. Below the core, the RSD combine nearly to balance the eastward zonal pressure gradient mainly through the VRSD.

With the inferred mean vertical velocity estimate, the mean inertial acceleration terms are estimated and appear, when added together, to be small effect overall at $-.09 \text{ dynes cm}^{-2}$, though individually the terms are as large as the RSD terms. The mean meridional advection of mean zonal momentum nearly cancels the mean vertical advection of the mean zonal momentum. The errors are large in these terms.

The Eliassen-Palm formulation for the mean zonal momentum equation is utilized to obtain a clearer picture of the role of the 21 day eddies in the dynamics of the Undercurrent. The estimates of the streamline for the eddy-driven meridional-vertical circulation, vT/T_z suggest a consistently southward and upward mean eddy-driven circulation pattern for the entire array. This eddy-driven circulation is in the direction to partially compensate for the mean meridional and vertical inertial acceleration terms. The overall size of the eddy-induced circulation, however, is much smaller than the observed v and w fields.

The EP flux divergence is a measure of the role of the eddies in redistributing momentum in the mean zonal momentum balance. Above the core, to the 50 m level, the EP divergence is very small. In the core region, at the 75 and 100 m levels, there is a divergence of EP flux, suggesting a decelerating mechanism for balancing the eastward zonal pressure gradient at these depths. Integrated to 125 m, the equivalent stress of the EP flux divergence is westward at $-0.10 \text{ dynes cm}^{-2}$ which is reduced over the eddy Reynolds stress divergence estimated equivalent stress over the same region of $-0.22 \text{ dynes cm}^{-2}$. The virtue of using the EP flux divergence rather than the Reynolds stress flux divergence is that all of the direct effects of the eddies in the momentum balance are expressed as the EP flux divergence. In this manner, it is shown that the 21 day eddy band of variability is important to the momentum balance of the Undercurrent, directly through the EP flux divergences and indirectly through the advection of eastward momentum by the eddy-driven mean circulation.

In Chapter 4, the rate of conversion from mean to eddy energy is estimated from the wave fluxes of momentum and temperature in the 21 day band. A local balance is observed between the positive conversion of mean kinetic energy (MKE) to eddy kinetic energy (EKE) through shear production, $-u'v'U_y - v'^2V_y - u'w'U_z$, at $0.4 \times 10^{-3} \text{ cm}^2\text{s}^{-3}$, and the local decay of MKE due to interaction with the eddies, $-(u'v')_yU - (v'^2)_yV - (u'w')_zU$, at $-0.6 \times 10^{-3} \text{ cm}^2\text{s}^{-3}$. An e-folding time scale of growth of 20 days is suggested for the local growth of EKE through the shear production terms, which compares well with theoretical estimates. Near the surface, at the 20 m level, there appears to be a near balance between the large positive rate of conversion usually associated with barotropic instability, $-u'v'U_y$, at $1.5 \times 10^{-3} \text{ cm}^2\text{s}^{-3}$, and the leak poleward of EKE at $-1.8 \times 10^{-3} \text{ cm}^2\text{s}^{-3}$, accomplished by the conversion process involving the mean meridional mass divergence due to poleward Ekman drift. Compared with the kinetic energy conversion, the conversion of mean available potential energy to eddy potential energy, $-v'T'(\alpha T_y/T_z)$, is an order of magnitude smaller at $.04 \times 10^{-3} \text{ cm}^2\text{s}^{-3}$, suggesting that the primary source of eddy energy is through kinetic energy conversion.

Through isentropic analysis, a different approach to studying the zonal momentum and energy balances of the Undercurrent is presented in Chapter

5. The purpose of using this approach is to be able to determine the mean momentum and energy balance of the Undercurrent core in a downstream frame of reference so that kinematical effects can be subtracted. The mean Bernoulli function, defined as the sum of kinetic energy and Acceleration Potential calculated on potential density surfaces or approximate isentropes, is used as the diagnostic for this study.

On potential density surfaces, the Bernoulli function is observed to decrease eastward from 150°W to 110°W. This is mostly due to a decrease in the Montgomery streamfunction or Acceleration Potential. In the mean zonal momentum balance of the Undercurrent, the downstream decrease in the Bernoulli function represents an eastward force that can be balanced by the lateral divergence of eastward eddy stress calculated on isotherms representative of the core of the Undercurrent. This implies that it is not necessary to invoke an enormous turbulent stress divergence to balance the eastward pressure gradient force.

The downstream decrease in the Acceleration potential represents a decrease or a release of mean available potential energy. From an energy balance perspective, the overall decrease observed in the mean Bernoulli function implies that the release of mean available potential energy is not converted into mean kinetic energy but must be balanced by small scale processes, such as turbulent dissipation or conversion into eddy kinetic or potential energy. The rate at which mean available potential energy is released as the Undercurrent flows "downhill", is about $10^{-3} \text{ cm}^2 \text{ s}^{-3}$, which is about the rate at which mean kinetic energy is converted to eddy kinetic energy for the 21 day waves through lateral shear instability as estimated in Chapter 4.

Within the core of the Undercurrent, the local slopes of the eastward and upward mean equatorial trajectories, are larger than the slopes of the isopycnals but smaller than the slopes of Bernoulli function. But the slopes of the Bernoulli function and the mean streamline are nearly equal to the slope of the isopycnals within the errors of the calculation. Thus to a good approximation, it can be said that the Undercurrent *nearly* conserves Bernoulli function and density as it flows eastward and upward.

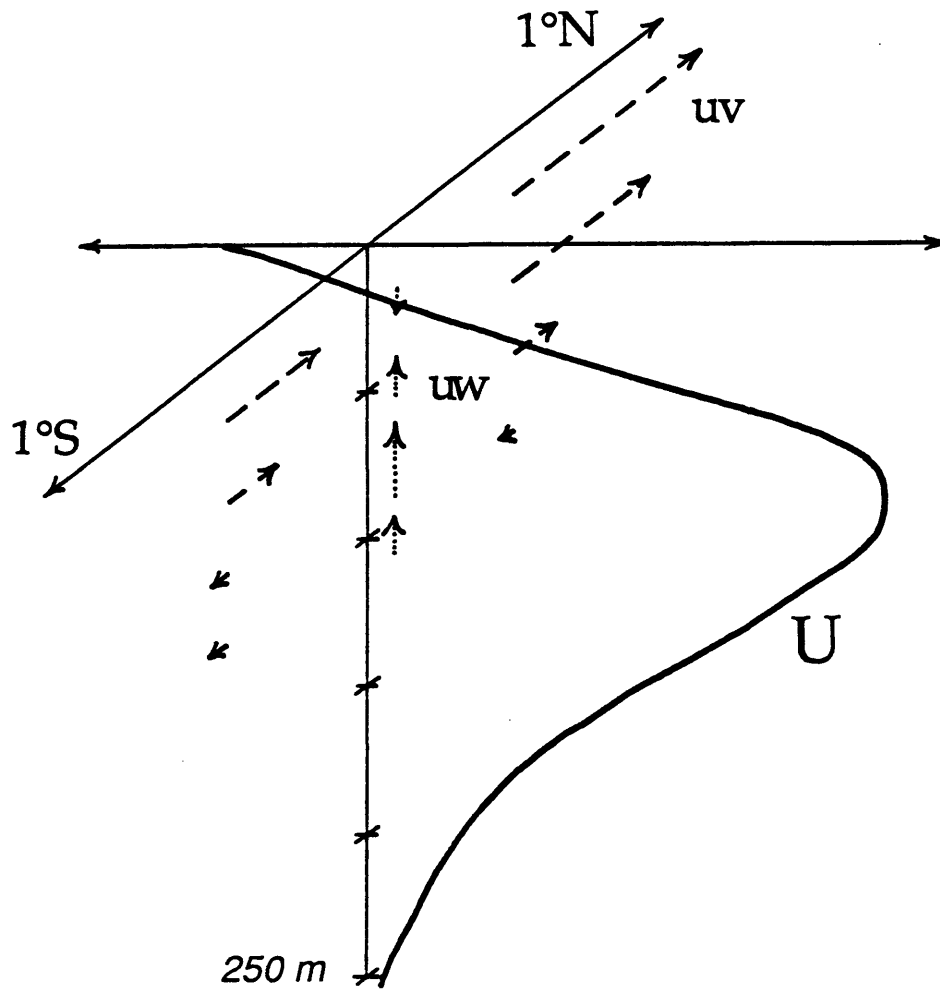


Figure 6.1: Three-dimensional schematic of the effect of the observed eddy Reynolds stresses on the zonal momentum balance of the mean equatorial Undercurrent. A typical equatorial zonal velocity profile is drawn as a function of depth with a maximum at 75 m. The northward flux of eastward momentum is drawn as dashed vectors; the upward flux of eastward momentum is drawn as dotted vectors.

6.2 CONCLUSIONS

Understanding how the 21 day waves or instability waves affect the momentum balance and energetics of the mean Equatorial Undercurrent was the central goal of this thesis. This study has successfully shown that these waves are necessary in the momentum and energy balances of the mean Undercurrent on the equator at 110°W , which is in the eastern Pacific Ocean. Through the EP flux, these waves redistribute the westward momentum input by the westward winds downward into deeper levels of the thermocline and laterally redistribute the eastward momentum of the Undercurrent northwards towards the South Equatorial Current (figure 6.0). The downward redistribution of westward stress allows the mean eastward pressure gradient force to be balanced at levels below the upper surface layer which is dominated by turbulence.

The northward redistribution of eastward momentum into the region of the SEC suggests a coupling of the EUC to the SEC through the mechanism of lateral shear instability. In the classical case of lateral shear instability of an isolated jet, when the isolated jet becomes unstable, momentum is redistributed by the growing waves in such a way that the velocity maximum is reduced and the velocity at the flanks is increased (Pedlosky, 1987). Thus, the lateral shear is diminished, which eventually shuts down the instability. Here, the eastward flowing Undercurrent is not an isolated feature, but is embedded within the westward flowing SEC. These waves effect an enormous northward flux of eastward momentum into the region of the SEC observed north of the equator (figure 6.1). If this eastward eddy momentum is deposited in the SEC, the lateral shear between the SEC and the EUC would be diminished, thus reducing the growth of the instability. The eddy flux of eastward momentum upwards into the region of negative velocity shear above the core, inferred in Chapter 3, also works to diminish the shear above the Undercurrent, hence reducing the source of the instability due to the waves working against the vertical shear of the Undercurrent.

The westward winds pump energy and momentum into the equatorial ocean (figure 6.2). The energy input is primarily stored in the east-west slope

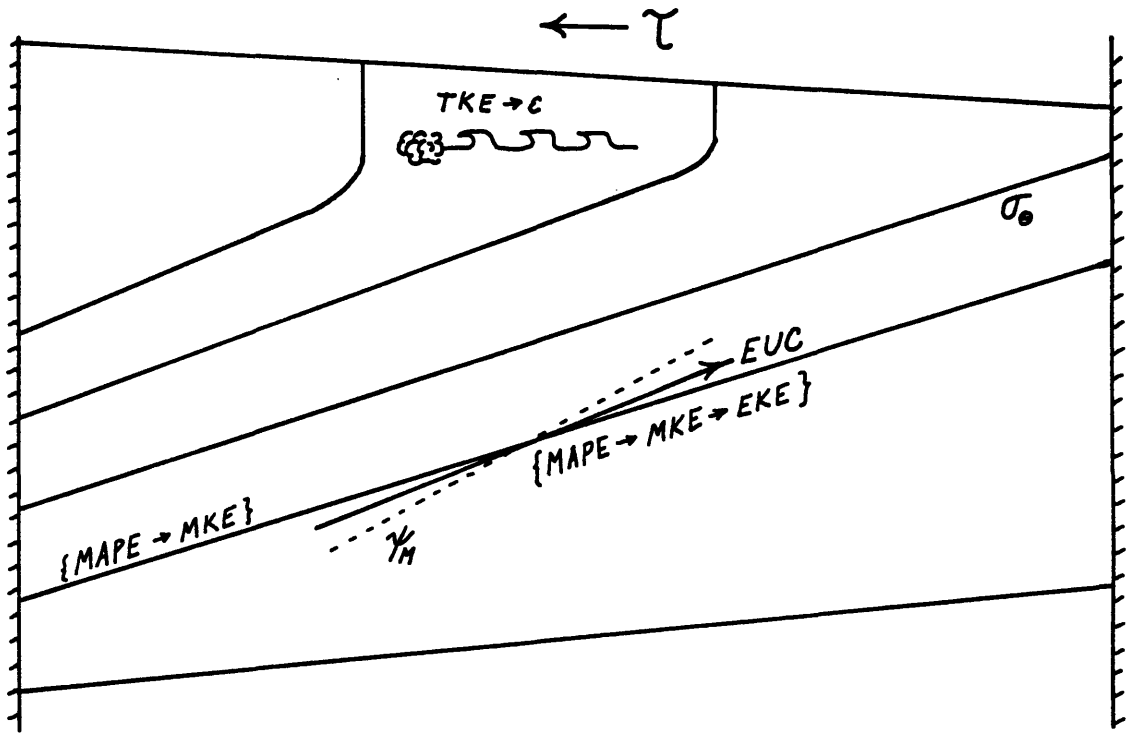


Figure 6.2: Schematic diagram for the mean energetics of the equatorial upwelling region. The westward wind stress τ puts energy into the equatorial ocean stored as available potential energy in the east-west sloping thermocline represented as lines of constant sigma-theta in the diagram. In the upper layer, some energy is immediately dissipated in the upper mixed layer as schematically shown by the process of breaking internal waves and some energy is directly converted into kinetic energy of the SEC (not schematically shown). The rest is released by the EUC as it flows “downhill” eastward and upward along the sloping thermocline as represented by the solid arrow which denotes the equatorial streamline of the EUC crossing downwards through a line of constant acceleration potential Ψ_M . The equatorial streamline is shown to be nearly parallel to both the potential density curve and Ψ_M .

of the thermocline as available potential energy (APE). To maintain an equilibrium, this energy must be removed at the same rate as it is stored. As the Undercurrent flows eastward, it releases available potential energy by flowing “downhill” from a region of high acceleration potential to low acceleration potential (Chapter 5). For a steady state, the available potential energy released can be converted into a downstream increase in mean kinetic energy or directly dissipated. In the western Pacific ocean, the EUC gains kinetic energy by this process as its velocity increases downstream. A downstream increase in kinetic energy is not observed in the central or eastern Pacific ocean as is shown by the slight decrease in kinetic energy observed between 150°W and 110°W (Chapter 5). Instead, the vertical and lateral shear between the SEC and EUC has become large enough for instabilities to grow. This is suggested by the observed growth rates of EKE (Chapter 4) by conversion from MKE. The EUC loses MKE by conversion to EKE through lateral shear instability at a rate of $0.5 \times 10^{-7} \text{ m}^2 \text{ s}^{-3}$ (Chapter 4), which is about the rate at which APE is released (Chapter 5). The direct conversion of APE to eddy potential energy is observed to be an order of magnitude smaller (Chapter 4). An upward phase propagation (Chapter 2) and a downward Eliassen-Palm flux (Chapter 3) suggest that the waves radiate energy into the deep ocean. Downward energy propagation is an energy sink for the upper thermocline. Turbulent dissipation may not be as important for dissipating the wind input below the core of the Undercurrent. In fact, below the core of the Undercurrent, turbulent dissipation rates are an order of magnitude lower than necessary to dissipate the energy released by the Undercurrent in flowing downhill (Hebert et al., 1990).

This thesis shows that the tropical instability waves, or 21 day waves, are important to the zonal momentum balance and energetics of the Equatorial Undercurrent. The waves redistribute eastward momentum northward away from the Undercurrent toward the South Equatorial Current, implying that the dynamics of these two currents may be linked. The waves also redistribute westward momentum downward to balance the eastward pressure gradient force at depth. In the eastern Pacific, these waves provide a way to remove energy from the upper thermocline where the wind puts energy into the large scale circulation stored as mean available potential energy associated with the east-west sloping thermocline.

APPENDIX

A Derivation of the Equations for the Interaction of a Wave Disturbance with a Slow, Large-scale Zonal Flow

The derivation of the equations for the slow evolution of an interactive system, comprised of a slowly varying large scale flow and a rapidly varying intermediate scale wave, follows from a multiple scale analysis. The evolution equations appear at second order in the expansion, based on the smallness of the ratio of the scale of the wave velocity amplitude to the scale of the large scale zonal flow. The geostrophic and hydrostatic balance of the zonal flow obtains at the lowest order, and the wave evolution equations modified by a laterally and vertically sheared zonal flow obtain at the next order.

Equations

The following equations, describing the motion of a Boussinesq, incompressible, hydrostatic fluid on the equatorial β plane with an external forcing or dissipation given in a general form (M^x , M^y) for momentum and Q for heat, will be used as the starting point in the procedure:

$$u_t + uu_x + vu_y + wu_z - fv + hw = -\frac{1}{\rho_0} p_x + M^x$$

$$v_t + uv_x + vv_y + wv_z + fu = -\frac{1}{\rho_0} p_y + M^y$$

$$w_t + uw_x + vw_y + ww_z - hu + g \frac{\rho}{\rho_0} = -\frac{1}{\rho_0} p_z$$

$$T_t + uT_x + vT_y + wT_z = Q$$

$$\rho = \rho(T)$$

$$u_x + v_y + w_z = 0$$

where u , v , and w are the velocity components of a fluid parcel in the x , y , and z directions, f is the vertical component of the Earth's rotation vector, tangent to the Earth's surface at the equator; it varies in the y direction as βy with constant β ; h is the horizontal component of the Earth's rotation vector at the equator equal to 2Ω , where Ω is the angular rotation speed of the Earth; in Boussinesq approximation, the density is given by $\rho_0(z) + \rho^*(x, y, z, t)$, where ρ_0 is the density of the resting state and is much larger than ρ ; T is the temperature; the density is a function of T alone; and p is the pressure after subtracting out the hydrostatic pressure of the resting fluid.

Equatorial Scaling

The system to be described here consists of two fluid motions superimposed, with well separated time and length scales such that the variables (u, v, w, T, p, ρ^*) can be written as a sum of a slowly varying flow, (U, V, W, T, P, ρ^*), which varies in time according to a slow scale τ and in the zonal direction x , according to a long zonal scale L_x and a wave flow ($u', v', w', T', p', \rho'$), which varies as a plane wave in x and t with zonal wavenumber k and frequency ω .

For well separated time and length scales, the relative scaling of this system is such that the wave scales $|\omega^{-1}|$ and $|k^{-1}|$ must be very small with respect to the slow scales τ and L_x . Thus, the small parameter ϵ^2 is defined, such that

$$|\omega|\tau \sim \epsilon^2 \text{ and } |k|L_x \sim \epsilon^2.$$

The length scale in the meridional direction y is L_y , which is shorter than the zonal length scale L_x and is the same order as the *intermediate* wave length scale $|k^{-1}|$. Observations of the Equatorial Undercurrent provide the motivation for such scaling. The Undercurrent varies only significantly over the zonal extent of the Pacific basin, approximately 10,000 km, whereas the characteristic length scale in the meridional direction is 100 km. Thus, ϵ is typically observed to be 0.1. The vertical scale of the Undercurrent is about 100 m. Thus, in choosing,

$$L_y \sim \epsilon^2 L_x \text{ and } L_z \sim \epsilon^5 L_x,$$

by comparison to observations, the continuity equation after averaging over a wave period is scaled as follows,

$$\frac{\partial U}{\partial x} + \frac{\partial V}{\partial y} + \frac{\partial W}{\partial z} = 0$$

$$1 \quad \frac{\mathcal{L}_x}{|U|} \frac{|V|}{\mathcal{L}_y} \quad \frac{|W|}{\mathcal{L}_z}$$

Thus, the scales appropriate for V and W for all slow, large scale terms to be of the same order in ϵ ,

$$|V| \sim \epsilon^2 |U| \text{ and } |W| \sim \epsilon^5 |U|,$$

which also agrees with observations, since $|V|$ is typically 1 cm s^{-1} at the edges of the Undercurrent, and $|W|$ is typically $10^{-3} \text{ cm s}^{-1}$ near the velocity maximum of the Undercurrent, while $|U|$ given by the velocity maximum, is typically 100 cm s^{-1} . That the continuity equation is assumed to be three-dimensional is consistent with the study by Bryden and Brady (1985), who found that the zonal convergence within the Undercurrent, over 40 degrees of longitude in their diagnostic model, was as important as the meridional divergence in determining the vertical velocity by integrating the continuity equation.

Similarly the continuity equation for the waves, obtained by subtracting the averaged continuity equation from the full equation is scaled as follows,

$$\frac{\partial u'}{\partial x} + \frac{\partial v'}{\partial y} + \frac{\partial w'}{\partial z} = 0$$

$$1 \quad \frac{|k^{-1}|}{|u|} \frac{|v|}{\mathcal{L}_y} \quad |w| |m|$$

The scalings,

$$|u| \sim |v|, |k^{-1}| \sim \mathcal{L}_y, \text{ and } |m^{-1}| \sim \mathcal{L}_z,$$

require that $|w| \sim \epsilon^5 |u|$ for all terms to be of the same order giving a fully three dimensional continuity equation.

Relative scaling of the wave velocity scales $|u|$ and $|v|$, by the mean flow scale $|U|$, is taken in the following expansion to be δ , where δ is a small number, to be determined as the lowest order of ϵ needed to allow the waves to affect the mean flow. It will be shown that δ is order ϵ . The waves

observed have amplitudes which exceed this ordering. A typical range in amplitude for u or v near the surface (at the larger end of the range) and in the vicinity of the Undercurrent core (at the smaller end of the range) is observed to be about 30 to 15 cm s⁻¹, thus δ would be about 0.3 to 0.15 for the actual scales in the real equatorial ocean over the domain of the Undercurrent. This is a bit larger than the size of ϵ as determined from the length scaling procedure above. However, the expansion discussed below reveals that δ must be the same order as ϵ .

Multiple Scale Expansion

Based on the scaling arguments above, new independent variables X and τ are defined such that,

$$X = \epsilon^2 x \text{ and } \tau = \epsilon^2 t.$$

Then,

$$\frac{\partial}{\partial t} \rightarrow \frac{\partial}{\partial \tau} + \epsilon^2 \frac{\partial}{\partial \tau} \text{ and } \frac{\partial}{\partial x} \rightarrow \frac{\partial}{\partial X} + \epsilon^2 \frac{\partial}{\partial X}.$$

Let each scaled variable u , v , w , T , ρ , and p , be decomposed into a slow, large scale flow and a fast wave, in the form,

$$u/|U| = U(X, y, z, \tau) + \delta u'(X, y, z, \tau)e^{i(kx' - \omega t' + mz)} \text{ and}$$

$$\frac{p}{\rho_0 |P|} = P(X, y, z, \tau) + \delta p'(X, y, z, \tau)e^{i(kx' - \omega t' + mz)} \text{ etc.,}$$

allowing for a slowly varying wave amplitude. The slow flow and the wave can each be further expanded in powers of ϵ , such that

$$U(X, y, z, \tau) = U_0 + \epsilon U_1 + \epsilon^2 U_2 + \dots \text{ and}$$

$$u'(X, y, z, \tau) = u'_0 + \epsilon u'_1 + \epsilon^2 u'_2 + \dots \text{ etc.}$$

Only the lowest order is important up to the order necessary to obtain the evolution equations for U and T , after averaging over a wave period, but it will be shown that there is a first order correction to the hydrostatic balance due to the vertical Coriolis force which is important in determining the next order correction to the geostrophic zonal flow.

Inserting the above decomposition and new operators into the equations above, scaling and then collecting like orders of ϵ and δ , yields the following.

$O(1)$:

At zeroth order in either ϵ or δ , the geostrophic, Ekman balance is obtained in the y momentum equation,

$$f U = -\frac{\partial P}{\partial y} + M^y.$$

This gives a scale relation between P and U , such that,

$$|P| \sim \beta L_y^2 |U|,$$

where f is scaled as βL_y , which can be used in the zeroth order z momentum equation to show that the Coriolis acceleration $2\Omega U$ is an order in ϵ smaller than $\frac{\partial P}{\partial z}$,

$$\frac{|2\Omega U|}{|\frac{\partial P}{\partial z}|} \sim \frac{\beta L_x |U|}{\beta L_y^2 |U| / L_z} \sim \frac{L_x L_z}{L_y^2} \sim \epsilon.$$

Thus the hydrostatic balance,

$$-\frac{\rho^*}{\rho_0} g = \frac{\partial P}{\partial z},$$

holds at zeroth order. No zeroth order balance is observed in the x momentum equation or in the temperature equation.

$O(\epsilon)$:

To obtain the ordering relationship between δ and ϵ , the terms in the x momentum equation at the second order in ϵ and δ , after averaging over a

wave period are examined. It is observed that in order for the waves to affect the evolution of U and T , the wave amplitude scale δ with respect to $|U|$ must be $O(\epsilon)$. This is because the terms affecting the evolution of U and T due to the slow fields alone enter at order ϵ^2 while the average wave transports of momentum and temperature are order δ^2 .

Thus, setting δ equal to ϵ , and averaging the $O(\epsilon)$ equations over a wave period, since the terms involving wave quantities average to zero, the $O(\epsilon)$ geostrophic and hydrostatic balance of the slow flow remain,

$$f U_1 = -\frac{\partial P_1}{\partial y} + M^y_1 \quad \text{and} \quad -hU + \frac{\rho_1}{\rho_0}g = -\frac{\partial P_1}{\partial z}.$$

Joyce, Lukas, and Firing (1988) discuss the ramifications of this second order correction to the hydrostatic balance due to the vertical Coriolis force to the calculation of geostrophic currents near the equator. They note that the correction to the zonal velocity due to this additional term, may be important in the upper 200 m since almost everywhere this correction is eastward, adding at most 10 cm s^{-1} to the usually calculated geostrophic equatorial currents.

Then, subtracting these $O(\epsilon)$ terms from the full $O(\epsilon)$ equations, yields the evolution equations for the wave with modifications by the slow, large scale flow U , along with the wave continuity equation and a linear equation of state relating ρ' and T' ,

$$u'_t + Uu'_x - (f - U_y)v' + w'U_z + p'_x = m'_x$$

$$v'_t + Uv'_x + f u' + p'_y = m'_y$$

$$T'_t + UT'_x + v'T_y + w'T_z = q'$$

$$g \frac{\rho'}{\rho_0} + p'_z = 0$$

$$u'_x + v'_y + w'_z = 0$$

$$\rho' = -\rho_0 \alpha T', \text{ where } \alpha = -\partial \rho / \partial T.$$

$O(\epsilon^2)$

At second order in ϵ , after averaging over a wave period so that terms involving the next order in ϵ in the expansions of U and T and u' , v' , and T' do not enter the equation at order ϵ^2 (i.e terms like $U_1 u'_x$, $U u'_{1x}$, and $U_1 T'_x$ etc., because these terms average to zero), the equations for the evolution of a slow, large scale flow due to the interaction of waves obtain:

$$U_\tau + UU_X - V(f - U_y) + W U_z + P_X = - \langle (u'^2)_x + (u'v')_y + (u'w')_z \rangle + M^x$$

$$T_\tau + UT_X + VT_y + WT_z = - \langle (u'T')_x + (v'T')_y + (w'T')_z \rangle + Q$$

where the operator $\langle \rangle$ denotes an average over a wave period.

REFERENCES

- Andrews, D. G., 1983: A finite-amplitude Eliassen-Palm theorem in isentropic coordinates. *J. Atmos. Sci.*, **40**, 1877-1883.
- Andrews, D. G., and M. E. McIntyre, 1976: Planetary waves in horizontal and vertical shear: the generalized Eliassen-Palm relation and the mean zonal acceleration. *J. Atmos. Sci.*, **33**, 2031-2048.
- Arthur, R. S., 1960: A review of the calculation of ocean currents at the equator. *Deep Sea Res.*, **6**, 287-297.
- Blandford, R., 1966: Mixed Rossby-gravity waves in the ocean. *Deep Sea Res.*, **13**, 941-961.
- Boyd, J. P., 1976: The noninteraction of waves with the zonally averaged flow on a spherical earth and the interrelationships of eddy fluxes of energy, heat and momentum. *J. Atmos. Sci.*, **33**, 2031-2048.
- Brady, E. C., 1986: Observations of 21 day waves on the equator at 110° W. *Trans. Am. Geophys. U.*, **67**(44), p 1035.
- Brady, E. C., and H. L. Bryden, 1987: Estimating vertical velocity on the equator. *Oceanologica Acta*, **6** SP, Proceedings of the International Symposium on Vertical Motion in the Upper Equatorial Ocean and its Effects upon Living Resources and the Atmosphere, Paris, 6-10 May 1985, 33-37.
- Bretherton, F. P., 1964: Low frequency oscillations trapped near the equator. *Tellus*, **16**, 191-185.
- Bryden, H. L., 1976: Horizontal advection of temperature for low-frequency motions. *Deep-Sea Res.*, **23**, 1165-1174.
- Bryden, H. L., 1982: Sources of eddy energy in the Gulf Stream recirculation region. *J. Mar. Res.*, **40**, 1047-1068.
- Bryden, H. L. and E. C. Brady, 1985: Diagnostic model of three-dimensional circulation in the upper equatorial Pacific ocean. *J. Phys. Oceanogr.*, **15**, 1255-1273.
- Bryden, H. L. and E. C. Brady, 1989: Eddy momentum and heat fluxes and their effect on the large scale circulation in the equatorial Pacific Ocean. *J. Mar. Res.*, **47**, 55-79.
- Cane, M. A., and S. E. Zebiak, 1985: A theory for El Nino and the Southern Oscillation, *Science*, **228**, 1085-1087.
- Cane, M. A. and E. S. Sarachik, 1979: Forced baroclinic ocean motions, III: The linear equatorial basin case. *J. Mar. Res.*, **37**, 355-398.
- Charney, J. G., 1969: A further note on large-scale motions in the tropics. *J. Atmos. Sci.*, **26**, 182-185.

- Chereskin, T. K., J. N. Moum, P. J. Stabeno, D. R. Caldwell, C. A. Paulson, L. A. Regier and D. Halpern, 1986: Fine-scale variability at 140°W in the equatorial Pacific. *J. Geophys. Res.*, **91**, 12887-12897.
- Cox, M. D., 1980: Generation and propagation of 30 day waves in a numerical model of the Pacific. *J. Phys. Oceanogr.*, **10**, 1168-1186.
- Crawford, W. R., 1982: Pacific equatorial turbulence. *J. Phys. Oceanogr.*, **12**, 1137-1149.
- Crawford, W. R., and T. R. Osborn, 1981: Control of equatorial ocean currents by turbulent dissipation. *Science*, **212**, 539-540.
- Cromwell, T., 1953: Circulation in a meridional plane in the central equatorial Pacific. *J. Mar. Res.*, **12**, 196-213.
- Dillon, T., J. M. Moum, T. K. Chereskin and D. R. Caldwell, 1989: Zonal momentum balance at the equator. *J. Phys. Oceanogr.*, **19**, 561-570.
- Duing, W., P. Hisard, E. Katz, J. Knauss, J. Meincke, et al., 1975: Meanders and long waves in the equatorial Atlantic. *Nature*, **257**, 280-284.
- Dunkerton, T., 1980: A Lagrangian mean theory of wave, mean-flow interaction with applications to nonacceleration and its breakdown. *Rev. Geophys. Space Phys.*, **18**, 387-400.
- Edmon, H. J., B. J. Hoskins, and M. E. McIntyre, 1980: Eliassen-Palm cross sections for the troposphere. *J. Atmos. Sci.*, **37**, 2600-2616.
- Eliassen, A., 1986: A method pioneered by Jerome Namias: Isentropic analysis and its aftergrowth. Namias Symposium, J. O. Roads, ed., *Scripps Inst. Oceanogr., ref. series*, **86-17**, 70-81.
- Eliassen, A., and E. Palm, 1961: On the transfer of energy in stationary mountain waves. *Geofys. Publ.*, **22**, 1-23.
- Eriksen, C. C., 1978: Evidence for a continuous spectrum of equatorial waves in the Indian ocean. *J. of Geophys. Res.*, **85**, 3285-3303.
- Fofonoff, N. P., 1962: Dynamics of ocean currents. in *The Sea*, vol. 1, M. N. Hill, ed., Interscience Publishers, 323-395.
- Fofonoff, N. P., and R. B. Montgomery, 1955: The Equatorial Undercurrent in the light of the vorticity equation. *Tellus*, **7**, 518-521.
- Freitag, H. P., M. J. McPhaden, and A. J. Shepard, 1987: Equatorial current and temperature data: 108°W to 110°W: October 1979 to November 1983. NOAA Data Report ERL PMEL-17, 99 pp.
- Gill, A. E., 1982: *Atmosphere-Ocean Dynamics*, Academic Press, San Diego, CA., 662 pp.
- Gregg, M. C., H. Peters, J. C. Wesson, N. S. Oakey and T. J. Shay, 1985: Intensive measurements of turbulence and shear in the equatorial undercurrent. *Nature*, **318**, 140-144.

- Hall, M. M., 1986: Assessing the energetics and dynamics of the Gulf Stream at 68W from moored current measurements. *J. Mar. Res.*, **44**, 423-443.
- Halpern, D., 1987: Comparison of upper ocean VACM and VMCM observations in the equatorial Pacific. *J. Atmos. Oceanic Technol.*, **4**, 84-93.
- Halpern, D., and H. P. Freitag, 1987: Vertical motion in the upper ocean of the equatorial Eastern Pacific. *Oceanologica Acta*, **6** SP, Proceedings of the International Symposium on Vertical Motion in the Upper Equatorial Ocean and its Effects upon Living Resources and the Atmosphere, Paris, 6-10 May 1985, 19-26.
- Halpern, D., R. A. Knox, and D. S. Luther, 1988: Observations of 20-day period meridional current oscillations in the upper oceans along the Pacific equator. *J. Phys. Oceanogr.*, **18**, 1514-1534.
- Hansen, D. V., and C. A. Paul, 1984: Genesis and effects of long waves in the equatorial Pacific. *J. Geophys. Res.*, **89**, 10431-10440.
- Hansen, D. V. and C. A. Paul, 1987: Vertical motion in the eastern equatorial Pacific inferred from drifting buoys. *Oceanologica Acta*, **6** SP, Proceedings of the International Symposium on Vertical Motion in the Upper Equatorial Ocean and its Effects upon Living Resources and the Atmosphere, Paris, 6-10 May 1985, 27-32.
- Harvey, R., and W. C. Patzert, 1976: Deep current measurements suggest long waves in the eastern equatorial Pacific. *Science*, **193**, 883-885.
- Hayes, S. P., 1982: A comparison of geostrophic and measured velocities in the Equatorial Undercurrent. *J. Mar. Res.*, **40**(Suppl), 219-229.
- Holton, J. R., 1974: The forcing of mean flows by stationary waves. *J. Atmos. Sci.*, **31**, 942-945.
- Holton J. R., and R. S. Lindzen, 1972: An updated theory of the quasi-biennial cycle. *J. Atmos. Sci.*, **29**, 1076-1080.
- Hoskins, B. J., M. E. McIntyre and A. W. Robertson, 1985: On the use and significance of isentropic potential vorticity maps. *Quart. J. Roy. Meteor. Soc.*, **111**, 877-946.
- Ichiye, T., 1960: On long waves in a stratified , equatorial ocean caused by a travelling disturbance. *Deep Sea Res.*, **6**, 16-37.
- Imawaki, S., P. P. Niiler, C. H. Gautier, D. Halpern, R. A. Knox, W. G. Large, D. S. Luther, J. C. McWilliams, J. N. Moum, and C. A. Paulson, 1988: A new method of estimating the turbulent heat flux at the bottom of the daily mixed layer. *J. Geophys. Res.*, **93**, 14005-14012.
- Joyce, T. M., 1988. Wind-driven cross-equatorial flow in the Pacific Ocean. *J. Phys. Oceanogr.* , **18**, 19-24.
- Joyce, T. M., R. Lukas, and E. Firing, 1988: On the hydrostatic balance and equatorial geostrophy. *Deep-Sea Res.*, **35**, 1255-1257.

- Kessler, W. S., 1989: Observations of long Rossby waves in the northern tropical Pacific. NOAA Technical Memorandum ERL PMEL-86, 169 pp.
- Knox, R. A., and D. Halpern, 1982: Long range Kelvin wave propagation of transport variations in the Pacific Ocean equatorial currents. *J. Mar. Res.*, **40**(Suppl.), 329-339.
- Lamb, V. R., 1973: The response of a tropical atmosphere to middle latitude forcing. Ph.D. thesis, Dept. of Atmospheric Sciences, University of California, Los Angeles, 151 pp.
- Legeckis, R., 1977: Long waves in the eastern equatorial Pacific Ocean: A view from a geostationary satellite. *Science*, **197**, 1179-1181.
- Legeckis, R., W. Pichel, and G. Nesterczuk, 1983: Equatorial long waves in geostationary satellite observations and in a multichannel sea surface temperature analysis. *Bull. Am. Met. Soc.*, **64**, 133-139.
- Lindzen, R. A., 1967: Planetary waves on beta-planes. *Mon. Wea. Rev.*, **95**, 441-451.
- Lindzen, R. S., and T. Matsuno, 1968: On the nature of large scale wave disturbances in the equatorial lower stratosphere. *J. Met. Soc. Japan*, **46**, 215-220.
- Lukas, R., 1984: The termination of the equatorial undercurrent in the eastern Pacific. *Progr. in Oceanogr.*, **16**, 63-90.
- Lukas, R., 1987: Horizontal Reynolds stresses in the equatorial central Pacific. *J. Geophys. Res.*, **92**, 9453-9463.
- Lukas, R. and E. Firing, 1984: The geostrophic balance of the Pacific Equatorial Undercurrent. *Deep Sea Res.*, **31**, 61-66.
- Luyten, J. R., J. Pedlosky and H. Stommel, 1983: The ventilated thermocline. *J. Phys. Oceanogr.*, **13**, 292-309.
- Luyten J., and D. Roemmich, 1984: The 26-day oscillation in the equatorial Indian ocean. Unpublished manuscript, 47pp.
- Mak, M.-K., 1969: Laterally driven stochastic motions in the tropics. *J. Atmos. Sci.*, **26**, 41-64.
- Malarde, J.-P., P. De Mey, C. Perigaud, and J. F. Minster, 1987: Observation of long equatorial waves in the Pacific Ocean by Seasat Altimetry. *J. Phys. Oceanogr.*, **17**, 2273-2279.
- Mangum, L, and S. Hayes, 1983: CTD/O₂ measurements during 1980 and 1981 as part of the Equatorial Pacific Ocean Climate Study (EPOCS). NOAA Data Report ERL PMEL-9, 621 pp.
- Mangum, L, and S. Hayes, 1984: The vertical structure of the zonal pressure gradient in the eastern equatorial Pacific. *J. Geophys. Res.*, **89**, 10441-10449.

- Maruyama, T., 1967: Large-scale disturbances in the equatorial lower stratosphere. *J. Meteor. Soc. Japan*, **45**, 391-408.
- Matsuno, T., 1966: Quasi-geostrophic motions in the equatorial area. *J. Meteor. Soc. Japan*, **44**, 25-43.
- McIntyre, M. E., 1980: An introduction to the generalized Lagrangian-mean description of wave, mean-flow interaction. *Pure Appl. Geophys.*, **118**, 152-176.
- McPhaden, M. J., J. A. Proehl, and L. M. Rothstein, 1986: The interaction of equatorial Kelvin waves with realistically sheared zonal currents. *J. Phys. Oceanogr.*, **16**, 1499-1515.
- McPhaden, M. J. and P. Ripa, 1990: Wave-mean flow interactions in the equatorial ocean. *Annu. Rev. of Fluid Mech.*, **22**, 167-205.
- Meyers, G., 1979: Annual variation in the slope of the 14°C isotherm along the equator in the Pacific Ocean. *J. Phys. Oceanogr.*, **9**, 885-891.
- Montgomery, R. B., 1937: A suggested method for representing gradient flow in isentropic surfaces. *Bull. Amer. Met. Soc.*, **18**, 210-212.
- Montgomery, 1938: Circulation in upper layers of southern North Atlantic deduced with use of isentropic analysis. *MIT-WHOI Papers in Phys. Oceanogr. and Meteorol.*, **6** (2), 1-55
- Montgomery, R. B., and E. Palmen, 1940: Contribution to the question of the Equatorial Counter Current. *J. Mar. Res.*, **3**, 112-133.
- Montgomery, R. B., and E. D. Stroup, 1962: Equatorial waters and currents at 150°W in July-August 1952. *The Johns Hopkins Oceanographic Studies*, No. 1, 68 pp.
- Montgomery, R. B., and W. S. Wooster, 1954: Thermoclinic anomaly and the analysis of serial oceanographic data. *Deep-Sea Res.*, **2**, 68-70.
- Moum, J. N., D. R. Caldwell, C. A. Paulson, T. K. Chereskin and L. A. Regier, 1986: Does ocean turbulence peak at the equator? *J. Phys. Oceanogr.*, **16**, 1991-1994.
- Pedlosky, J., 1987a: *Geophysical Fluid Dynamics*, Springer-Verlag, New York, second edition, 710 pp.
- Pedlosky, J., 1987b: An inertial theory of the equatorial undercurrent. *J. Phys. Oceanogr.*, **17**, 1978-1985.
- Pedlosky, J., 1988: Entrainment and termination of the equatorial undercurrent. *J. Phys. Oceanogr.*, **18**, 880-886.
- Pedlosky, J. and R. M. Samelson, 1989: Wind forcing and the zonal structure of the equatorial undercurrent. *J. Phys. Oceanogr.*, **19**, 1244-1254.

- Perigaud, C., 1989: Instability waves in the tropical Pacific observed with Geosat. In *Proceedings of the TOGA-COARE Meeting*, ORSTOM, Noumea, New Caledonia, 637-648.
- Perigaud, C., 1990: Sea level oscillations observed with Geosat along the two shear fronts of the Pacific North Equatorial Countercurrent. *J. Geophys. Res.*, **95**, 7239-7248.
- Peters, H., M. C. Gregg, and J. M. Toole, 1989: Meridional variability of turbulence through the Equatorial Undercurrent. *J. Geophys. Res.*, **94**, 18003-18009.
- Philander, S. G. H., 1976: Instabilities of zonal equatorial currents. *J. Geophys. Res.*, **81**, 3725-3735.
- Philander, S. G. H., 1978: Forced oceanic waves. *Rev. Geophys. Space Phys.*, **16**, 15-46.
- Philander, S. G. H., 1978: Instabilities of zonal equatorial currents, 2. *J. Geophys. Res.*, **83**, 3679-3682.
- Philander, S. G. H., W. J. Hurlin and R. C. Pacanowski, 1986: Properties of long equatorial waves in models of the seasonal cycle in the tropical Atlantic and Pacific Oceans. *J. Geophys. Res.*, **91**, 14207-14211.
- Philander, S. G. H., D. Halpern, D. Hansen, R. Legeckis, M. Laury, C. Paul, D. R. Watts, R. Weisberg and M. Wimbush, 1985: Long waves in the equatorial Pacific Ocean. *Trans. Amer. Geophys. Union*, **66**, 154.
- Ripa, P., 1983: General stability conditions for zonal flows in a one-layer model on the β -plane or the sphere. *J. Fluid Mech.*, **126**, 463-489.
- Schudlich R. R., and J. F. Price, 1990: Diurnal cycles of turbulent dissipation, current, and temperature in a model of the equatorial upper ocean. Submitted to *J. Phys. Oceanogr.*
- Semtner, A. J. and W.R. Holland, 1980: Numerical simulation of equatorial circulation. Part I: A basic case in turbulent equilibrium. *J. Phys. Oceanogr.*, **10**, 667-693.
- Stern, M. E., 1963: Trapping of low frequency oscillations in an equatorial boundary layer. *Tellus*, **15**, 246-250.
- Stommel, H., H. Bryden, and P. Mangelsdorf, 1973: Does some of the Mediterranean Outflow come from great depth? *Pure and Appl. Geophys.*, **105**, 879-889.
- Stroup, E. D., 1960: The thermostat of the 13°C water in the equatorial Pacific Ocean. Ph. D. thesis, The Johns Hopkins University, 205 pp.
- Toole, J. M., H. Peters, and M. C. Gregg, 1987: Upper ocean shear and density variability at the equator during TROPIC HEAT. *J. Phys. Oceanogr.*, **17**, 1397-1406.

- Tsuchiya, M., 1968: Upper waters of the intertropical Pacific Ocean. *The Johns Hopkins Oceanographic Studies*, No. 4, 50 pp.
- Tsuchiya, M., 1975: Subsurface countercurrents in the eastern equatorial Pacific Ocean. *J. Mar. Res.*, **33** (Suppl), 145-175.
- Tsuchiya, M., 1981: The origins of the Pacific equatorial 13°C water. *J. Phys. Oceanogr.*, **11**, 794-812.
- Vallis, G. K., 1988: Conceptual Models of El Nino and the Southern Oscillation. *J. Geophys. Res.*, **93**, 13979-13991.
- Wacongne, S. 1988: Dynamics of the equatorial Undercurrent and its termination. Ph. D. thesis, M. I. T./W. H. O. I. Joint Program in Physical Oceanography, 365 pp.
- Wallace, J. M., 1973: General circulation of the tropical lower stratosphere. *Rev. Geophys. Space Phys.*, **11**, 191-222.
- Wallace, J. M. and V. E. Kousky, 1968: Observational evidence of Kelvin waves in the tropical stratosphere. *J. Atmos. Sci.*, **25**, 900-907.
- Weisberg, R. H., 1984: Instability waves observed on the equator in the Atlantic Ocean during 1983. *Geophys. Res. Lett.*, **11**, 753-756.
- Weisberg, R. H., A. Horigan, and C. Colin, 1979: Equatorially trapped Rossby-gravity wave propagation in the Gulf of Guinea. *J. Mar. Res.*, **37**, 67-86.
- Wunsch, C., and A. E. Gill, 1976: Observations of equatorially trapped waves in Pacific sea level variations. *Deep-Sea Res.*, **23**, 371-390.
- Wyrtki, K., 1978: Lateral oscillations of the Pacific equatorial countercurrent. *J. Phys. Oceanogr.*, **8**, 530-532.
- Wyrtki, K., 1981: An estimate of equatorial upwelling in the Pacific. *J. Phys. Oceanogr.*, **11**, 1205-1214.
- Wyrtki, K., and E. B. Bennett, 1963: Vertical eddy viscosity in the Pacific Equatorial Undercurrent. *Deep-Sea Res.*, **10**, 449-455.
- Yanai, M., 1975: Tropical meteorology. *Rev. Geophys. Space Phys.*, **13**, 685-710.
- Yanai, M. and Y. Hayashi, 1969: Large-scale equatorial waves penetrating from the upper troposphere into the lower stratosphere. *J. Meteorol. Soc. Japan*, **47**, 167-182.
- Yanai, M. and T. Maruyama, 1966: Stratospheric wave disturbances propagating over the equatorial Pacific. *J. Meteor. Soc. Japan*, **44**, 291-294.
- Yanai, M. and M.-M. Lu, 1983: Equatorially trapped waves at the 200 mb level and their association with meridional convergence of wave energy flux. *J. Atmos. Sci.*, **40**, 2785-2803.

Zangvil, A., and M. Yanai, 1980: Upper tropospheric waves in the tropics. Part I: Dynamical analysis in the wavenumber-frequency domain. *J. Atmos. Sci.*, **38**, 939-953.

Biographical Sketch and List of Publications

Born on the seventeenth of June, 1960, in Camp Lejeune, North Carolina. Lived throughout the United States. Attended the University of Massachusetts, Amherst from 1978 to 1982, majoring in Physics with a senior thesis project in Galactic Radio Astronomy with Dr. Judith Young at the Five College Radio Astronomy Observatory; graduated with a Bachelor of Science in 1982. Worked as a summer research assistant in 1981 to Dr. William Smethie at the Lamont-Doherty Geological Observatory in Palisades, New York. Attended the Woods Hole Oceanographic Institution/Massachusetts Institute of Technology Joint Program in Physical Oceanography from 1982 to 1987, and from 1989 to 1990, as a Ph.D. candidate working with Dr. Harry Bryden, advisor. Worked as research assistant at the Woods Hole Oceanographic Institution to Dr. Harry Bryden from 1987 to 1989. Participated in three oceanographic cruises: in 1984, on Tropic Heat Microstructure cruise, on R/V Thompson; in 1987, on Gulf Stream SYNOP cruise on R/V Endeavor; in 1988-1989 on Transpacific 10°N cruise on R/V Moana Wave.

Publications

Physical Oceanography

Brady, Esther C., and Harry L. Bryden, 1987.

Estimating Vertical Velocity on the Equator. *Oceanologica Acta* No. SP, Proceedings International Symposium on Equatorial Vertical Motion, Paris, 6-10 May 1985, 33-37.

Bryden, Harry L., and Esther C. Brady, 1985.

Diagnostic Model of the Three-Dimensional Circulation in the Upper Equatorial Pacific Ocean. *Journal of Physical Oceanography*, **15**, 1255-1273.

Bryden, Harry L. and Esther C. Brady, 1989.

Eddy Momentum and Heat Fluxes and their Effects on the Circulation of the Equatorial Pacific Ocean. *Journal of Marine Research*, **47**, 55-79.

Other Scientific

- Young, Judith S., N. Z. Scoville, and Esther Brady, 1985.
The Dependence of CO Content in Morphological Type and
Luminosity for Spiral Galaxies in the Virgo Cluster. *Astrophysical
Journal*, 288(2), Part I., 487-493.

Non-refereed Physical Oceanography

- Bryden , H. L. , E. C. Brady, and D. Halpern, 1987.
Lateral Mixing in the equatorial Pacific. In: *Further Progress in
Equatorial Oceanography*, E. J. Katz and J. M. Witte, eds., Nova
University Press, Fort Lauderdale, Florida, 121-131.
- Bryden, H. L., E. C. Brady, and R. D. Pillsbury, 1989.
Flow through the Strait of Gibraltar. *Proceedings Seminario sobre la
Oceanografía Fisica del Estrecho de Gibraltar*, in Madrid, 24-28 October
1988. Published by SECEG, 1989, 166-194.
- Thompson, Luanne and Esther Brady, 1989.
The Pilot Moorings of the Gibraltar Experiment: Flow over the
Camarinal Sill. *Proceedings Seminario sobre la Oceanografía Fisica del
Estrecho de Gibraltar*, in Madrid, 24-28 October 1988. Published by
SECEG, 1989, 151-165.